國立交通大學

光電工程研究所

博 士 論 文

半絕緣砷化鎵與砷離子佈植砷化鎵

天線之兆赫茲輻射實驗與模擬分析

A study of generation of terahertz radiations from semi-insulating

and arsenic-ion-implanted GaAs photoconductive antennas

研 究 生：周 榮 華

指導教授：潘 犀 靈 教授

中 華 民 國 九 十 七 年 七 月

半絕緣砷化鎵與砷離子佈植砷化鎵

天線之兆赫茲輻射實驗與模擬分析

A study of generation of terahertz radiations from semi-insulating

and arsenic-ion-implanted GaAs photoconductive antennas

研 究 生：周 榮 華　　　　　Student：Yi-Chao Wang

指導教授：潘犀靈 教授　　　　Advisor：Prof. Ci-Ling Pan

國 立 交 通 大 學

光 電 工 程 研 究 所

博 士 論 文

A Thesis

Submitted to Department of Photonics &

Institute of Electro-Optical Engineering

College of Electrical Engineering

National Chiao Tung University

In partial Fulfillment of the Requirements

for the Degree of

Doctor of Philosophy

in

Electro-Optical Engineering

July 2008

Hsinchu, Taiwan, Republic of China

中華民國九十七年七月

半絕緣砷化鎵與砷離子佈植砷化鎵

天線之兆赫茲輻射實驗與模擬分析

研　究　生：周　榮　華　　　　　　指導教授：潘　犀　靈　教授

國立交通大學

光電工程研究所

中文摘要

　　在此所呈現的工作之主要焦點在對於不同孔徑大小的偏壓光導天線的實驗分析和由光激發產生兆赫輻射脈衝之數值與解釋。孔徑大小 1.5 公分的天線被定義為大孔徑天線。孔徑大小從 20 微米到 0.5 公釐範圍的天線則是被區分為中型孔徑天線。製造天線所使用的光導材料是砷離子佈植的砷化鎵（GaAs:As[+]）和使用半絕緣的砷化鎵（SI-GaAs）。

　　理論上，我們採用描述電磁波傳輸的一組非線性偏微分方程式，包含了電磁波、載子的漂移－擴散，和波頌方程式來解釋測量到的資料。這一個模型考慮到發生在兆赫天線內的空間－電荷電場，以及近場屏避電場的效應。在中型孔徑天線中，前者扮演了一個重要的角色，而後者在大孔徑天線中主要決定其特性。

在實驗上，我們從不同觀點分析這些測量到的兆赫輻射脈衝波形，包括尖峰峰值，尖峰寬度，負與正峰值的比，以及頻寬。我們發現來自中型孔徑天線中，測量到的兆赫脈衝的特性顯著地仰賴孔徑大小和光導材料。我們可以從我們的理論模擬推論，測量到的孔徑相依的行為源自於較大孔徑的天線在其陽極的附近有一個因陷阱而提高的偏壓電場是較強的，因此引起較大的空間－電荷電場屏避的效應，以及較大的頻寬。對於大孔徑天線的實驗結果來說，我們的砷離子佈植砷化鎵天線比半絕緣砷化鎵天線展現了更大的頻寬和更好的發射效率。由已知的實驗觀察可得知，砷離子佈植砷化鎵天線的光學吸收係數在某些條件下，可以是大於半絕緣砷化鎵天線的光學吸收係數，我們將此假設代入理論模型中，由模擬結果我們成功地驗證了砷離子佈植砷化鎵天線的優越特性確實能歸因於在離子佈植層中比起半絕緣砷化鎵有較大的吸收係數。對於兩者類型的材料，我們觀察到輻射出來的尖峰兆赫振幅顯示對於泵光輝度有一個異常的相關性，這相關性偏離了縮放比例規則所給的預測。分析那理論上的和模擬結果，我們推論出這種行為起因於帶填充和雙光子的吸收效果的發生。此外，在特定的泵光輝度之下，尖峰兆赫振幅對於偏壓電場的相關性，偏離了從被縮放比例規則預測的線性關係。

A study of generation terahertz radiations from semi-insulating and arsenic-ion-implanted GaAs photoconductive antennas

Student : Rone-Hwa Chou   Advisor : Prof. Ci-Ling Pan

Department of Photonics and Institute of Electro-Optical Engineering

National Chiao Tung University

Abstract

The work presented here is focused on the experimental analysis and numerical explanation of the terahertz radiation pulses from biased photoconductive antennas with different gap sizes. The antenna with gap sizes of 1.5 cm is divided into large-aperture antennas. The antennas with gap sizes ranging from $20\ \mu$m to 0.5 mm are divided into mid-size-gap antennas. The photoconductive materials fabricated on the large-aperture antennas are arsenic-ion-implanted GaAs (GaAs:As$^+$) and semi-insulating GaAs (SI-GaAs). The photoconductive material fabricated on the mid-size-gap antennas is multi-energy arsenic-ion-implanted GaAs (GaAs:As$^+$).

Theoretically, we adopt a set of nonlinear partial differential equations including an electromagnetic wave, drift-diffusion, and Poisson equations to interpret the measured data. This model considers the space-charge field and near-field screening effects within the THz antenna. The former plays an important role in the mid-size-gap antennas, whereas the latter is dominant in the large-aperture antennas. Experimentally, we analyze these measured terahertz radiation waveforms from different point of views, including the peak terahertz amplitude, the peak width, the ratio of negative peak to positive peak, and bandwidth. We find that the characteristics of measured terahertz pulses from the mid-size-gap antennas depend markedly on both the gap size and photoconductive material. We deduce from our simulation that the gap-dependent behavior stems from the fact that an antenna with larger gap has a stronger trap-enhanced bias field near the anode edge and thereby induces larger space-charge field screening effect and bandwidth.

For the large-aperture antennas, our single-energy arsenic-ion-implanted GaAs antenna exhibits larger bandwidth and better emission efficiency in comparison with semi-insulating GaAs antenna. Our simulation verifies that the superior characteristics for the latter can be partly attributed to larger optical absorption in the ion-implanted layer. For both types of materials, we observe that the radiated peak terahertz amplitude displays an anomalous dependence on pump fluence, which deviates from

the prediction given by the scaling rule. Analyzing the theoretical and simulation results, we infer that this behavior arises from band filling and two-photon absorption effects. Besides, at specific pump fluence, the dependence of peak terahertz amplitude on bias field is also distinct from the usual linear relationship predicted by the scaling rule.

Acknowledgements

I am deeply indebted to my advisor, Prof. Ci-Ling Pan, for giving me the opportunity to work in this area, for his precious advice, continuous encouragement and full support during my research.

I am also very grateful to Dr. Tze-An Liu for his assistance and valuable discussion in my research. I hardly finish my research without his kindly help.

I would like to thank my wife, Anne Wu, most heartily for her patience, encouragement, and understanding during the course of this work.

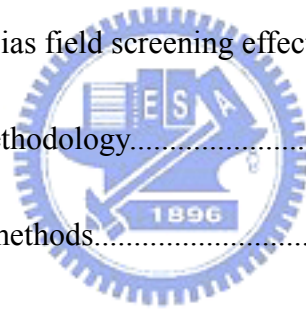Finally, to my parents I dedicate my honor in token of affection and gratitude.

Contents

Table Captions

Figure Captions

Chapter 1

Introduction

1.1   Background

Although terahertz (THz) radiation generated from biased photoconductive (PC) antennas have been widely used in many disciplines, we can found that some experimental phenomena are not able to be explained by proper physical mechanisms. For example, the scaling rule which gives the pump fluence dependence of peak THz amplitude indicates that the peak THz amplitude should saturate at high fluence. However, some experiments show anomalous results that the peak THz amplitude decreases gradually at high fluence. In addition, some fundamental principles involving with carrier dynamics within PC antennas are still unclear by the researchers. For example, it is found experimentally that the space-charge bias field screening effect is dominant in a small-gap photoconductive antenna, whereas plays minor role in a large-aperture photoconductive antenna. We also found that the THz pulse width calculated from some theoretical models is narrower than the measured width. Up to now, theoretical models have provided no interpretations for this inconsistence between theory and experiment.

Over past ten years, many groups have attempted to design an THz radiation emitter with maximum emission efficiency. To reach this purpose, researchers employ different PC materials or metallic patterns to fabricate on the antennas, and also vary the optical pump conditions in order to observe their different performance. Nevertheless, these experimental studies still lack corresponding theoretical works.

1.2 Overview of terahertz radiation

1.2.1 Terahertz radiation

We usually classify the electromagnetic radiation in the frequency range from 0.2×10^{12} to 20×10^{12} Hz as terahertz (THz) radiation where is a largely unexplored frontier area for research in science and engineering in part since reliable sources of high quality THz radiation have been scarce. From the electromagnetic spectrum of Fig. 1.1, we can see that the THz frequency range lies above the high-frequency range of electronics, but below the range of the traditional fields of optics. The fact that the THz frequency range lies in the transition region between electronics and photonics has led to creative ways in source development. Many groups have made great efforts to develop THz radiation sources in both continuous-wave and pulsed way. In particular, pulsed sources used in THz time domain spectroscopy (THz-TDS) as shown in Fig. 1.2 has generated a great deal of interest, and sparked a rapid growth in

the field of THz science and technology.

1.2.2   Sources of THz radiation

Free-Space Electron Laser (FEL) [1-2], and backward wave oscillators (BWO) [3] are electron beam sources that generate relatively high power signals at the terahertz frequency range. All of these devices work based on the interaction of a high-energy electron beam with a strong magnetic field inside resonant cavities or waveguides. Due to this interaction, energy transfer occurs from the electron beam to an electromagnetic wave. Conventional lasers rely on the inversion of an atomic or molecular transition. Thus the wavelength at which they operate is determined by the active medium they use. The FEL eliminates the atomic "middle-man", and does not rely on specific transitions. Potentially FEL's offer three main characteristics those are often hard to get with conventional lasers, namely wide tunability, high power and high efficiency. They do this by using a relativistic beam of free electrons that interact with a periodic structure, typically in the form of a static magnetic field. This structure exerts a Lorentz force on the moving electrons, forcing them to oscillate. The basic idea is to cause all the electrons to have approximately the same phase, thereby producing constructive interference (stimulated emission). A key feature of these lasers is that the emitted radiation is a function of the electron energy and we can change the wavelength of the FEL simply by the changing the energy of the electrons.

The FEL is therefore a widely tunable system and can be tuned to emit THz radiation. However, the main disadvantages of these electron beam devices are bulky and need extremely high fields as well as high current densities.

By injecting a CO_2 pump laser light into a cavity filled with a gas that lases, one also can obtain THz radiation [4-5]. The lasing frequency is fixed dictated by the filling gas. Tunable sources have been developed based on mixing a tunable microwave source with these gas lasers [6-7]. Power levels of 1 - 20 mW are common for 20 - 100 W laser pump power depending on the chosen line, with one of the strongest being that of methanol at 2522.78 GHz. A miniaturized gas laser has been reported with $75 \times 30 \times 10$ cm dimensions and 20 kg weight, which generates 30 mW power at 2.5 THz [8].
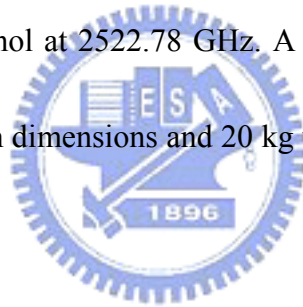
One approach to generate THz radiation is the quantum-cascade laser (QCL), first proposed by R. F. Kazarinov and R. A. Suris back in 1971 [9]. For the THz generation the QCL employs the intraband transitions in a biased doped semiconductor heterostructure. The first operating device was demonstrated however only in 1994 by J. Faist and coworkers [10], and despite the impressive progress in the QCL development achieved ever since, these devices are not yet able to operate at a room temperature.

Another approach to generate THz radiation is to make use of the Free-Space

Electro-Optic Sampling (FSEOS). This technique is based on an emission by optical

rectification [11], [12]. Optical rectification is a process first observed in the 1960's

that describes how a pulse at optical frequencies can be downshifted by degenerate

difference frequency generation inside a non-linear crystal. This effect arises from the

second order susceptibility χ of a crystal. The susceptibility, $\chi = P / \varepsilon_0 E$ measures

the degree of polarization, P, caused when an electric field, E, is applied to a

dielectric material (ε_0 is the permittivity of a vacuum). The non-linearity between the

polarization, P, and the magnitude of the electric field, E, may be encompassed by

writing P as a power series in $P = \varepsilon_0 \left(\chi_1 E + \chi_2 E^2 + \chi_3 E^3 + ... \right)$. Higher order terms

such as χ_2, denote the non-linear response of the materials and are important for the

high electric fields found in laser pulses. In a material subjected simultaneously to

waves of frequencies ω_1 and ω_2, the P will contain a term of the form,

$\cos \omega_1 t \cos \omega_2 t = \left[\cos \left(\omega_1 + \omega_2 \right) t + \cos \left(\omega_1 - \omega_2 \right) t \right] / 2$. Thus both sum and difference

frequencies will be generated [13].

Ultrafast pulses with a temporal width of approximately 70 fs comprise a large

number of difference frequency waves and have a frequency bandwidth in excess of

10 THz. Using an ultrafast visible pulse to excite a crystal that has large second-order

susceptibility, such as zinc telluride, produces a time varying polarization of the

electron cloud inside the crystal. We can think of the oscillating electron cloud with

5

electric polarization, P, vibrating at the various frequencies (say ω_1 and ω_2) that

correspond to those that make up the incident pulse of visible light. The electron

cloud then re-radiates at THz frequencies, $\omega_{THz} = \omega_1 + \omega_2$, as a result of the beats that

form between the various frequency components. The pulse of THz electromagnetic

radiation contains a broad range of frequencies, from zero up to the bandwidth of the

visible radiation. The power of the THz pulse is derived entirely from the incident

laser pulse, so FSEOS has typically lower power.

1.2.3   Applications of THz radiation

Along with the progress of THz radiation sources, recently researchers have

become increasingly interested in exploiting THz radiation for numerous

technological applications including spectroscopy, sensing, range finding, tomography

and microscopy, and imaging [14]. In these applications, THz spectroscopy [15-16] is

valuable for distinguishing molecules and studying intermolecular interactions, while

tomography relates to imaging through the successive layers of a material.

Microscopy with THz radiation is realized by working in the near-field THz radiation

pattern, thus overcoming the far-field wavelength limitation on resolution. Imaging

remains the most fervently researched and eagerly awaited application of THz

radiation. There exists a further uncountable number of applications for THz radiation

and even a brief description of these would be ambitious. We have therefore opted to give a bullet-point review of some of the more interesting applications in biology, chemistry, gas detection, medicine and elsewhere before giving a more comprehensive account of THz radiation imaging.

The experiments for THz time-domain spectroscopy (THz-TDS) use coherent pulses of electromagnetic radiation to obtain information about the frequency range between 0.1 and 5 THz. The electromagnetic pulses have sub-picosecond width and field strength on the order of 10-100 V/cm, depending on antenna geometry. In THz-TDS experiments, the picosecond pulses of THz radiation are used to probe different materials. The radiation has several distinct advantages over other forms of spectroscopy: many materials are transparent to THz; THz radiation is safe for biological tissues because it is non-ionizing unlike X-rays, and images formed with THz radiation can have relatively good resolution (less than 1 mm). Also, many interesting materials have unique spectral fingerprints in the THz range, which means that THz radiation can be used to identify them. The emerging field of TDS typically relies on broadband short-pulse THz sources employing photoconductive (PC) antennas [17-18], since the broad bandwidths correspond to short coherence lengths, which are required for high resolution imaging or tomography and sensing. This broadband technique is also widely used to obtain linear spectroscopic information,

such as complex dielectric constants or the conductivity of materials to fully understand the behavior with very broad spectral coverage. As implied in the title of the dissertation, we shall be dealing with ultrafast carrier dynamics in GaAs-based photoconductive THz antennas to simulate the emitted THz transients using numerical simulation. These will be detailed in the ensuing chapters of the dissertation.

1.3 Motivation

Experimentally, the photoconductive antenna based on LT-GaAs lacks of the reproducibility, and thus we want to search a replacement of low temperature grown GaAs (LT-GaAs) without losing the THz emission efficiency. One of the replacement is the arsenic-ion-implanted GaAs (GaAs:As$^+$). We want to verify that whether such ion-implanted material are able to replace LT-GaAs or not by investigating its characteristics of terahertz radiation. Understanding the detail mechanisms in a photoconductive antenna can help us promote the device efficiency in order to reach an optimum terahertz radiation operation. We expect to adopt a rigorous theoretical model to explain the observed phenomena in experiments. After the validity of the model is verified, we want to vary some parameters of the model to predict its possible results and also give a suggestion on how to fabricate THz antennas with high emission efficiency.

1.4   Contributions of this thesis

This thesis makes some contributions to the knowledge of the generation of THz radiation. The main contributions to THz radiation can be listed as the following seven points:

1. We systematically investigate the characteristics of THz radiation from large-aperture and mid-size-gap biased photoconductive antennas.

2. We use large-aperture and mid-size-gap biased photoconductive antennas with two different materials to compare their distinct characteristics of THz radiation.

3. For mid-size-gap biased photoconductive antennas, we observe their THz radiation under different gap size and two different materials.

4. For large-aperture photoconductive antennas, we construct a rigorous theoretical model to interpret several measured features including THz waveforms, THz pulse width, pump fluence dependence, and anomalous saturation behavior.

5. We construct another rigorous theoretical model to explain the gap-dependent THz waveforms from mid-size-gap photoconductive
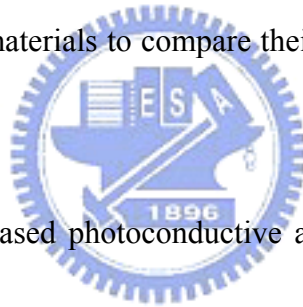
antennas, and also demonstrate the carrier and field dynamic behavior

which can give us a good insight of fundamental THz radiation principle.

6.   We clearly deduce each physical mechanism responsible for the measured

result for large-aperture and mid-size-gap photoconductive antennas.

7.   We point out the way to further improve the interpretation and prediction of

numerical simulation in future works.

1.5   Organization of this thesis

We organize our thesis below:

Chapter 1 gives the fundamental principle involving with THz radiation, and

reviews some terahertz radiation sources and their operation principles. The

motivation and our contribution are also contained in this chapter.

In the Chapter 2 we describe photoconductive antennas with different types of

designs and three kinds of materials.

In the Chapter 3 we review four theoretical models involving with carrier and

field dynamics. The numerical algorithm is also provided for each model. We will

also suggest several softwares to use in numerical simulation.

In the Chapter 4 we conduct a comparison between the characteristics of

terahertz   radiation   pulses   generated   using   biased   semi-insulating   and

arsenic-ion-implanted GaAs photoconductive antennas with 1.5-cm aperture size under various pump fluences and bias fields. We use fullwave model to explain the distinct terahertz radiation characteristics between both types of materials.

In the Chapter 5 we investigate the gap-dependent THz pulses from mid-size-gap multi-energy arsenic-ion-implanted GaAs photoconductive antennas in terahertz time-domain spectroscopy experiments. We demonstrate the carrier and field dynamics within the antennas. An explanation for the gap-dependent phenomenon is provided in this Chapter.

Chapter 6 summarizes the results obtained during this work, and provides an outlook on future prospects of the numerical simulation of THz radiation mechanism.
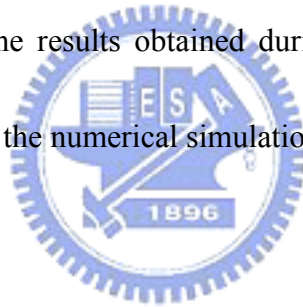
References

[1] A. S. Krishnagopal and V. Kumar, Radiat. Phys. Chem. **70**, 559 (2004).

[2] H. P. Freund and G. R. Neil, Proceedings of IEEE **87**, 782 (1999).

[3] R. Kompfner and N. T.Williams, Proc. IRE, **41**, 1602 (1953).

[4] T. Y. Chang and T. J. Bridges, Opt. Commun. **1**, 423 (1970).

[5] M. Inguscio, G. Moruzzi, K. M. Evenson, and D. A. Jennings, J. Appl. Phys. **60**, 161 (1986).

[6] D. D. Bicanic, B. F. J. Zuidberg, and A. Dymanus, Appl. Phys. Lett. **32**, 367 (1978).

[7] G. A. Blake, K. B. Laughlin, R. C. Cohen, K. L. Busarow, D-H. Gwo, C. A. Schmuttenmaer, D. W. Steyert, and R. J. Saykally, Rev. Sci. Instrum. **62**, 1693 (1991).

[8] M. C. Gaidis, H. M. Pickett, C. D. Smith, S. C. Martin, P. R. Smith, and P. H. Siegel, J. Appl. Phys. **60**, 161 (1986).

[9] R. F. Kazarinov and R. A. Suris, Fiz. Tekh. Poluprov. **5**, 797 (1971) [Sov. Phys. Semicond. 5, 707 (1971)]

[10] J. Faist, F. Capasso, D. L. Sivco, C. Sirtori, A. L. Hutchinson, and A. Y. Cho, Science 264, 553 (1994).

[11] M. Bass, Phys. Rev. Lett. **9**, 446 (1962).

[12] A. Bonvalet, Appl. Phys. Lett. **67**, 2907 (1995).

[13] O. S. Heavens and R. W. Ditchburn - Insight into Optics (1987)

[14] D. R. Grischkowsky, IEEE J. Sel. Top. Quantum Electron. **6**, 1122 (2000).

[15] M. Nagel, C. Meyer, H.-M. Heiliger, T. Dekorsy, H. Kurz, R. Hey, and K. Ploog, Appl. Phys. Lett. **72**, 1018 (1998).

[16] B. B. Hu and M. C. Nuss, *Opt. Lett*. **20**, 1716 (1995).

[17] G. Zhao, R. N. Schouten, N. van der Valk, W. T. Wenckebach, and P. C. M. Planken, Rev. Sci. Instrum.73, 1715 (2002).

[18] A. Dreyhaupt, S. Winnerl, T. Dekorsy, and M. Helm, App. Phys. Lett. **86**, 121114 (2005).

THz Region

3 cm	3 mm	300 μm	30 μm	3 μm	300 nm	30 nm	Wavelength

| Micro-Wave (SHF) | Millimeter Wave (EHF) | Submilli-meter Wave | Infrared | | Visible | Ultraviolet | |

10 GHz	100 GHz	1 THz	10 THz	100 THz	1 PHz	10 PHz	Frequency

0.33 cm^{-1}	3.3 cm^{-1}	33 cm^{-1}	330 cm^{-1}	3300 cm^{-1}	33000 cm^{-1}		
41 μeV	410 μeV	4.1 meV	41 meV	410 meV	4.1 eV	41 eV	Energy
0.48 K	4.8 K	48 K	480 K	4800 K	48000 K		Temperature
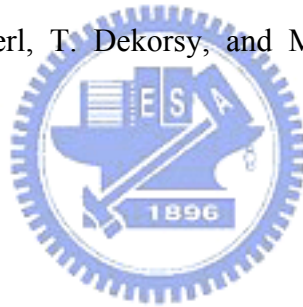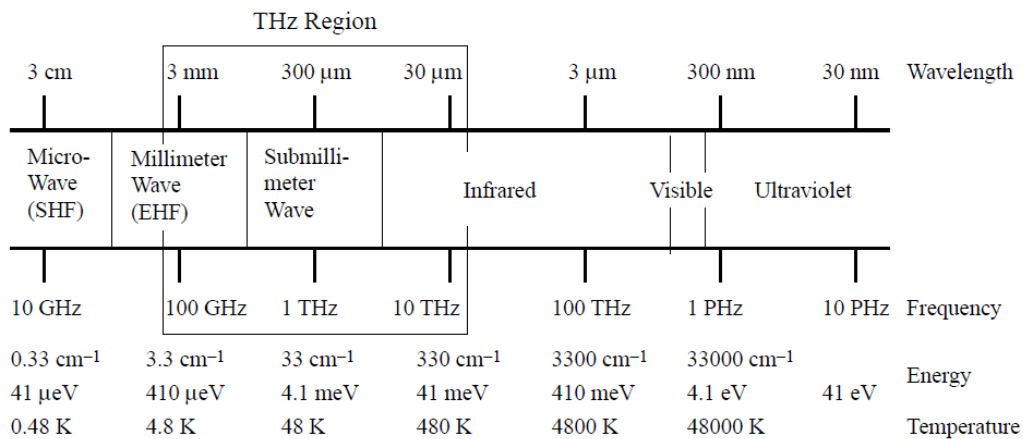
Fig. 1.1: THz radiation spectrum.*

Band-Pass Filter Optical Chopper Emitter (GaAs,InP)

OPA Pump Pulse Lens Lens V_b THz Pulse Parabolic Mirror

Regenerative Amplifier Probe Pulse Silicon Filter

Delay Line Pellicle Beam Splitter

Femtosecond Ti:sapphire Laser EO Sampling Setup
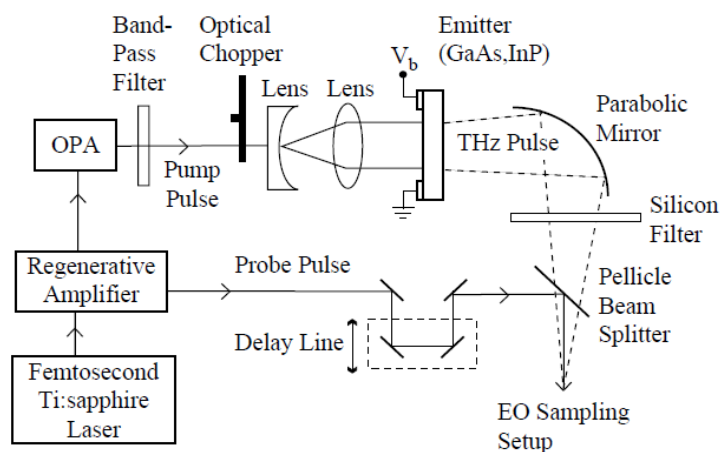
Fig. 1.2: Schematic of a THz-TDS system.*

*D. D. Toshiaki Hattori, *et al*. Science and Technology of Advanced Materials **6**, 649 (2005).

14

Chapter 2

Photoconductive antennas

Besides of FEL, QCL, and FSEOS, THz radiation also can be generated by employing femtosecond laser pulses to excite biased photoconductive (PC) antennas. These devices were first proposed by Auston *et al.* [1] and subsequently studied by many groups [2-4]. Typical PC antennas have two parallel metallic contacts deposited on the surface of a semiconductor as shown in Fig. 2.1. THz pulses are typically produced by conduction between two electrodes patterned on a semi-insulating GaAs (SI-GaAs), low temperature gallium arsenide (LT-GaAs), or other ion-implanted materials substrate. To generate THz radiation, a femtosecond laser pulse (often a titanium sapphire laser (Ti-Sapphire laser)) has to be focused onto the gap of the photoconductive antennas with a DC bias across the gap. Absorption of the laser pulse whose center frequency exceeds the bandgap of the semiconductor substrate generates free carriers there between the electrodes. The mechanism underlying the THz radiation is to quickly create photoexcited carriers between the externally biased contacts using an ultrafast laser pulse. The charge carriers are then quickly accelerated to the opposite electrodes by the bias field and lead to the formation of an electrical dipole due to the difference of mobility between electrons and holes. This acceleration

of the charge carriers by the external electric field generates an electromagnetic transient. That is, the bias–laser pulse combination allows these charge carriers to rapidly jump the gap, and the resulting fast temporal change in a transient current can generate a pulse of electromagnetic radiation in the THz frequency range. The performance of THz generation depends on the temporal shape of photo-induced current from charge acceleration. The far-field radiation $E_r(t)$ from the current distribution $J_s(t)$ ($\propto$ v, v is the drift velocity of the carriers) on the propagating axis of the radiation can be expressed by [5]

$$E_r(t) \cong -\frac{A}{4\pi\varepsilon_0 c^2 r} \frac{dJ_s(t)}{dt} \propto a, \tag{2.1}$$

where A is the area of the emitter carrying the current distribution and a is acceleration of the carriers. Since the THz radiation in the far field is proportional to the time derivative of the current density, the emitted THz transient depends crucially on the carrier drift velocity. As a result, the THz radiation field has a field shape proportional to the acceleration of the photo-excited carriers. Very short THz pulses (typically ~2 ps) are produced due to the rapid rise of the photo-induced current in the gap and in short lifetime materials such as LT-GaAs. This current may persist for only a few hundred femtoseconds or up to several nanoseconds, depending on the material of which the substrate is composed. This photoconductive antenna puts out a train of pulses, whose repetition frequency is the same as that of the femtosecond pump laser.

Pulse widths are on the order of 100 fs, with average powers below a few hundred nW

and a frequency spread of > 500 GHz. The pulse bandwidth is typically centered at

about 1 to 2 THz. The details of the spectrum can vary significantly, however,

depending on the design of the antenna and pump-laser power, pulse width and shape,

and configuration.

2.1 Antenna types

The features of the pump pulses will significantly affect the generated THz

radiation. Besides, the characteristics of THz radiation also depend on the designs of

photoconductive antennas. Several designs of antennas includes the dipoles, bow tie,

and coplanar strip line as shown in Fig. 2.1, or interdigitated structures, logarithmic

spiral antennas, and more sophisticated designs derived from microwave theory. The

most commonly used are the Hertzian dipole antenna which has been reported to have

an emission spectral distribution as high as 2 or 3 THz. The bow-tie antenna possesses

a wide frequency bandwidth, and is also used as a photoconductive antenna. For the

bow-tie antenna, increased radiation power was observed, although its emission

spectrum distributed at frequencies lower than dipole antennas. A unique

photoconductive source is the biased coplanar strip line, the metal and semiconductor

interface of which was excited with femtosecond laser pulses. The biased strip line

showed a very wideband emission spectrum (< 5 THz).

In 1997, M. Tani *et. al.* report a quantitative and systematic comparison of the emission properties of the photoconductive antennas [6]. In their experiments, they investigated the characteristics of THz radiation from several photoconductive antennas with three different designs (the three dipoles, bow tie, and coplanar strip line) and two different materials (semi-insulating GaAs (SI-GaAs) and low-temperature grown GaAs (LT-GaAs)). They found that the radiation spectra showed no significant difference for both materials under the same design. In addition, the pump-power dependencies of the radiation power showed saturation for higher pump intensities, which was more serious in SI-GaAs-based antennas than in LT-GaAs-based antennas.

2.2 Photoconductive materials

One of the essential device factors determining the efficiency of THz antennas is the photoconductive materials fabricated on the antenna. To generate high THz power, the photoconductive materials should have large carrier mobility. In addition, a high resistivity is desired for the materials so that the PC antennas can endure high bias field and thus obtain high THz radiation power. To fulfill these conditions, some approaches like doped and ion-implantation are applied to the PC materials. In the

following, we introduce three materials which are commonly fabricated on PC antennas.

2.2.1   Semi-insulating GaAs

One typical material fabricated on biased PC antennas is known as semi-insulating GaAs (SI-GaAs) [7]. By a variety of techniques one may produce SI-GaAs [8-10] with carrier lifetime τ_c of several picoseconds as a whole. The electrostatic property of SI-GaAs exhibits greatly reduced parasitic capacitance suitable for fast devices, and allows for integration and the implementation of monolithic microwave integrated circuits. SI-GaAs provides semiconductor qualities including thermal stability during epitaxial growth or anneal of ion-implanted active layer, absence of undesirable substrate active layer interface effects, no degradation of active layer properties by outdiffusion of impurities from substrate during thermal processing, and lowest possible density of crystalline defects. Undoped GaAs can be made semi-insulating by the addition of either oxygen or chromium to the melt. For our study, the SI-GaAs grown by the liquid encapsulated Czochralski method. Through a compensation of shallow acceptors by the intrinsic type of deep donor defect, EL2, the resistivity of SI-GaAs antenna is able to reach a value as high as the order of $10^{17} \Omega \bullet cm$. This high resistivity is about six orders of magnitude greater than

that of silicon and provides excellent isolation and substrate insulation. The resistivity

of the semiconductor can be controlled by counter doping with a deep-level impurity

that has a conductivity type opposite to that of the impurities introduced during

growth.

Hurd *et al*. [11] found that if pump light is incident upon SI-GaAs, the deep

traps within SI-GaAs lead to the photo-induced space charge at the electrode, and

therefore produce a space-charge field that screen the bias field and alter the transient

response of a PC antenna. The influence of space-charge field depends on the ratio of

the deep trap and shallow concentrations.

A particularly appealing phenomenon is provided by SI-GaAs when

a DC external bias is applied to the electrodes of a SI-GaAs antenna: an enhanced bias

field will form near the edge of the anode leading to an enhanced THz radiation when

femtosecond laser pump pulses are incident upon the edge of the anode [12].

2.2.2   Low-temperature grown GaAs

One usually makes use of molecular beam epitaxy method to grow GaAs thin

films on certain device. If the growth temperature during the film deposition is

reduced to about 200 - 300°C under arsenic overpressure an incorporation of excess

group V-atoms (As) occurs. Post annealing at temperatures above 600°C leads to the

nucleation of the excess arsenic in crystalline As precipitates of several nanometer size [13]. These As clusters act as burried Schottky barriers, form localized mid-gap states and are responsible for trapping of electrons and holes [14]. Other types of trapping centers are point defects, which are incorporated during the growth process. They are double donors, which consist of neutral and positively charged arsenic antisites. Energetically the antisite states are localized close to the center of the band gap [15]. The charged antisites as well as the precipitates are believed to influence the electrical properties of the material and the carrier relaxation after optical excitation [16]. Due to the fast carrier trapping the carrier lifetime of such low-temperature grown GaAs (LT-GaAs) is only about 250 ~ 500 fs [17] and depends critically on the growth temperature.
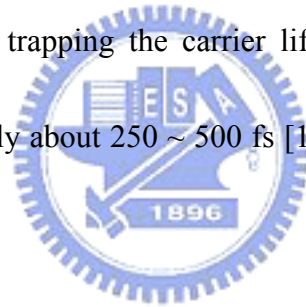
The trapping states may consist of Urbach tail states, which are located energetically close to the conduction band edge and the mid-gap states, mentioned above. The Urbach tail states are caused by disorder in the material, while the mid-gap states formed by the arsenic precipitates and the defects. In LT-GaAs the mid-gap state concentration can be as high as $10^{20}\,\mathrm{cm}^{-3}$ after growth [18], but decreases while the subsequent annealing to values of about $5\times10^{17}\,\mathrm{cm}^{-3}$ to $5\times10^{18}\,\mathrm{cm}^{-3}$ depending on growth and annealing temperature [19].

At high injected carrier densities a saturation of the trapping can occur and

therefore the slow recombination of the trapped carriers acts as a bottleneck for the depopulation of the bands via the point defects. High epitaxial GaAs crystals, grown under standard conditions (not LT-GaAs), exhibit a typical electron-hole recombination time of about 100 ~ 500 ps [18]. Therefore it is obvious that localized states in the energy gap due to defects or impurities (trapping states) can act as recombination centers for non-radiative processes, which change the recombination time substantially. If the density of trapped states is sufficiently high, carriers can tunnel through these centers to valence band. Because the trapping of carriers due to these localized states occurs very fast, the recombination time is reduced to about 10 ps. This effect is important for the development of fast PC antennas with sub-picosecond response times, which can be used for THz pulse emission [20]. With a bandwidth extending up to 5 THz and a good signal-to-noise ratio, such THz pulses are a promising tool for far-infrared spectroscopy of solids, liquids, and gases. However due to the introduced defects and impurities the statistical probability of scattering is increased and the mobility of the carriers is therefore reduced, what causes an increase in resistivity. This leads on the opposite side to a decrease in the sensitivity of the device to external electrical fields.

Compared to the SI-GaAs antenna, the LT-GaAs-based antenna has a larger bandwidth of THz radiation owing to its shorter carrier lifetime (< 1 ps), but its

disadvantage lies in the lack of reproducible property.

2.2.3 Arsenic-ion-implanted GaAs

Implanting ions into semi-insulating materials will significantly change their original resistivity and temperature stability, as well as optical properties, such as τ_c or absorption coefficient α_0. The value of τ_c for As-implanted [21-22] or LT-GaAs antenna [23] is as short as 1 ps or less; hence, it influences THz radiation characteristics, including: pulse shape, pulse duration, and bandwidth. Concerning the quantity α_0, its value is affected in the presence of impurity, bias field, or ion implantation. Nolte *et al*. pointed out that LT-GaAs exhibits an excess absorption relative to GaAs, depending on the growth conditions [24]. On the other hand, Lin *et al*. [25] found that the band edge of absorption coefficient α_0 of GaAs:As$^+$ increases from 6.2×10^3 to $2.2 \times 10^4 \text{cm}^{-1}$ for different dosages. Therefore, one can deduce that the absorption coefficient of semi-insulating materials tends to be altered after ion implantation.

In practical experiments, one can choose ions with different energy and dose for implanting the antenna's surface. The ion-implanted depth is determined by the ion energy, and can be calculated using the Stopping Range of Ions in Matter (SRIM)

software [26]. For As ion energy of 200 keV and 2 MeV, the implanted depths are about $0.1 \, \mu m$ and $1 \, \mu m$, respectively.

In addition to As^+, many groups have investigated THz devices based on GaAs implanted with H^+, N^+, and O^+. Salem *et al*. studied strip-line emitters based on GaAs:H, GaAs:N, GaAs:O, and also GaAs:As [27-28]. Recently, Winnerl *et al*. [29] studied THz emitters implanted with dual energy implants of N^+ and As^+ ions of various doses, and compared the results with that of SI-GaAs and LT-GaAs.

References

[1] D. H. Auston, K. P. Cheung, and P. R. Smith, Appl. Phys. Lett. 45, 284 (1984).

[2] D. H. Auston, Appl. Phys. Lett. 26, 101 (1975).

[3] G. Mourou, C. V. Stancampiano, A. Antonetti, and A. Orszag, Appl. Phys. Lett. 39, 295 (1981).

[4] X.-C. Zhang, B. B. Hu, J. T. Darrow, and D. H. Auston, Appl. Phys. Lett. 56, 1011 (1990).

[5] J. T. Darrow, X.-C. Zhang, D. H. Auston, and J. D. Morse, IEEE J. Quantum Electron. 28, 1607 (1992).

[6] M. Tani, S. Matsuura, K. Sakai, and S. Nakashima, Appl. Opt*s*. 36, 7853 (1997).

[7] M. S. Markram-Ebied, "Nature of EL2: The Main Native Midgap Electron Trap in VPE and Bulk GaAs," in semi-insulating III-V Materials, D. Look, Editor, Shiva Publishing Ltd., England (1984).

[8] N. G. Ainslie, S. E. Blum, and J. F. Woods, J. Appl. Phys. 33, 2391 (1961).

[9] G. R. Cronin and R. W. Haisty, J. Electrochem. *Soc.*, 111, 874 (1964).

[10]J. B. Mullin, R. J. Heritage, C. H. Holliday, and B. W. Straughan, J. Cryst. Growth, 3-4, 281 (1968).

[11]C. M. Hurd and W. R. McKinnon, J. Appl. Phys. 75, 596 (1994).

[12]S. E. Ralph and D. Grischkowsky, Appl. Phys. Lett. 59, 1972 (1991).

[13] M. Luysberg, H. Sohn, A. Prasad, P. Specht, Z. Lilienthal-Weber, E. R. Weber, J. Gebauer, R. Krause-Rehberg, J. Appl. Phys. 83, 561 (1998)

[14] U. Siegner, R. Fluck, G. Zhang, U. Keller, Appl. Phys. Lett. 69, 2566 (1996)

[15] G. D. Witt, Mater. Sci. Eng. B 22, 9 (1993)

[16] G. Segschneider, F. Jacob, T. Löffer, H. G. Roskos, S. Tautz, P. Kiesel, G. Döhler, Phys. Rev. B 65, (2002)

[17] M. Tani, K. Sakai, H. Abe, S. Nakashima, H. Harima, M. Hangyo, Y. Tokuda, K. Kanemoto, Y. Abe, N. Tsukada, Jpn. J. Appl. Phys. 1 33, 4807 (1994).

[18] A. Othonos, J. Appl. Phys. 83, 1789 (1998)

[19] D. C. Look, D. C. Walters, G. D. Robinson, J. R. Sizelove, M. G. Mier, C. E. Stutz, J. Appl. Phys. 74, 306 (1993)

[20] P. R. Smith, D. H. Auston, M. C. Nuss, IEEE J. Quantum Electron. 24, 255 (1988)

[21] M. Tani, K. Sakai, H. Abe, S. Nakashima, H. Harima, M. Hangyo, Y. Tokuda, K. Kanamoto, Y. Abe, and N. Tsukada, Jpn. J. Appl. Phys. 33, 4807 (1994).

[22] S. Gupta, J. F. Whitaker, and G. A. Mourou, IEEE J. Quantum Electron. 28, 2464 (1992).

[23] Wang, H.-H. Grenier, P. Whitaker, J. F. Fujioka, H. Jasinski, J. Liliental-Weber, Z. IEEE J. Selected Topics in Quantum Electron. 2, 630 (1996).

[24] D. D. Nolte, W. Walukiewicz, and E. E. Haller, Phys. Rev. Lett. 59, 501 (1987).

[25] G.-R, Lin, C,-C, Hsu, J. Appl. Phys. 89, 1063 (2001).

[26] J. F. Ziegler and J. P. Biersack, available online at http://www.srim.org.

[27] B. Salem, D. Morris, Y. Salissous, V. Aimez, S. Charlebois, M. Chicoine, and F. Schiettekatte, J. Vac. Sci. Technol. A 24, 774 (2006).

[28] B. Salem, D. Morris, V. Aimez, J. Beerens, J. Beauvais, and D. Houde, J. Phys. Condens. Matter 17, 7327 (2005).

[29] S. Winnerl, F. Peter, S. Nitsche, A. Dreyhaupt, B. Zimmermann, M. Wagner, H, Schneider, M. Helm, and Klaus Kohler, J. Selected Topics in Quantum Electron. 14, 449 (2008).
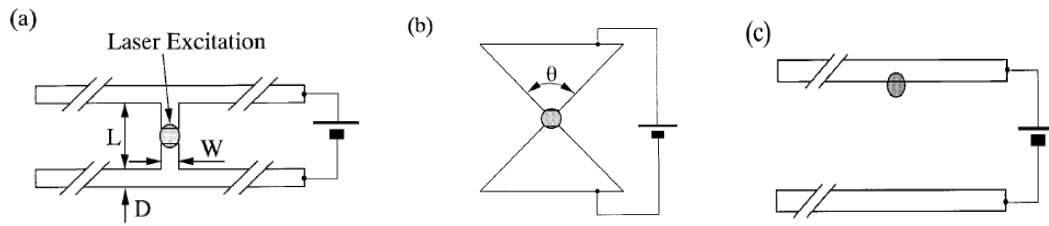
Fig. 2.1: Schematic view of (a) the photoconductive dipole antenna, (b) the bow-tie

antenna, and (c) the photoconductive strip line.*

*M. Tani, S. Matsuura, K. Sakai, and S. Nakashima, Appl. Opt*s*. 36, 7853 (1997).
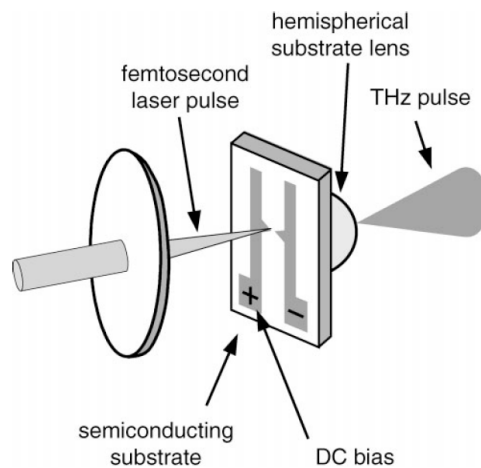
Fig. 2.2: Schematic of an Auston antenna, used to generate single-cycle bursts of THz

radiation. A subpicosecond optical pulse excites the semiconducting substrate

in a region between two biased electrodes. This radiation is coupled into free

space using a hemispherical substrate lens.*

*T. D. Dorney, M. J. Rossow*z*, W. W. Symes, and D. M. Mittleman*z*, Geophysics, 68, 308 (2003).

Chapter 3

Modeling of terahertz radiation from photoconductive antennas

Understanding the physics critical to the emission efficiency of THz antennas will allow greater control and wider applicability of THz radiation. Previously, Taylor *et al*. [1-2] used the current-surge model to explain several characteristics of large-aperture PC antennas, including: THz pulse width, saturation, and pump wavelength dependence. In their model, the formation of THz pulses is associated with the carrier dynamics in PC material, and the time-dependent THz radiation is proportional to the time derivative of the surface photocurrent. In 1996, Taylor *et al*. [3] used the drift-Poisson model to reproduce the bipolar THz radiation waveforms generated from different gap size of PC antennas. In their numerical simulation, they found that the negative peak of THz waveform becomes obvious if the pump fluence increases gradually. They attribute the formation of bipolar waveforms to the space-charge bias field screening effect, depending on the pump fluence and photoexcited carrier concentration.

In the following, we describe four theoretical models, including current-surge, Drude-Lorentz, drift-Poisson, and fullwave model. These models are usually adopted to interpret the characteristics of THz radiation.

3.1 Current surge model

This model assumes that the transient surface conductivity $\sigma_s(t)$ grows rapidly when an antenna is excited by a sub-picosecond optical pulse [4]:

$$\sigma_s(t) = \frac{q(1-R)}{h\nu} \int_{-\infty}^{t} \mu(t-t')I_{opt}(t')\, e^{-\frac{t-t'}{\tau_c}}\, dt' \qquad (3.1.1)$$

where R is the optical reflectivity of the illuminated area, $\mu(t)$ is the carrier mobility, $I_{opt}(t)$ is the optical pump pulse intensity, $h\nu$ is the photon energy, and τ_c is the lifetime of the excited carriers. Or, for the peak surface conductivity:

$$\sigma_s(t) = \frac{q(1-R)}{h\nu}\mu_1 F_{opt}, \qquad (3.1.2)$$

where μ_1 is the value of the time-dependent mobility at the moment of maximum σ_s and F_{opt} is the incident optical fluence.

In reality, the response of the photoconductor is slower than the rise time of the intensity of the excitation laser pulse because it takes up to several picoseconds for the transient mobility $\mu(t)$ to reach its quasi equilibrium value.

Solving the Maxwell equations and taking into account the finite size of the emitter, one obtains for the radiated field $E_r(t)$:

$$E_r(t) = -E_b \frac{\sigma_s(t)\eta_0}{\sigma_s(t)\eta_0 + 1 + N}, \qquad (3.1.3)$$

where E_b is the applied bias electrical field, $\eta_0 = 1/\varepsilon_0 c = 376.7\Omega$ is the impedance

of free space, and N is the refractive index of the semiconductor. Eq. (3.1.3) contains

the near-THz field screening effect, and its derivation will be detailed in Chapter 4.

By the Eq. (3.1.3), two important points should be noted:

(1) the radiated THz field E_r should raise linearly with the increase of the

applied bias voltage at least in the area of the Ohm's law validity. At very high

bias fields, the field dependence of the surface conductivity σ_s have to be

taken into account,

(2) E_r increases and then saturates as the incident optical fluence grows.

3.2 Drude-Lorentz model

One usually use a simple one-dimensional Drude-Lorentz model to describe the

behavior of the photo-excited carriers [5]. In Drude-Lorentz model, the current

density is given by

$$j = -qn_f v \qquad (3.2.1)$$

where n_f is the carrier density and v the velocity averaged over the carrier

distribution. The contribution by the holes is ignored for simplicity since their

contribution is very minor due their much larger effective mass. The change in carrier density over time can be described by:

$$\frac{dn_f}{dt} = -\frac{n_f}{\tau_c} + G(t) \qquad (3.2.2)$$

Here τ_c is the carrier lifetime, and $G(t)$ the photo-generation rate decided by the optical pump pulse. The motion of these generated carriers is slowed down by scattering, and their velocities can be described as:

$$\frac{dv}{dt} = -\frac{v(t)}{\tau_r} + \frac{q}{m^*} E_l(t) \qquad (3.2.3)$$

Where m^* is the effective mass of the carriers, E_l is the local field at the position of the carriers and τ_r the momentum relaxation time. If E_l is constant, it follows,

$$v(t) = v(0)e^{-t/\tau_r} + \frac{q\tau_r E_l}{m^*}[1 - e^{-t/\tau_r}] \qquad (3.2.4)$$

When an electron (charge $-q$) separates from a hole (charge $+q$), a dipole is formed with magnitude $\mu = -qz$. The negative sign indicates its direction is pointing toward the hole and its position z is found by integrating equation (3.2.4). The polarisation density is therefore given by:

$$P(t) = -qn_f z = \frac{q^2 \tau_r E n_f}{m^*} \int_0^t [1 - e^{-t/\tau_r}]d\tau. \qquad (3.2.5)$$

If we consider space-charge screening effect [6], the local field E_l results from combination of the biased E_b and space-charge E_s, that is:

$$E_l = E_b + E_s = E_b - \frac{P_s}{\eta\varepsilon}, \qquad (3.2.6)$$

where P_s is the polarization, η is a geometrical factor and ε is the dielectric

constant. The induced polarization changes with time, what can be described by [7]:

$$\frac{dP_s}{dt} = -\frac{P_s}{\tau_r} + j(t),$$ (3.2.3)

Combining Eqs. (3.2.1) – (3.23) and taking the time derivative, we obtain a second order differential equation:

$$\frac{d^2v}{dt^2} = -\frac{1}{\tau_r}\frac{dv}{dt} - \frac{\omega_p^2 v}{\eta} + \frac{qP_s}{m^*\eta\varepsilon\tau_r},$$ (3.2.3)

with the plasma frequency $\omega_p^2 = nq^2/m^*\varepsilon$. Solving these equations gives the information of the carrier dynamics via the parameter τ_c and τ_r necessary to describe the experimental results.

The Drude-Lorentz model is only applicable if the approximation of a free electron gas is valid. This is the case for a large number of excited electrons. Here we should note that one drawback of the Drude-Lorentz model is that it lacks the near-THz field screening effect. Another drawback is that it only considers the time-dependent behavior without including spatial factor. Nevertheless, the Drude-Lorentz model is still favorable for the simulation of THz radiation due to its simplicity and fast computation.

3.3 Drift-Poisson model

The drift-Poisson model consists of a set of fundamental equations which link together the electrostatic potential and the carrier densities, within some simulation

domain. These equations have been derived from Maxwell's laws and consist of Poisson's equation, the continuity equations and the transport equations. Poisson's equation relates variations in electrostatic potential to local charge densities. The continuity equations describe the way that the electron and hole densities evolve as a result of transport processes, generation processes, and recombination processes. We will introduce the Poisson and continuity equations in the following.

3.3.1 Poisson's equation

Poisson's equation belongs to a kind of elliptic equation, and it is of particular importance in electrostatics and Newtonian gravity. In electrostatics, Poisson's Equation relates the electrostatic potential V to the local space-charge density ρ :

$$\nabla \bullet (\varepsilon \nabla V) = -\rho \qquad (3.3.1)$$

where ε is the local electric permittivity.

We can write the electric field E in terms of an electric potential V with the gradient of the potential V.

$$\vec{E} = -\nabla V \qquad (3.3.2)$$

3.3.2 Carrier continuity equations

The continuity equations for electrons and holes are defined by the equations;

$$\frac{\partial n}{\partial t} = G_n - R_n + \frac{1}{q} \nabla \cdot J_n, \qquad (3.3.3)$$

$$\frac{\partial p}{\partial t} = G_p - R_p - \frac{1}{q} \nabla \cdot J_p, \qquad (3.3.4)$$

Where n and p are the electron and hole concentration, J_n and J_p are the electron and hole current densities, G_n and G_p are the photogeneration rates for electrons and holes, R_n and R_p are the recombination rates for electrons and holes, and q is the magnitude of the charge on an electron.

Derivations based upon the Boltzmann transport theory have shown that the current densities in the continuity equations may be approximated by a drift-diffusion model. In this case the current densities are expressed as:

$$J_n = -q\mu_n n \nabla V \qquad (3.3.5)$$

3.4 Fullwave model

Basic equations for fullwave analysis are three-dimensional Maxwell curl equations, including conductive current components. Although Boltzmann's transport equation for electrons may, in a strict sense, be solved for subpicosecond regions, current-continuity equations based on drift-diffusion for both electrons and holes are used as first-order approximations. These equations are

$$\nabla \times E = -\mu \frac{\partial H}{\partial t}, \qquad (3.4.1)$$

$$\nabla \times H = J_n + J_p + \varepsilon \frac{\partial E}{\partial t}, \qquad (3.4.2)$$

$$\frac{\partial n}{\partial t} \; = \; G_n \; - \; R_n \; + \; \frac{1}{q} \, \nabla \cdot J_n, \tag{3.4.3}$$

$$\frac{\partial p}{\partial t} \; = \; G_p \; - \; R_p \; - \; \frac{1}{q} \, \nabla \cdot J_p, \tag{3.4.4}$$

$$J_n \; = \; q \mu_n n \nabla V \; + \; q D_n \nabla n \tag{3.4.5}$$

$$J_p \; = \; q \mu_p p \nabla V \; - \; q D_p \nabla p \tag{3.4.6}$$

where E and H stand for the electric and magnetic field, n and p are the electron and

hole concentrations, respectively, R and G are the recombination and generation rates,

respectively, μ is the magnetic permittivity, $\mu_{n,p}$ and $D_{n,p}$ refer to the electron (hole)

mobility and diffusion coefficient.

Sano *et al*. [8] adopt Eqs. (3.4.1) - (3.4.6) to analyze the propagation of an

electromagnetic wave within a PC dipole antenna with respect to different direction.

In 2003, Hughes *et al*. [9] apply a vector approach to simulate the THz transients

generated from a PC dipole antenna.
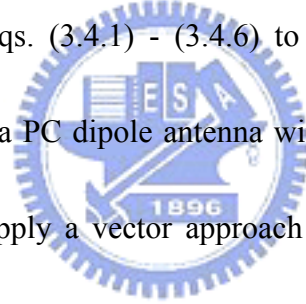
3.5 Numerical algorithm for Poisson's equation

In the drift-Poisson and fullwave model, Poisson's equation plays an important

role in determining the profile of the electrostatic field of a THz antenna. Hence it is a

essential project for us to solve Poisson's equation by a proper numerical algorithm.

As we know, most of the electrostatic problems that come up in the real world are too

hard to solve with formulas, or even by Fourier series. For such problems the most

widely used method is to use a spatial grid. This can be done in 1, 2, or 3 dimensions, but the technique will be illustrated here in 2 dimensions

Suppose that you have an electrostatics problem in infinitely-long geometry so that one of the dimensions (say the y dimension) is irrelevant. Then the equation that must be solved is Poisson's equation in the two dimensions x and z:

$$\frac{\partial^2 V}{\partial x^2} + \frac{\partial^2 V}{\partial z^2} = -\frac{\rho}{\varepsilon_0} \quad , \tag{3.5.1}$$

subject to boundary conditions on the electrostatics potential V. In THz antennas, x usually stands for the gap direction, z refers to the direction of pump pulse propagation (or penetration depth). To solve this problem on a grid we first choose a rectangular computation region bounded in x by $x_{\min}$ and $x_{\max}$ and in z by $z_{\min}$ and $z_{\max}$. We then subdivide the x interval into N_x subintervals and the z interval into N_z subintervals to form a grid in the x-z plane. The x-subintervals have length $\Delta x = (x_{\max} - x_{\min})/N_x$ and the z-subintervals have length $\Delta z = (z_{\max} - z_{\min})/N_z$. Because the ends of the intervals are included the grid is of size $(N_x+1) \times (N_z+1)$ and the ($x_i ; z_k$) position of the grid point labeled by (i, k) is given by

$$x_i = x_{\min} + (i-1)\Delta x \qquad ; \qquad z_k = z_{\min} + (k-1)\Delta z \tag{3.5.2}$$

We now use this grid to solve Poisson's equation by writing down an approximation to it at each grid point. The approximation is obtained by using the centered-difference approximation to the second derivative:

$$\frac{\partial^2 V}{\partial x^2}\Big|_{(i,k)} \approx \frac{V_{i+1,k} - 2V_{i,k} + V_{i-1,k}}{\Delta x^2} \quad, \tag{3.5.3}$$

$$\frac{\partial^2 V}{\partial z^2}\Big|_{(i,k)} \approx \frac{V_{i,k+1} - 2V_{i,k} + V_{i,k-1}}{\Delta z^2} \quad, \tag{3.5.4}$$

where $V_{i,j} = V(x_i, z_k)$. Substituting Eqs. (3.5.3) and (3.5.4) into Eq. (3.5.1), the grid

version of Poisson's equation is approximately given by

$$\frac{V_{i+1,k} - 2V_{i,k} + V_{i-1,k}}{\Delta x^2} + \frac{V_{i,k+1} - 2V_{i,k} + V_{i,k-1}}{\Delta z^2} = -\frac{\rho_{i,k}}{\varepsilon_0} \quad, \tag{3.5.5}$$

It is by no means clear that this approximation is useful just by looking at it, but a

large number of clever people have discovered over the years that it is useful to

rewrite this equation by solving for $V_{i,j}$:

$$V_{i,k} = \left(\frac{2}{\Delta x^2} + \frac{2}{\Delta z^2}\right)^{-1}\left[\frac{V_{i+1,k} + V_{i-1,k}}{\Delta x^2} + \frac{V_{i,k+1} + V_{i,k-1}}{\Delta z^2} + \frac{\rho_{i,k}}{\varepsilon_0}\right] \quad, \tag{3.5.6}$$

The reason that this is a good idea is that it turns out that in this form the equation can

be solved by iteration, just as we can solve the equation $x = \cos x$ by iteration:

$$x_{n+1} = \cos x_n \quad, \tag{3.5.7}$$

where n counts successive iterations. If you haven't seen this trick before, try it. Start

with 1, then calculate cos(1), then cos(cos(1)), etc.. After doing this a bunch of times

you will get the number 0.7391, which solves the equation $x = \cos x$. The same trick

works for Eq. (3.5.6): make a guess for $V_{i,j}$ across the whole grid, compute the right

hand side of Eq. (3.5.6) from this guess and use the equation to get a new set of values

for $V_{i,j}$. Rewriting Eq. (3.5.6) in the symbolic form
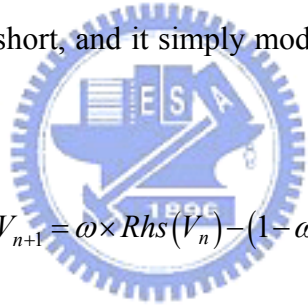
$$V = Rhs(V) \quad, \tag{3.5.8}$$

38

this iteration scheme can be written as

$$V_{n+1} = Rhs(V) \quad , \qquad\qquad (3.5.9)$$

Amazingly, this actually works and is called successive relaxation. It is, however, painfully slow. But the people who discovered this trick also discovered how to improve it in various ways and have, in fact, developed an entire field of study based on this problem. We will just discuss here the simplest improvement that is useful, but if you would like to see why this really works and be introduced to even better methods. The simple, but effective, improvement we will use is called Successive Over-Relaxation, or SOR for short, and it simply modifies the iteration scheme given above in the following way:

$$V_{n+1} = \omega \times Rhs(V_n) - (1-\omega)V_n \quad , \qquad\qquad (3.5.10)$$

where ω is a number between 1 and 2. Using $\omega = 1$ is just simple relaxation and using $\omega = 2$ makes the iteration unstable so that V goes to infinity. But between these two extremes there is an optimum value of ω that makes the iteration converge much better than simple relaxation. You can get close to the best value of ω by experimenting, but here is some rough guidance. For a 20×20 grid use $\omega = 1.7$; for a 30×30 grid use $\omega = 1.8$; for a 40×40 grid use $\omega = 1.85$; and for a 50×50 grid use $\omega = 1.9$.

This above methods work fine for finding $V(x, z)$ at the defined grid points,

but what if we want $V(x, z)$ at some arbitrary point, then we have to interpolate the data in two dimensions. There are lots of ways to do this, but the simplest (and usually adequate, but least accurate) way is bilinear interpolation. In this scheme you begin by finding the four grid points that surround the point (x, z) at which you want to find the potential $V(x, z)$. In what follows these points will designated by the symbols 00, 10, 01, and 11 denoting, respectively, the lower left point, the lower right point, the upper right point, and the upper left point.

Generally, the electric field E is useful for the practical calculation. Now suppose we have obtained $V(x, z)$, we have to find E at all the grid points, and then you can use bilinear interpolation on the x and z-components of E just as it was described for V. To find the components of E recall that

$$E = -\nabla V = \mathrm{i}\frac{\partial V}{\partial x} - \mathrm{j}\frac{\partial V}{\partial z} \quad , \qquad\qquad (3.5.11)$$

So we just need to know how to numerically compute these partial derivatives using values of V on the grid. This is most easily accomplished by using a simple centered difference approximation:

$$\frac{\partial V}{\partial x}\Big|_{(i,k)} \approx \frac{V_{i+1,k} - V_{i-1,k}}{2\Delta x} \qquad ; \qquad \frac{\partial V}{\partial z}\Big|_{(i,k)} \approx \frac{V_{i,k+1} - V_{i,k-1}}{2\Delta z} \qquad (3.5.12)$$

3.6 Method of lines

A common approach to finding numerical solutions of time-dependent partial differential equations (PDEs) is to use the method of lines (MOL). This technique involves reducing an initial boundary value problem (IBVP) to a system of ordinary differential equations (ODEs) in time through the use of a discretization in space. This system of ODEs, which takes the form of an initial value problem (IVP), can then be solved using standard software such as MATHEMATICA or MAPLE. The spatial discretization may take many forms (e.g., finite difference[10-12], finite element [13-14] or finite volume) but the resulting ODE system can be solved using standard initial value problem software, which may use a variable time-step/variable order approach with time local error control.
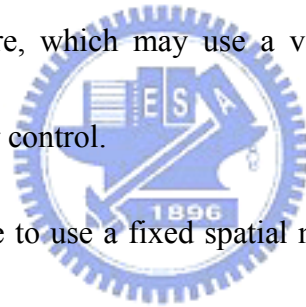
Although it is possible to use a fixed spatial mesh in such an approach it has long been recognized that adapting the spatial mesh offers important advantages as regards the efficiency and accuracy of the solution process, particularly for problems with moving or highly localized features. There are in general two approaches used to modify a spatial mesh. One approach is to continuously move the grid in time often by solving an extra set of differential equations to determine the mesh point positions.

Spatial derivative approximations

Before employing method of lines for PDEs, we have to discretize the spatial

derivative in equations with finite differences or finite element method. The essence

of the concept of finite differences is based on a standard definition of the first

derivative:

$$f'(x_i) \equiv \lim_{h \to 0} \frac{f(h+x_i)-f(x_i)}{h} \quad , \tag{3.6.1}$$

where instead of passing to the limit as h approaches zero, the finite spacing to the

next adjacent point, $x_{i+1} = x_i + h$, is used so that you get an approximation.

$$f'(x_i) = \frac{f(h+x_i)-f(x_i)}{h} \quad , \tag{3.6.2}$$

We also call Eq. (3.6.11) as *stencil*. The difference formula can also be derived from

Taylor's formula,

$$f(x_{i+1}) \approx f(x_i)+hf'(x_i)+\frac{h^2}{2}f''(\xi_i); x_i < \xi_i < x_{i+1} \quad , \tag{3.6.3}$$

which is more useful since it provides an error estimate (assuming sufficient
smoothness)

$$f'(x_i) = \frac{f(h+x_i)-f(x_i)}{h} - \frac{h}{2}f''(\xi_i) \quad , \tag{3.6.4}$$

An important aspect of this formula is that ξ_i must lie between x_i and x_{i+1} so that the

error is local to the interval enclosing the sampling points. It is generally true for finite

difference formulas that the error is local to the stencil, or set of sample points.

Typically, for convergence and other analysis, the error is expressed in asymptotic

form:

$$f'(x_i) = \frac{f(h+x_i)-f(x_i)}{h} + O(h) \quad , \tag{3.6.5}$$

This formula is most commonly referred to as the first-order forward difference. The

backward difference would use x_{i-1}.

Taylor's formula can easily be used to derive higher-order approximations. For example, subtracting

$$f(x_{i+1}) = f(x_i) + hf'(x_i) + \frac{h^2}{2}f''(x_i) + O(h^3) \quad, \qquad (3.6.6)$$

from

$$f(x_{i-1}) = f(x_i) - hf'(x_i) + \frac{h^2}{2}f''(x_i) + O(h^3) \quad,$$

and solving for $f(x_i)$ gives the second-order centered difference formula for the first derivative,

$$f'(x_i) = \frac{f(x_{i+1}) - f(x_{i-1})}{2h} + O(h^2) \quad, \qquad (3.6.7)$$

If the Taylor formulas shown are expanded out one order farther and added and then combined with the formula just given, it is not difficult to derive a centered formula for the second derivative.

$$f''(x_i) = \frac{f(x_{i+1}) - 2f(x_i) + f(x_{i-1})}{h^2} + O(h^2) \quad, \qquad (3.6.8)$$

Note that the while having a uniform step size h between points makes it convenient to write out the formulas, it is certainly not a requirement. For example, the approximation to the second derivative is in general

$$f''(x_i) = \frac{2(f(x_{i+1})(x_{i-1} - x_i) + f(x_{i-1})(x_i - x_{i+1}) + f(x_i)(x_{i+1} - x_{i-1}))}{(x_{i-1} - x_i)(x_{i-1} - x_{i+1})(x_i - x_{i+1})} + O(h) \quad, \qquad (3.6.9)$$

where h corresponds to the maximum local grid spacing. Note that the asymptotic order of the three-point formula has dropped to first order; that it was second order on a uniform grid is due to fortuitous cancellations.

In general, formulas for any given derivative with asymptotic error of any chosen order can be derived from the Taylor formulas as long as a sufficient number of sample points are used. However, this method becomes cumbersome and inefficient beyond the simple examples shown. An alternate formulation is based on polynomial interpolation: since the Taylor formulas are exact (no error term) for polynomials of sufficiently low order, so are the finite difference formulas. It is not difficult to show that the finite difference formulas are equivalent to the derivatives of interpolating polynomials. For example, a simple way of deriving the formula just shown for the second derivative is to interpolate a quadratic and find its second derivative (which is essentially just the leading coefficient).

3.7 Boundary conditions

In solving the fullwave model, the boundary conditions at an interface of different materials play an important role, and will significantly determine the solutions of a set of nonlinear partial equations. Hence we should assume carefully appropriate boundary conditions in order to obtain correct solutions.

In practical calculations, it is often essential to introduce artificial boundaries to limit the area of computation. Here we develop a systematic method for obtaining a hierarchy of local boundary conditions at these artificial boundaries. These boundary

conditions not only guarantee stable difference approximations, but also minimize the

(unphysical) artificial reflections that occur at the boundaries.

At the edges of the grid, the stencil applied at points in the interior of the grid

typically cannot be used. Some type of rule for handling the edge points is required.

There are several different types of boundary conditions:

(1) Dirichlet: $f \mid_{xi} = 0$, where xi is a boundary point. Sometimes instead of

vanishing of f, the unknown may be equal to some given function at the

boundary.

(2) Neumann: $\dfrac{\partial f}{\partial n} \mid_{xi} = 0$, where n represents the coordinate that is normal to the

boundary. Implementing this boundary condition on the grid using a forward

difference approximation for the derivative leads to the relationship $x_1 = x_2$,

where x_1 is a point on the grid boundary.

(3) Mixed: A linear combination of the function f and its normal derivative are set

to a constant.

(4) Absorbing boundary condition (ABC): This type of boundary condition is very

important in applications of the finite difference method, and is adopted by us

in our simulation.

Most electromagnetic problems involve unbounded regions, which cannot be

modeled computationally. One option is to use one of the above boundary

conditions and make the simulation region very large, and terminate the simulation before reflections from the boundary perturb the solution in the region of interest. The drawback of this approach is that the larger the simulation region, the greater the computational cost of the simulation. A better approach is to use a boundary condition that absorbs waves and reflects as little energy as possible. This is the computational analogue of an anechoic chamber. There are several types of ABCs, including:

♦   One-way wave equation. These are easy to implement but imperfect in 2D and higher dimensions.

♦   Perfectly matched layer with loss.

♦   Surface integral equation on the boundary (MOM-TDIE).
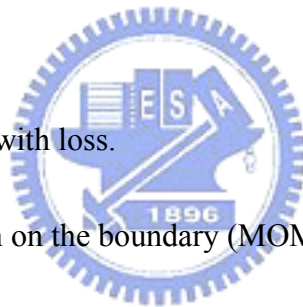
Boundary conditions may also be required at material interfaces inside the simulation region.

Hyperbolic PDEs

Here we consider the simplest hyperbolic PDE - the 1D wave equation for function f:

$$\frac{\partial^2 f(x,t)}{\partial x^2} = \frac{1}{c^2}\frac{\partial^2 f(x,t)}{\partial t^2} \qquad (3.7.1)$$

One physical problem that is modeled by this PDE is a planar time-domain current

source that varies in intensity only in the x direction. Since the source varies only in the x direction, the radiated electric field also only varies in the x direction, and the components $E_y(x,t)$ and $E_z(x,t)$ both satisfy Eq. (3.7.1) where the source term is zero. In order to apply the finite difference method to the wave equation, difference approximations for the derivatives are required. The stencil for the second derivative in x is

$$\frac{\partial^2 f(x)}{\partial x^2} \simeq \frac{\partial}{\partial x}\left[\frac{f(x+\Delta x)-f(x-\Delta x)}{\Delta x}\right] \simeq \frac{f(x+\Delta x)-2f(x)+f(x-\Delta x)}{(\Delta x)^2} \qquad (3.7.2)$$

where the t dependence of u(x; t) is suppressed for brevity. The stencil for the right-hand side of (3.2) is very similar. Substituting difference approximations into the wave equation leads to

$$r^2\left[f(x+\Delta x,t)-2f(x,t)+f(x-\Delta x,t)\right]=f(x,t+\Delta t)-2f(x,t)+f(x,t-\Delta t)$$

$$(3.7.3)$$

where $r = c\Delta t / \Delta x$.

If we define a grid by the points $x_n=(m-1)\Delta x$ and $t_n=(n-1)\Delta t$, then $f(x_m,t_n)=f\big((m-1)\Delta x,(n-1)\Delta t\big)$. As a shorthand notation, we write this as f_m^n. The difference equation becomes

$$r^2\left[f_{m+1}^n - 2f_m^n + f_{m-1}^n\right] = f_m^{n+1} - 2f_m^n + f_m^{n-1} \qquad (3.7.4)$$

Now, we can solve this for f_m^{n+1} to obtain an explicit finite difference method:

$$f_m^{n+1} = r^2\left[f_{m+1}^n - 2f_m^n + f_{m-1}^n\right] + 2f_m^n - f_m^{n-1} \qquad (3.7.5)$$

This algorithm is known as the finite difference time domain method (FDTD), because a time coordinate is involved.

Because the wave equation involves time, part of the boundary condition required for the finite difference approach is actually a boundary condition in time, or an initial condition. Since the PDE involves a second order time derivative, initial conditions at two time steps are required. This means that f_m^1 and f_m^2 must be specified as given functions. One common situation is the initial condition $f_m^1 = f_m^2 = 0$, and a source is applied at one of the spatial boundaries of the region.

A simplest boundary condition is Dirichlet: $f(0,t) = 0$ and $f(G,t) = 0$, where [0, G] is the simulation region. The Neumann condition is implemented by setting the endpoint value equal to the point next to it: $f_2^n = f_1^n$, and similarly for the right boundary point.

An absorbing boundary condition can be obtained by discretizing the one-way wave equation at the endpoints of the region. This is known as the Mur boundary condition. At the right-hand side, we enforce the PDE

$$\frac{\partial f(x,t)}{\partial x} = -\frac{1}{c}\frac{\partial f(x,t)}{\partial t} \qquad (3.7.6)$$

This equation has solutions of the form $f(x,t) = f_0(x - ct)$, which is a wave of arbitrary shape moving to the right as time increases. This allows waves to move out of the simulation region without reflection. We have to be careful in discretizing this

equation, because the approximations for the spatial and time derivatives in the

one-way wave equation need to be evaluated at the same point.

There are two types of sources that can be used in the FDTD method, hard

sources and soft sources. A hard source simply sets the value of the field at one or

more grid points equal to a specified function of time, and so is a type of Dirichlet

boundary condition. This corresponds to an EM problem in which the electric field at

some point is known, and we wish to find the values of the radiated field at other

points. One property of a hard source is that waves propagating towards the source are

reflected by the source. A soft source corresponds to an impressed electric current. In

order to allow for a soft source, we must rederive (3.7.2) from Maxwell's equations. If

we take the curl of Faraday's law and substitute in Ampere's law, we obtain

$$\nabla \times \nabla \times E + \frac{1}{c^2}\frac{\partial E}{\partial t} = -\mu \frac{\partial J}{\partial t} \qquad (3.7.7)$$

where the light speed $c = 1/\sqrt{\mu\varepsilon}$, E and J are the electric field and current density,

respectively. If we use the vector calculus identity

$$-\nabla \times \nabla \times E + \nabla\left(\nabla \bullet E\right) = \nabla^2 E \qquad (3.7.8)$$

and assume that the permittivity is constant and the net electric charge is zero, so that

$\nabla \bullet D = \nabla \bullet E = 0$, then we arrive at the wave equation

$$\nabla^2 E - \frac{1}{c^2}\frac{\partial^2 E}{\partial t^2} = \mu \frac{\partial J}{\partial t} \qquad (3.7.9)$$

Provided that there is a net charge density ρ in space, it will be obtained that

$\nabla \cdot E = \rho / \varepsilon$, then Eq. (3.7.7) becomes

$$\nabla^2 E - \frac{1}{c^2}\frac{\partial^2 E}{\partial t^2} = \mu \frac{\partial J}{\partial t} + \nabla \frac{\rho}{\varepsilon} \qquad (3.7.10)$$

If we consider two dimensional case (i.e. x and z direction), then Eq. (3.7.10) can be written as

$$\frac{\partial^2 E}{\partial x^2} + \frac{\partial^2 E}{\partial z^2} - \frac{1}{c^2}\frac{\partial^2 E}{\partial t^2} = \mu \frac{\partial J}{\partial t} + \hat{x}\frac{\partial \rho}{\varepsilon \partial x} + \hat{z}\frac{\partial \rho}{\varepsilon \partial z} \qquad (3.7.11)$$

Assuming that $E = E_x(x,z)\hat{x} + E_z(x,z)\hat{z}$, then Eq. (3.7.11) is divided into two equations as follows:

$$\frac{\partial^2 E_x}{\partial x^2} + \frac{\partial^2 E_x}{\partial z^2} - \frac{1}{c^2}\frac{\partial^2 E_x}{\partial t^2} = \mu \frac{\partial J_x}{\partial t} + \frac{\partial \rho}{\varepsilon \partial x} \qquad (3.7.12)$$

$$\frac{\partial^2 E_z}{\partial x^2} + \frac{\partial^2 E_z}{\partial z^2} - \frac{1}{c^2}\frac{\partial^2 E_z}{\partial t^2} = \mu \frac{\partial J_z}{\partial t} + \frac{\partial \rho}{\varepsilon \partial z} \qquad (3.7.13)$$

For a problem in which the current density vector is in one direction only, and the source varies also only in one direction, this reduces to a 1D wave equation of the same form as Eq. (3.7.1) but with a forcing function determined by the current source.

3.8 Programming methodologies

Basically, there are three possible methods by which we could perform the numerical calculations which are going to crop up during this work.

Firstly, we could use mathematical software packages such as MATHEMATICA, MAPLE, MATLAB, or MATHCAD. The main advantage of these packages is that they facilitate the very rapid coding up of numerical problems.

However, these simulation tools all have the same disadvantage that they produce

executable code which is interpreted, rather than compiled. Compiled code is

translated directly from a high-level language into machine code instructions, which,

by definition, are platform dependent--after all, an Intel x86 chip has a completely

different instruction set to a Power-PC chip. Interpreted code is translated from a

high-level language into a set of meta-code instructions which are platform

independent. Each meta-code instruction is then translated into a fixed set of machine

code instructions which is peculiar to the particular hardware platform on which the

code is being run. In general, interpreted code is nowhere near as efficient, in terms of

computer resource utilization, as compiled code: i.e., interpreted code run a lot slower

than equivalent compiled code. Thus, although MATHEMATICA, MAPLE, and

MATLAB are ideal environments in which to perform relatively small calculations,

they are not suitable for full-blown research projects, since the code which they

produce generally runs far too slowly.
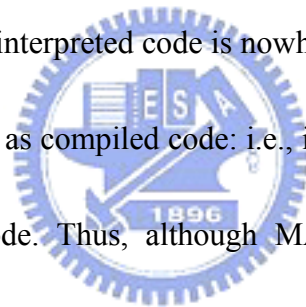
Secondly, we could write our own programs in a high-level language, but use

calls to pre-written, pre-compiled routines in commonly available subroutine libraries,

such as NAG, LINPACK, and ODEPACK, to perform all of the real numerical work.

This is the approach used by the majority of research physicists.

Thirdly, we could write our own programs--completely from scratch--in a high-level language. However, we should realize that, in many cases, pre-written library routines offer solutions to numerical problems which are pretty hard to improve upon. Here we do not suggest adopting this way.

In this thesis, we have opted the MATHEMATICA software to perform our numerical simulation since it can reduce much programming time without losing much execution efficiency. Its disadvantage is that one has to comprehend its programming language very deeply; otherwise, some useful usage will be hidden.

References

[1] A. J. Taylor, P. K. Benicewicz, and S. M. Young, Opt. Lett. 18, 1340 (1993).

[2] G. Rodriguez, S. R. Caceres, and A. J. Taylor, Opt. Lett. 19, 1994 (1994).

[3] G. Rodriguez and A. J. Taylor, Opt. Lett. 21, 1046 (1996).

[4] J. T. Darrow, Xi,-C. Zhang, D. H. Auston, and J. D. Morse, IEEE J. Quantum Electron. 28, 1607 (1992).

[5] P. K. Benicewicz, A. J. Taylor, Opt. Lett. 18, 1332 (1993).

[6] P. U. Jepsen, R. H. Jacobsen, S. R. Keiding, J. Opt. Am. B, 13, 2424 (1996)

[7] S. D. Brorson, J. Zhang, S. R. Keiding, Appl. Phys. Lett. 64, 2385 (1994).

[8] E. Sano and T. Shibata, IEEE J. Quantum Electron. **26**, 372 (1990).

[9] S. Hughes. M. Tani, and K. Sakai, J. Appl. Phys. **93**, 4880 (2003).

[10] W. H. Press, B. P. Flannery, S. A. Teukolsky, and W. T. Vetterling, *Numerical Recipes,* (Cambridge Univ. Press, Cambridge, MA. 1986).

[11] K. Z. Kunz and R. J. Luebbers, *The Finite Difference Time Domain Method for Electromagnetics* (CRC Press, Boca Raton, 1993).

[12] A. Taflove, *Computational Electrodynamics: The Finite-Difference Time-Domain Method* (Artech House, Boston, 1995).

[13] J. Jin, *The Finite Element Method in Electromagnetics* (Wiley, New York, 1993).

[14] F. Brezzi and M. Fortin, *Mixed and Hybrid Finite Element Methods*

(Springer-Verlag, New York, 1991).

Chapter 4

Large-aperture antennas

According to aperture size, a PC antenna with aperture size larger than 5 mm is classified as large-aperture (or large-area) antennas since its size is much larger than its radiation wavelength (~submillimeter). A typical configuration for a large-aperture biased antenna consists of two coplanar strip lines separated by 5 mm and above. Such an antenna can generate a giant THz radiation pulse with peak amplitude as high as 150 kV/cm when an expanded femtosecond laser beam is normally incident upon the antenna surface [1]. To increase THz emission efficiency, PC antennas with laterally structured emitter electrodes were employed [2-3]. Recently, Dreyhaupt *et al*. [4] reported a large-area PC THz emitter with an interdigitated electrode metal-semiconductor-metal structure and selective shadowing of optical excitation. Terahertz radiation with peak amplitude of 85 V/cm and bandwidth of about 2 THz were demonstrated by use of a high bias field [5-6]. High THz field amplitude is desirable for potential applications for sensing, imaging [7], telecommunications [8-9], and nonlinear spectroscopy [10]. If the carrier lifetime τ_c of PC material for fabrication of a large-aperture antenna is much longer than the pump pulse duration: τ_p, then the generated far-field THz pulse tends to exhibit a

unipolar waveform which is ideal for field ionization study [11], THz-field-induced

second-harmonic generation from molecular liquids [12], and real-time imaging.

A significant criterion for assessing the performance of a biased PC antenna is

its THz emission efficiency. In this regard, one can obtain insights by comparing the

dependence of peak THz amplitude E_r^{max} on pump fluence F or bias field E_b [13]. E_r^{max}

first grows rapidly with pump fluence for F below a characteristic fluence F_s, and then

ascends slowly and linearly above F_s. It was also shown that E_r^{max} scales linearly with

E_b up to a breakdown value. In practice, either the F or E_b dependence will vary with

different aperture size, pump spot size, or material properties.

We have investigated the optically excited THz radiation from PC dipole

antennas with 5-μm-gap fabricated on SI-GaAs and multi-GaAs:As$^+$ antennas [14]

and analyzed their characteristics by using the scaling rule. In this thesis, our study

extends to large-aperture antennas. Additionally, we analyze our experimental data by

use of the simulation results based on the formulism of nonlinear envelope and wave

equations.

4.1   Near-THz field screening effect

Some applications usually require high THz radiation power to induce the

material reaction. To reach this purpose, one will increase the pump fluence F of the

pulses incident upon the surface of a large-aperture antenna at a fixed bias. However, the radiated THz power will not be proportional to F as we expect. Instead, the radiated THz power will vary in a way that saturates at high F. This saturation behavior originates mainly from the near-THz field screening effect[14] that can be described by the scaling rule. The principle of the near-THz field screening effect can be analyzed using the basic Maxwell electromagnetic theory [15].

In Fig. 4.1 we plot a large-aperture antenna subjected to an external bias. The pump laser pulse illuminates the antenna at normal incidence. The antenna consists of a planar photoconductor with two parallel metallic electrodes. At the interface between the air and photoconductive material the inward and outward radiated electric fields, $E_{r,\text{in}}(t)$ and $E_{r,\text{out}}(t)$, the inward and outward radiated magnetic fields, $H_{r,\text{in}}(t)$ (pointing out of the page) and $H_{r,\text{out}}(t)$ (pointing into the page), are created due to the generation of transient surface current $J(t)$. These radiated fields are plane waves propagating away from the antenna's surface. Fig. 4.1 also depicts two orthogonal surfaces, l long by w wide, with corresponding contours, partially in the antenna. The surface in the plane of the page has unit normal n_y; the other perpendicular to this plane, unit normal n_x. From Maxwell's equations, relationships among these quantities can be derived. In spite of the time-dependent nature of the physical situation depicted in Fig. 1, we can show that the boundary conditions on the

electric and magnetic fields reduce to those of the steady state. The boundary

condition on the electric fields can be derived from Faraday's law,

$$\nabla \times E = -\frac{\partial B}{\partial t} = -\frac{\partial H}{\partial t} \qquad (4.1.1)$$

where, for simplicity, B is the magnetic induction assumed to be equal to the magnetic

field H, everywhere in space. From Stokes's theorem, we can integrate Eq. (4.1.1)

over a flat region perpendicular to the antenna surface and with unit normal, n_y,

(pointing out of the page),

$$\oint_C E \cdot dl = -\int_S \frac{\partial H}{\partial t} \cdot n_y \, da \qquad (4.1.2)$$

where C is the contour of integration along the perimeter of the region and S is the

surface. We can take the region to be a distance w wide by l long and positioned

partially into the antenna as shown in Fig. 4.1 Since distance l is taken to be much

larger than the center wavelength of the emitted radiation, yet smaller than the

radiated beam diameter (i.e., the antenna gap spacing), the electric fields can be

assumed to be uniform over the respective sides of length l on the contour of

integration. Further, the electric fields point in a direction parallel to the plane of the

photoconductor (i.e., perpendicular to their respective directions of propagation).

Thus, Eq. (4.1.2) reduces to

$$E_{r,\text{in}}(t) - E_{r,\text{out}}(t) = -w \frac{\partial}{\partial t} \left(H_{r,\text{in}}(t) - H_{r,\text{out}}(t) \right) \qquad (4.1.3)$$

Since we assume that $\partial / \partial t \left(H_{r,\text{in}}(t) - H_{r,\text{out}}(t) \right)$ is bounded, we can express Eq.

(4.1.3) in the limit of the surface width w becoming very small. Thus, (3) reduces to

$$\lim_{w \to 0} \left(E_{r,\text{in}}\left(t\right) - E_{r,\text{out}}\left(t\right) \right) = 0 \qquad (4.1.4)$$

Thus, the radiated electric fields are predicted to be equal at the photoconductor surface,

$$E_{r,\text{in}}\left(t\right) = E_{r,\text{out}}\left(t\right) \qquad (4.1.5)$$

Also, Eq. (4.1.5) reduces to the steady-state boundary condition

$$n_z \times \left(E_{r,\text{in}}\left(t\right) - E_{r,\text{out}}\left(t\right) \right) = 0 \qquad (4.1.6)$$

Eq. (4.1.5) has been verified experimentally in a large-aperture antenna. This is in contrast to Hertzian dipole antennas where the radiated field directed into the antenna substrate has been calculated and measured to be stronger than that of one traveling through free space by a factor of ε. The boundary condition on the electric fields derived above cannot be used in the case of dipole antennas which have lengths much smaller than or comparable to the center wavelength of the emitted radiation and, thus, which produce highly divergent radiation. Because of these features of dipole antennas, the electric fields cannot be assumed to be uniform over respective analogous sides of the contour of integration and Eqs. (4.1.3)-(4.1.6) are not valid.

By a method like that used above, the boundary condition on the radiated magnetic field can be derived. This condition can be evaluated from the Ampere-Maxwell law

$$\nabla \times H = J + \frac{\partial D}{\partial t} \tag{4.1.7}$$

where D is the electric displacement (i.e., $D = \varepsilon E$). From Stokes's theorem,

$$\oint_C H \cdot dl = -\int_S \left(J + \frac{\partial D}{\partial t} \right) \cdot \mathrm{n}_x \, da \tag{4.1.8}$$

where the region of integration is the plane w wide by l long, mutually orthogonal to

the area of integration discussed previously and the surface of the photoconductor as

depicted in Fig. 4.1. As discussed above, this plane, with unit normal n_x, is also

positioned partially into the photoconductor. The surface current $J_s(t)$ is related to

the current density $J(z,t)$ by

$$J_s(t) = \int_0^\delta J(z,t) \, dz \tag{4.1.9}$$

where δ is the distance into the photoconductor that excited carriers exist and dz is

the increment of distance into the surface (i.e., along unit normal n_z). From Eqs.

(4.1.4), (4.1.8), and (4.1.7), Eq. (4.1.9) reduces to

$$H_{r,\mathrm{in}}(t) + H_{r,\mathrm{out}}(t) = J_s(t) - (1+\varepsilon) w \frac{\partial}{\partial t} E_{r,\mathrm{in}}(t) \tag{4.1.10}$$

Since it is taken that $(\partial / \partial t) E_{r,\mathrm{in}}(t)$ is bounded, the second term on the right-hand

side of Eq. (4.1.10) is negligible to the first term in the limit of w being small. Thus,

Eq. (4.1.10) becomes

$$\lim_{w \to 0} \left(H_{r,\mathrm{in}}(t) + H_{r,\mathrm{out}}(t) \right) = J_s(t) \tag{4.1.11}$$

Thus, Eq. (4.1.11) can be expressed as the steady-state boundary condition on the

magnetic field:

$$J_s(t) = \left(H_{r,\text{out}}(t) + H_{r,\text{in}}(t) \right) \times \text{n}_z \qquad (4.1.12)$$

The radiated magnetic fields are related to their corresponding radiated electric fields

by the free space resistance, η_0. Thus, the magnetic fields can be defined as

$$H_{r,\text{in}}(t) \times \text{n}_z = \frac{\sqrt{\varepsilon}}{\eta_0} E_{r,\text{in}}(t) \qquad (4.1.13)$$

$$H_{r,\text{out}}(t) \times \text{n}_z = -\frac{1}{\eta_0} E_{r,\text{out}}(t) \qquad (4.1.14)$$

From Eqs. (4.1.11) - (4.1.14), the surface current $J_s(t)$ can be represented as a

function of the inward radiated electric field $E_{r,\text{in}}(t)$,

$$J_r(t) = -\frac{(1+\sqrt{\varepsilon})}{\eta_0} E_{r,\text{in}}(t) \qquad (4.1.15)$$

The inward radiated field $E_{r,\text{in}}(t)$ can be expressed in terms of the bias field E_b

and the surface conductivity from the definition of the surface current $J_s(t)$. From

Ohm's law, the surface current is given by

$$J_s(t) = \sigma_s(t)\left(E_b + E_{r,\text{in}}(t) \right) \qquad (4.1.16)$$

where $\sigma_s(t)$ is the surface conductivity of the emitting antenna which is defined as:

$$\sigma_s(t) = \frac{q(1-R)}{h\nu} \int_{-\infty}^{t} \mu(t-t') I_{opt}(t') \, e^{-\frac{t-t'}{\tau_c}} \, dt' \qquad (4.1.17)$$

The meaning of Eq. (4.1.17) is the same as Eq. (3.1.1) in current surge model.

From Eq. (4.1.15) and (4.1.16), the inward radiated field $E_{r,\text{in}}(t)$ at the antenna can

be expressed as

$$E_{r,\text{in}}(t) = -\frac{\sigma_s(t)\eta_0}{\sigma_s(t)\eta_0 + (1+\sqrt{\varepsilon})} E_b \qquad (4.1.18)$$

61

The peak radiated electric field, $E_{r,\text{in,max}}(t)$, is given by

$$E_{r,\text{in,max}}(t) = -\frac{\sigma_{s,\text{max}}(t)\eta_0}{\sigma_{s,\text{max}}(t)\eta_0 + (1+\sqrt{\varepsilon})}E_b \qquad (4.1.19)$$

where $\sigma_{s,\text{max}}(t)$ is the peak surface photoconductivity which is expressed as

$$\sigma_{s,\text{max}}(t) = -\frac{q(1-R)\mu_{tr}F}{h\nu} \qquad (4.1.18)$$

where μ_{tr} is the transient carrier mobility at the point in time when the surface conductivity is maximum, F is the optical pump fluence.

4.2   Experimental methods

Our basic experimental setup was a conventional THz-TDS system as shown in Fig. 4.2 [16]. In detail, we used a mode-locked regeneratively amplified Ti:sapphire laser (λ= 800 nm) with 0.8 W average output power to generate pulses with duration τ_p of 50 fs at a 1-kHz repetition rate. The output laser beam was divided into a pump and a probe beam. The pump beam passed through a variable attenuator and was chopped at 200 Hz by a mechanical chopper. The probe power was fixed to ~ 30 mW. To overlap the whole antenna gap, the beam was first expanded by a concave lens with focal length of 5 cm, and then illuminates the gap at normal incidence. The THz radiation was generated by the laser excited, DC voltage applied large-aperture photoconductive antenna fabricated on SI-GaAs and Arsenic-ion-implanted GaAs (GaAs:As$^+$). The antenna is the AuGe/Ni/Au coated two strip line antenna with gap

spacing of 1.5 cm. The ion implanted energy of GaAs:As$^+$ is 200 keV with post

furnace annealing of $600\,^\circ\mathrm{C}$ for 30 min. The THz radiation was then emitted

through the substrate, collimated by a pair of off-axis parabolic mirrors and focused

onto a <110>-cut ZnTe crystal with 1-mm thickness. The other coherent probe laser

was also transmitted through the crystal and resolved the THz field by a quarter wave

plate, Wollaston prism, and balanced photo-detectors. The THz waveform was

mapped out by moving the delay line between the pump pulse and the probe pulse.

The carrier lifetimes τ_c for both types of antennas were obtained from the optical

pump-probe differential reflection measurement. In the pump fluence dependence

experiment, pump fluence F was varied through a calibrated attenuator in front of the

emitters.
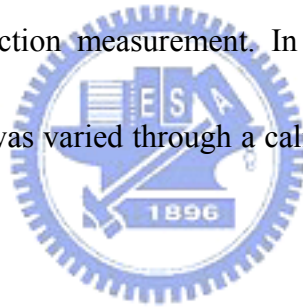
4.3 Theoretical methodology

In order to dedicate an explanation to the mechanisms underlying THz pulse

waveforms from large-aperture antennas, we adopt a methodology based on wave

propagation scheme. If a pump pulse with field strength ξ propagates through a

nonlinear dispersive medium (e.g. THz antenna) along z direction, it will undergo

several nonlinear effects, such as: pulse dispersion β'', two-photon absorption α'',

and optical-Kerr effect γ. The spatial z and time t dependent behavior associated

with these phenomena is governed by the following nonlinear envelope equation for

ξ [17]:

$$\left(\frac{\partial}{\partial z} + \frac{n_L}{c_0} \frac{\partial}{\partial t} \right) \xi = -\alpha(N_e)\xi - \alpha'' \left| \xi \right|^2 \xi + i \frac{\beta''}{2} \frac{\partial^2 \xi}{\partial t^2} + i\gamma \left| \xi \right|^2 \xi, \tag{4.3.1}$$

where

$$\alpha(N_e) = \alpha_0 \left(\frac{N_{max} - N_e}{N_{max}} \right) \tag{4.3.2}$$

is the single photon absorption caused by the band filling effect [18], α_0 is the linear

absorption coefficient, N_{max} is the population inversion threshold, N_e is the

single-photo-excited electron concentration, while the constant n_L, c, and symbol i

stand for linear refractive index, light vacuum speed, and imaginary unit, respectively.

In Eq. (4.3.2), the evolutions of the N_e and single-photon-excited hole

concentration N_h obey the current-continuity equations:

$$\frac{\partial N_e}{\partial t} = \alpha(N_e) \frac{\left| \xi \right|^2}{2\eta h\nu \sqrt{\pi}} - \frac{N_e(x, z, t)}{\tau_c} \tag{4.3.3}$$

$$\frac{\partial N_h}{\partial t} = \alpha(N_e) \frac{\left| \xi \right|^2}{2\eta h\nu \sqrt{\pi}} - \frac{N_h(x, z, t)}{\tau_c}, \tag{4.3.4}$$

where η denotes the medium impedance, and $h\nu$ is the photon energy. The

generated carriers are subjected to E_b, and cause a conducting current J given by:

$$J = J_e + J_h = q\{\mu_e N_e(x, z, t) + \mu_h N_h(x, z, t)\}E_b \tag{4.3.5}$$

Here the quantity μ_e and μ_h denote the carrier mobilities for electron and hole, and

q stands for the electron charge. Inside the medium, the current J induces an

electromagnetic field E satisfying the second-order scalar wave equation:

$$\nabla^2 E - \mu\varepsilon\frac{\partial^2 E}{\partial t^2} = \mu\frac{\partial J}{\partial t}. \qquad (4.3.6)$$

In far-field regime, evaluating the broadband Huygen-Fresnel diffraction integral [19] of E yields the far-field radiation field $E_r(t)$ as:

$$E_r(t) = \int\frac{\cos(\hat{z}, d')}{2\pi d' c_0}\frac{d}{dt}\left\{E(x', t - \frac{d}{c_0})\right\}ds. \qquad (4.3.7)$$

In this notation, $\hat{z}$ represents the unit vector in z direction, the distance vector is denoted as d, and s refers to the differential area of the antenna's surface. The peak THz amplitude $E_r^{\max}$ can be obtained by evaluating the maximum of E_r.

In solving Eqs. (4.3.1) and (4.3.6), a reflection boundary conditions are applied to ξ and E on the incident surface, while an absorbing boundary conditions are assumed on the outer surface. For ξ, we assume a Gaussian function with duration of τ_p:

$$\xi(z, t = 0) = \sqrt{\frac{2\eta F}{\tau_p}}exp[-\frac{1}{2}\left(\frac{zn_L}{c_0\tau_p}\right)^2] \qquad (4.3.8)$$

as an initial condition of Eq. (4.3.1). The values for the parameters included in Eqs. (4.3.1)-(4.3.8) are summarized in Table I. To match the measured data, we select a lower $N_{\max}$ and higher α'' value than that reported in Ref. [28]. In the appendix A, we demonstrate some programming routines for solving Eqs. (4.3.1)-(4.3.8) using Mathematica v 6.0.

In the case of small-aperture antennas, the velocity overshoot, space-charge field screening, or photo-Dember effects contribute to the formation of bipolar THz waveforms with bandwidth more than 1 THz, depending on F, E_b, and the incident

condition of pump pulse. In our case, however, the measured waveforms reveal

unipolar THz pulses with narrower bandwidth (~ 0.5 THz) rather than bipolar THz

pulses with broader bandwidth at various F and normal incidence. This fact allows us

to neglect the aforementioned three effects in our simulation for large-aperture

antennas.

Although the $E_r^{\max}$ can be obtained from Eq. (4.3.7) by evaluating the maximum of

$E_r(t)$, as a comparison, we also present the $E_r^{\max}$ given by the scaling rule:

$$E_r^{\max} \approx D \frac{F / F_s}{1 + F / F_s},\tag{4.3.9}$$

where

$$D = \frac{A n_L^{1/2} E_b}{4\pi\varepsilon_0 c^2 \eta_0 \tau_d z},\tag{4.3.10}$$

and

$$F_s = \frac{(1 + n_L)h\nu}{q(1 - R)\mu_e \eta_0}.\tag{4.3.11}$$

4.4   Results and discussions

4.4.1   Pump fluence dependence

4.4.1.1   Waveforms and spectra

In Fig. 4.3 we show the normalized photoreflectance changes $\Delta R / R$ with

respect to the time delay t using SI-GaAs and GaAs:As$^+$ antennas. Fitting the data of

Fig. 4.3 to exponential decays, yields the τ_c of 2.5 ps for the SI-GaAs antenna and

0.8 ps for the GaAs:As$^+$ antenna. Obviously, these τ_c values are much larger than the pump pulse duration τ_p (= 0.05 ps). Here the values of τ_c are used to substitute into the calculation of Eq. (4.3.7) and (4.3.8).

In Figs. 4.4(a) and 4.4(b), we present the measured THz radiation waveforms E_r from SI-GaAs and GaAs:As$^+$ antennas with E_b of 0.6 kV/cm under various pump fluences F. As can be seen, each waveform consists of a dominated peak followed by a relatively small and long negative tail. These waveforms can be characterized by four quantities: peak width dt (FWHM), peak shift t_p, peak amplitude E_r^{max}, and minimum amplitude E_r^{min}. The normalized Fourier-transformed amplitude spectra $\tilde{E}_r$ of Fig. 4.4(a) and 4.4(b) are shown in Fig. 4.3(c) and Fig. 4.4(d). Owing to the unipolar shapes in waveforms, the spectra contain small residual dc components which also can be seen from Ref. 4.5. For these spectra, we pay attention to their peak frequency f_p and frequency bandwidth df.

For the sake of comparison, we select one waveform individually from Figs. 4.4(a) and 4.4(b) at the same F, and plot these two waveforms with normalization in Fig. 4.5(a). From Fig. 4.5(a) it was obtained that E_r^{min} = 0.15 and dt = 0.72 ps for the case of the SI-GaAs antenna, and E_r^{min} = 0.08, dt = 0.70 ps for the case of the GaAs:As$^+$ antenna. The quantity dt is comparable to those observed in some centimeter-size antennas. The Fourier-transformed amplitude spectra $\tilde{E}_r$ of Fig.
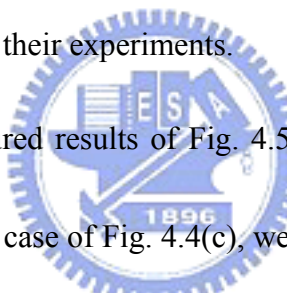
4.5(a) are plotted in Fig. 4.5(b). It was found that the quantity f_p for both types of

antennas is equal to 0.13 THz, and the df (= 0.57 THz) of GaAs:As$^+$ is larger than in

the case of SI-GaAs (df = 0.52 THz).

With our aim being to explain the measured results of Fig. 4.4(a) and 4.4(b),

we calculated Eq. (4.3.1)-(4.3.8) by assuming that both α_0 and n_L of the GaAs:As$^+$

antenna are larger than that of the SI-GaAs antenna as seen in Table 1. Figures 4.4(c)

and 4.4(d) plot the simulated E_r and $\tilde{E}_r$ corresponding to Fig. 4.4(a) and 4.4(b).

From Fig. 4.4(c), it was found that the simulated dt for SI-GaAs and GaAs:As$^+$ are

0.32 ps and 0.30 ps, respectively. Also, the simulated E_r^{min} is about 0.15, which is

close to the measured one. In numerically studying the influence of the τ_c on E_r^{min},

we found that E_r^{min} is relevant to the values of the τ_c. The shorter the τ_c, the larger

the E_r^{min}. Besides, the irregular negative waveforms stem from the pulse dispersion

and optical-Kerr mechanism. In Fig. 4.4(d), the df of GaAs:As$^+$ reveals a larger value

(df = 1.5 THz) than that (df = 1.2 THz) of SI-GaAs. This larger df of GaAs:As$^+$

merely reflects its shorter dt compared to the SI-GaAs case.

4.4.1.2. Peak width, peak shift, and bandwidth

Figure 4.5(a) plots the measured dt and t_p obtained from Fig. 4.3(a) and 4.3(b) as a

function of F. It is remarkable that as F increases from 2 to 58 μJ/cm^2, the quantity dt

of SI-GaAs decreases monotonically to its minimal value located at the turning point

($F = 30\,\mu\mathrm{J/cm}^2$, d$t$ = 0.72 ps), and subsequently increases from that point onward. In

the case of GaAs:As$^+$, dt varies with F in a manner similar to the case of SI-GaAs, but

its turning point occurs at higher F (= $44\,\mu\mathrm{J/cm}^2$) than in the case of SI-GaAs. For

both types of antennas, the quantity t_p reveals an increasing trend with the increase of

F. Also, the dt or t_p value for GaAs:As$^+$ is less than that for SI-GaAs at each value of

F. Although the measured dt values in Fig. 4.5(a) are close to those obtained by T.

Hattori et al. (cf. Ref. [5]), it is worth noting that the phenomenon relevant to the

turning point was not found in their experiments.

To interpret the measured results of Fig. 4.5(a), with the assumption of α_0

and n_L being the same as the case of Fig. 4.4(c), we calculated Eqs. (4.3.1)-(4.3.8) at

different F, and present the results in Fig. 4.5(b). As seen in this figure, the simulated

data produced a monotonic decrease in dt and an increase in t_p with increasing F. In

addition, the simulated dt or t_p for GaAs:As$^+$ is less than that for SI-GaAs, mainly due

to a larger α_0 and n_L in GaAs:As$^+$. However, it was found that the turning point

behavior does not appear in the simulated dt.

From the spectra in Figs. 4.3(c) and 4.3(d), we plotted the measured df and f_p

in Fig. 4.5(c) as the function of F. Obviously, one can see from Fig. 4.5(c) that the

df of GaAs:As$^+$ is larger than that of SI-GaAs under various F. This larger df for

GaAs:As$^+$ reflects the shorter dt shown in Fig. 4.5(a). In addition, it can be perceived

that the f_p as well as the difference between two df, has an increasing trend with the

increase of F.

4.4.1.3. Peak THz amplitude

In Fig. 4.6(a) we show the measured E_r^{max} of SI-GaAs and GaAs:As$^+$ antennas as a

function of pump fluence from $F = 2$ up to $170\,\mu\mathrm{J/cm}^2$. We observe that as F

increases from 2 to $58\,\mu\mathrm{J/cm}^2$, both E_r^{max} curves increase monotonically. Compared

with the SI-GaAs case, the E_r^{max} values of the GaAs:As$^+$ antenna are lower, provided

that $F < 20\,\mu\mathrm{J/cm}^2$, but exceed that of the SI-GaAs antenna, provided that $F >$

$20\,\mu\mathrm{J/cm}^2$; hence both curves intersect at $F = 20\,\mu\mathrm{J/cm}^2$. In addition, note that both

curves reach their respective maximums in the vicinity of $F = 60\,\mu\mathrm{J/cm}^2$, then

gradually become reduced instead of further increasing as F increases from 60 to

$170\,\mu\mathrm{J/cm}^2$. We designate this phenomenon as anomalous saturation since the

quantity in normal saturation tends to increase slowly with the increasing of F rather

than reducing to a lower value. From these two anomalous saturation data, it is

instructive to gain insight into how the difference in E_r^{max} between two types of

antennas varies with F. To quantify this difference, we introduce a relative emission

efficiency ρ defined as the ratio of the difference in peak THz amplitude between

two types of antennas to peak THz amplitude of the SI-GaAs antenna, that is, $\rho \equiv$

$[E_r^{max}(\text{GaAs:As}^+) - E_r^{max}(\text{SI-GaAs})]/E_r^{max}(\text{SI-GaAs})$. Figure 4.6(a) also shows the F

dependence of the relative emission efficiency ρ in percentage term (%). In

particular, it appears that the quantity ρ first grows from $F = 2\,\mu\text{J/cm}^2$, until it

reaches to a maximum (~12%) at $F = 30\,\mu\text{J/cm}^2$ and finally reduces, tending to lower

values for high enough F.

In contrast to our previous study (see Ref. [19]), where we compared the

emission efficiency of SI-GaAs and multi-GaAs:As$^+$ antennas with gap size of

$5\,\mu\text{m}$, our large-aperture GaAs:As$^+$ antenna takes advantage of better THz emission

efficiency than our SI-GaAs one, above specific F. In Ref. [16], one can see that a

similar advantage also happens to the dipole-I LT-GaAs small-aperture antenna,

which exhibits better emission efficiency relative to the case of SI-GaAs, above pump

power of 21 mW. Nevertheless, its advantage has not been confirmed theoretically.

On the other hand, although the anomalous saturation does not occur at our previous

GaAs:As$^+$ small-aperture antenna, it was observed by Tani *et al.* in dipole-I SI-GaAs

small-aperture antenna (see Ref. [16]), and also by Löffler *et. al.* and Hasegawa in

large-aperture SI-GaAs antenna. In Ref. 4.33, the anomalous saturation was attributed

to initial carrier effect.

In an attempt to theoretically reproduce the relation between the measured

E_r^{max} and F, we fit our measured E_r^{max} using the scaling rule given by Eq. (4.3.9), and

report the fitting results in Fig. 4.6(b). From these two fitting curves, it was obtained

that $D = 331.5$, $F_s = 5.3\,\mu J/cm^2$ for SI-GaAs, and $D = 377.6$, $F_s = 9.7\,\mu J/cm^2$ for

GaAs:As$^+$. Accordingly, either the F_s or D values in the GaAs:As$^+$ case are larger than

those in the SI-GaAs case. Note that F_s depends on both the μ_e and n_L according

to Eq. (4.3.11). Under the same pump wavelength, a larger F_s for GaAs:As$^+$ implies

two consequences: one is that its μ_e value is lower than that of SI-GaAs since F_s is

inversely proportional to μ_e; the other is that its n_L is larger than that of SI-GaAs

since F_s is proportional to n_L. Both consequences are reasonable since

ion-implantation reduces the μ_e value, whereas increasing the α_0 value leads to the

increase of n_L due to the reciprocal relationship between α_0 and n_L. Under the

same pump and detection configuration, a larger D for GaAs:As$^+$ indicates that the

quantity $n_L^{1/2}$ of GaAs:As$^+$ is also larger than that of SI-GaAs according to Eq.

(4.3.10). Therefore, an increase in n_L leads to a higher D for GaAs:As$^+$ compared to

SI-GaAs. In contrast to the measured E_r^{max} in Fig. 4.6(a), although the fitting curves in

Fig. 4.6(b) are able to account for the E_r^{max} behavior at low F, it is still not consistent

with the measured E_r^{max} at high F regime. To resolve this discrepancy, we considered

the band-filling and two photon absorption effects as described in Section III instead

of initial carrier effect presented in Ref. 4.33. From the implication of the fitting

curves given by the scaling rule, we evaluated Eqs. (4.3.1)-(4.3.8) provided that the

n_L for GaAs:As$^+$ is 1.06 times larger than that for SI-GaAs, and also plotted the two

simulated E_r^{max} along with the ρ in Fig. 4.6(b). As shown in the graph, each

simulated E_r^{max} initially increases at increasing values of F, reaches a maximum at

about $F = 80\,\mu J/cm^2$, and then starts decreasing gradually at large values of F.

Similarly to the measured case, the E_r^{max} value of GaAs:As$^+$ is lower than that of

SI-GaAs below $F = 20\,\mu J/cm^2$, but higher than $F = 20\,\mu J/cm^2$. Besides, the maximum

of the simulated ρ (~16%) appears at about $F = 55\,\mu J/cm^2$.

Referring to the simulated dependency in Fig. 4.6(b), the trends in E_r^{max} and

anomalous saturation behavior are both consistent with our experimental observation

of Fig. 4.6(a). Accordingly, we infer that the GaAs:As$^+$ antenna possesses a larger

refractive index n_L and smaller μ_e so that the E_r^{max} value for GaAs:As$^+$ is lower

than that for SI-GaAs, below $F = 20\,\mu J/cm^2$, but higher than $F = 20\,\mu J/cm^2$. In

another respect, in the region of pump fluence more than $60\,\mu J/cm^2$, the effects of

band filling and two-photon absorption become obvious and confine the values of

E_r^{max}.

4.4.2 Bias dependence

We next examine the dependence of E_r^{max} on E_b at specific F where the emission efficiency of GaAs:As$^+$ is higher than that of SI-GaAs. Figure 4.7 contains our results for the measured E_r^{max} of SI-GaAs and GaAs:As$^+$ antennas as a function of E_b at $F = 58\,\mu$J/cm^2. It clearly appears that the experimental data apparently fit the linear relationships from $E_b = 0.5$ to 0.85 kV/cm for both types of antennas. Besides, the zero-intercept line for GaAs:As$^+$ has a larger slope than that for SI-GaAs, implying that GaAs:As$^+$ has a considerably higher E_r^{max} than does SI-GaAs at any same E_b value. These two linear trends are analogous to those found in other large-aperture antennas (see Refs. 4.14 and 4.15). As expected on the basis of the scaling rule, the origin of these linear dependences can be interpreted straightforwardly by the linear relation between E_r^{max} and E_b in accordance with Eqs. (4.3.9) and (4.3.10). In THz antenna literature, we do not find any exception deviating from this linear relation.

Also shown in Fig. 4.7 is the relative emission efficiency ρ. Remarkably, ρ first grows until it reaches its maximum ($\sim 40\%$) in the vicinity of 0.57 kV/cm, then subsequently reduces to 30%, and does not decrease any more at high E_b regime. To the best of our knowledge, this special characteristic has not been discovered by any group except ours. Its importance lies in the fact that if the two zero-intercept lines in Fig. 4.7 were exactly linear, the values in ρ would supposedly form a horizontal line rather than a curve. Accordingly, we infer that the relationships between E_r^{max} and

E_b are not exactly linear for our or even other group's cases. In other words, the scaling rule expressed by Eq. (4.3.9) is not a rigorous model, and the mechanism responsible for the maximum of ρ at low E_b regime is due to a nonlinear relationship between $E_r^{\max}$ and E_b. Nevertheless, its exact theoretical relationship remains unknown to us.

4.5   Conclusions

We have performed a comparative study between THz radiation waveforms for large-aperture biased SI-GaAs and GaAs:As$^+$ antennas under various pump fluences and bias field. The THz pulses emitted from our GaAs:As$^+$ antenna have narrower peak width, wider bandwidth, and higher peak THz amplitude than those obtained from the SI-GaAs antenna. The peak frequency and bandwidth difference between these two types of antennas have increasing trends with increasing pump fluence. From the pump fluence dependence of peak THz amplitude, we have found that SI-GaAs and GaAs:As$^+$ antennas both exhibit anomalous saturation behaviors which can be reproduced numerically by incorporating nonlinear effects into a rigorous electromagnetic wave propagation model. Above pump fluence of $20\,\mu\text{J/cm}^2$, the GaAs:As$^+$ antenna obtained better emission efficiency relative to the SI-GaAs antenna. On the basis of numerical simulation, we have deduced that this better

emission efficiency stems from the fact that both types of antennas have different quantities, including: linear absorption coefficient, refractive index, and carrier mobility. For the GaAs:As$^+$ antenna, the first two quantities are larger, whereas the last is smaller in comparison with the SI-GaAs antenna. We have also inferred from our simulation that the band filling and two-photon absorption effects are responsible for the anomalous saturation behavior. In the bias field dependence of measured peak THz amplitude, we have found that the emission efficiency of the GaAs:As$^+$ antenna is higher than that of the SI-GaAs antenna, and that the relative emission efficiency reaches maximum at specific bias field. This particular behavior convinces us that a more rigorous model is required for interpreting the bias field dependence of peak THz amplitude instead of the scaling rule, and we believe that it will be an important topic worthy of being investigated further.

References

[1] T. Hattori, K. Tukamoto, and H. Nakatsuka, Jap. J. App. Phys. 40, 4907 (2001).

[2] S. R.Andrews, A. Armitage, P. G. Huggard,and A. Hussain, Phys. Med. Biol. 47, 3705 (2002).

[3] G. Zhao, R. N. Schouten, N. van der Valk, W. T. Wenckebach, and P. C. M. Planken, Rev. Sci. Instrum.73, 1715 (2002).

[4] A. Dreyhaupt, S. Winnerl, T. Dekorsy, and M. Helm, App. Phys. Lett. 86, 121114 (2005).

[5] David A Turton, Gregor H Welsh, John J Carey, Gavin D Reid, Godfrey S Beddard, and Klaas Wynne, Rev. Sci. Instrum. 77, 083111 (2006).

[6] S. Winnerl,   A. Dreyhaupt,   F. Peter,   D. Stehr,   M. Helm,   and   T. Dekorsy, *Nonequilibrium Carrier Dynamics in Semiconductors* (Springer Berlin Heidelberg), 110, 73 (2006).

[7] B. B. Hu and M. C. Nuss, Opt. Lett. 20, 1716 (1995).

[8] Tze-An Liu, Gong-Ru Lin, Yung-Cheng Chang, and Ci-Ling Pan, Opt. Exp. 13, 10416 (2005).

[9] S. Ramsey, E. Funk, and C. H. Lee, in The Int. Topical Meeting on Microwave Photonics '99, Technical Digest, 265 (1999).

[10] R. R. Jones, D. You, and P. H. Bucksbaum, Phys. Rev. Lett. 70, 1236 (1993).

[11] X. Zhang and R. R. Jones, Phys. Rev. A 73, 035401 (2006).

[12] D.J. Cook, J.X. Chen, E.A. Morlino, R.M. Hochstrasser, Chem. Phys. Lett. 221 (1999).

[13] P. K. Benicewicz and A. J. Taylor, Opt. Lett. 18, 1332 (1993).

[14] T.-An. Liu, M. Tani, C.-L. Pan, J. Appl. Phys. 93, 2996 (2003).

[15] J. T. Darrow, Xi,-C. Zhang, D. H. Auston, and J. D. Morse, IEEE J. Quantum Electron. 28, 1607 (1992).

[16] Q. Chen and X.-C. Zhang, Appl. Phys. Lett. 74, 3435 (1999).

[17] Bahaa E. A. Saleh and Malvin Carl Teich, *Fundamentals of Photonics* (John Wiley & Son, 1991), Chap.19.

[18] F. Kadlec and H. Nemec, P. Kuzel, Phys. Rev. B 70, 125205 (2004).

[19] J. W. Goodman, *Introduction to Fourier Optics* (McGraw-Hill Publishing Company, 1996).

[20] M. Tani, K. Sakai, H. Abe, S. Nakashima, H. Harima, M. Hangyo, Y. Tokuda, K. Kanamoto, Y. Abe, and N. Tsukada, Jpn. J. Appl. Phys. 33, 4807 (1994).

[21] S. Gupta, J. F. Whitaker, and G. A. Mourou, IEEE J. Quantum Electron. 28, 2464 (1992).

[22] Wang, H.-H. Grenier, P. Whitaker, J. F. Fujioka, H. Jasinski, J. Liliental-Weber, Z., IEEE J. Selected Topics in Quantum Electron. 2, 630 (1996).

[23] D. D. Nolte, W. Walukiewicz, and E. E. Haller, Phys. Rev. Lett. 59, 501 (1987).

[24] G.-R, Lin, C,-C, Hsu, J. Appl. Phys. 89, 1063 (2001).

[25] A. J. Taylor, P. K. Benicewicz, and S. M. Young, Opt. Lett. 18, 1340 (1993).

[26] G. Rodriguez, S. R. Caceres, and A. J. Taylor, Opt. Lett. 19, 1994 (1994).

[27] Q. Chen and X.-C. Zhang, Appl. Phys. Lett. 74, 3435 (1999).

[28] Bahaa E. A. Saleh and Malvin Carl Teich, *Fundamentals of Photonics* (John Wiley & Son, 1991), Chap.19.

[29] F. Kadlec and H. Nemec, P. Kuzel, Phys. Rev. B 70, 125205 (2004).

[30] J. W. Goodman, *Introduction to Fourier Optics* (McGraw-Hill Publishing Company, 1996).

[31] T. Dekorsy, H. Auer, H. J. Bakker, H. G. Roskos, and H. Kurz, Phys. Rev. B 53, 4005 (1996).

[32] T. Löffler, T. Hahn, M. Thomson, F. Jacob, and H. G. Roskos, Opt. Exp. 13, 5353 (2005).

[33] N. Hasegawa, Dissertation, University of Frankfurt (2004), http://deposit.ddb.de/cgi-bin/dokserv?idn=975373056.

Table 4.1: Parameters used in THz radiation simulations for SI-GaAs and GaAs:As[+]

antennas

	α_0 (cm^{-1})	N_{max} (cm^{-3})	α'' (cm/GW)	n_L	μ_e , μ_h (cm^{2}V^{-1}s^{-1})	β'' (ps^{2}km^{-1})	γ (cm/GW)
SI-GaAs	6.5×10^3	2.0×10^{18}	286	3.4	1000, 50	120	3.2
GaAs:As$^+$	6.7×10^3	2.0×10^{18}	286	3.6	800, 20	120	3.2
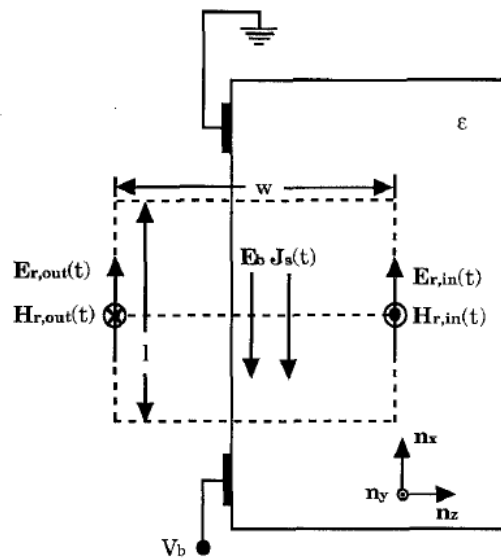
Fig. 4.1: Schematic of a large-aperture photoconductive antenna with a voltage V_b.*

* J. T. Darrow, Xi,-C. Zhang, D. H. Auston, and J. D. Morse, IEEE J. Quantum Electron. **28**, 1607
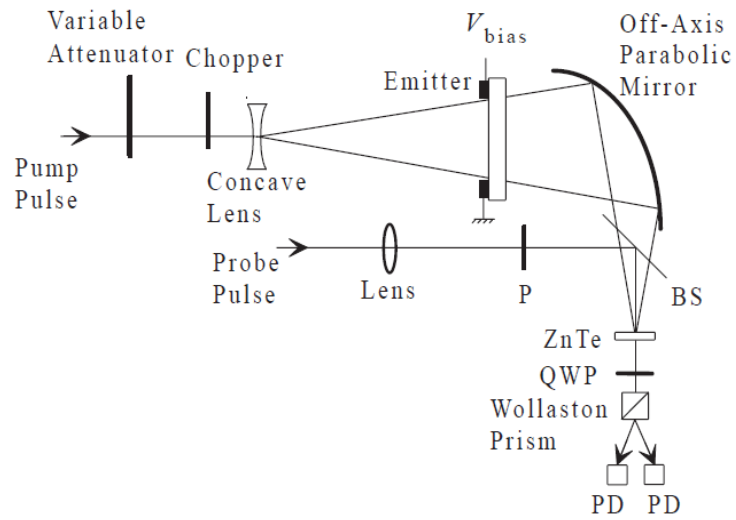
(1992).

Fig. 4.2: Experimental setup for a large-aperture photoconductive antenna with a

voltage V_b.*

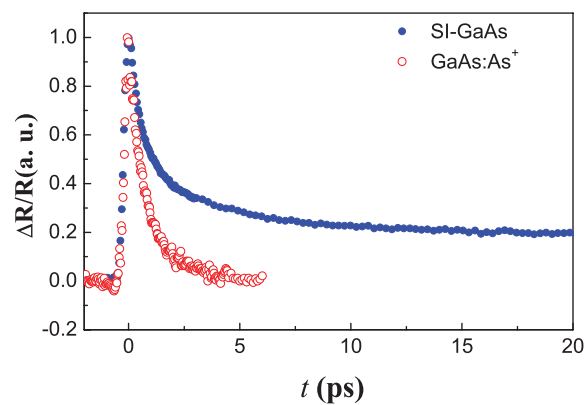*T. Hattori, K. Tukamoto, and H. Nakatsuka, Jap. J. App. Phys. 40, 4907 (2001).

Fig. 4.3: Transient normalized photoreflectance changes for SI-GaAs (solid blue
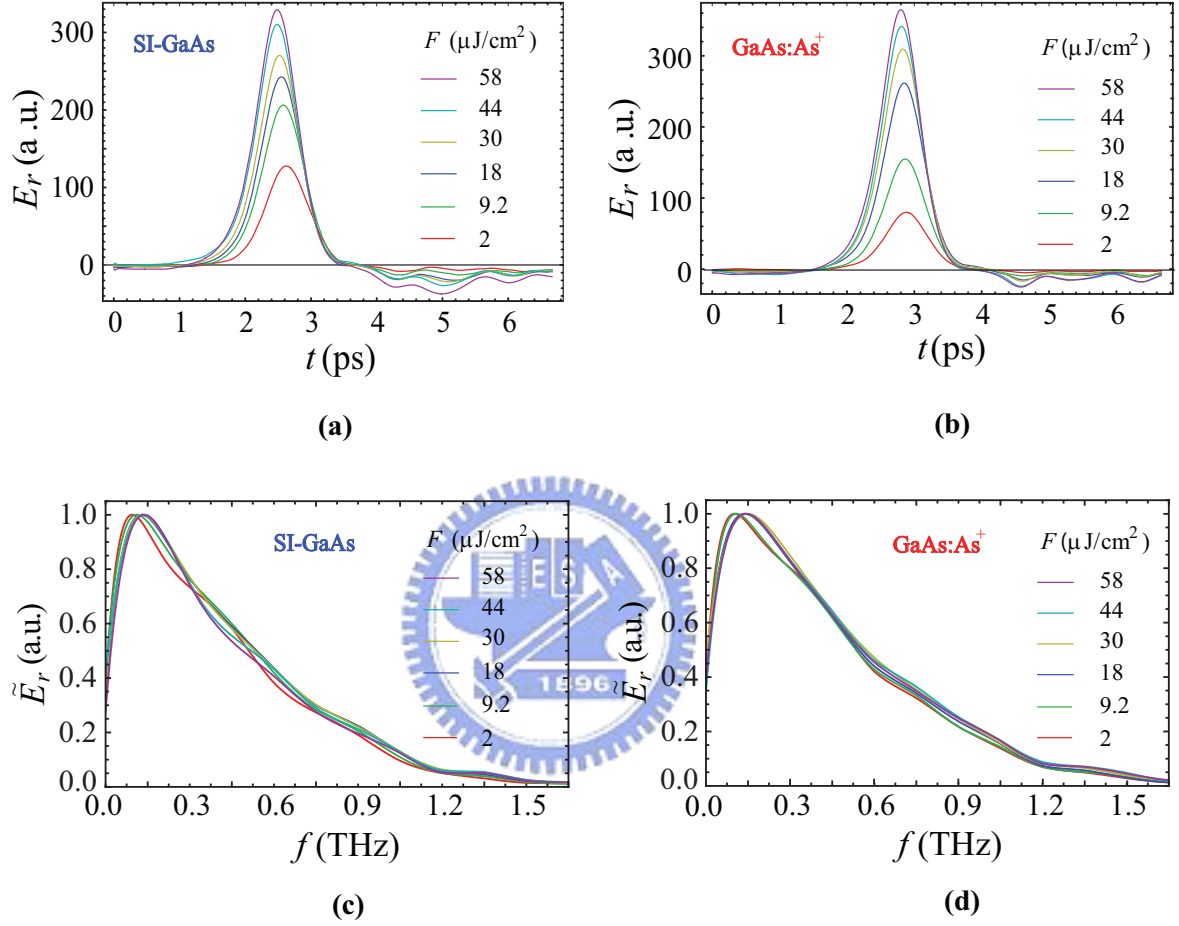
circle) and GaAs:As$^+$ (open red circle) antennas.

Fig. 4.4: Measured THz waveforms E_r for (a) SI-GaAs, and (b) GaAs:As$^+$ antennas as a function of time delay t at various pump fluences F. The bias field applied to the antennas was kept at 0.6 kV/cm. (c) Fourier-transformed amplitude spectrum $\widetilde{E}_r$ of the waveforms in (a), and (d) $\widetilde{E}_r$ of the waveforms in (b).
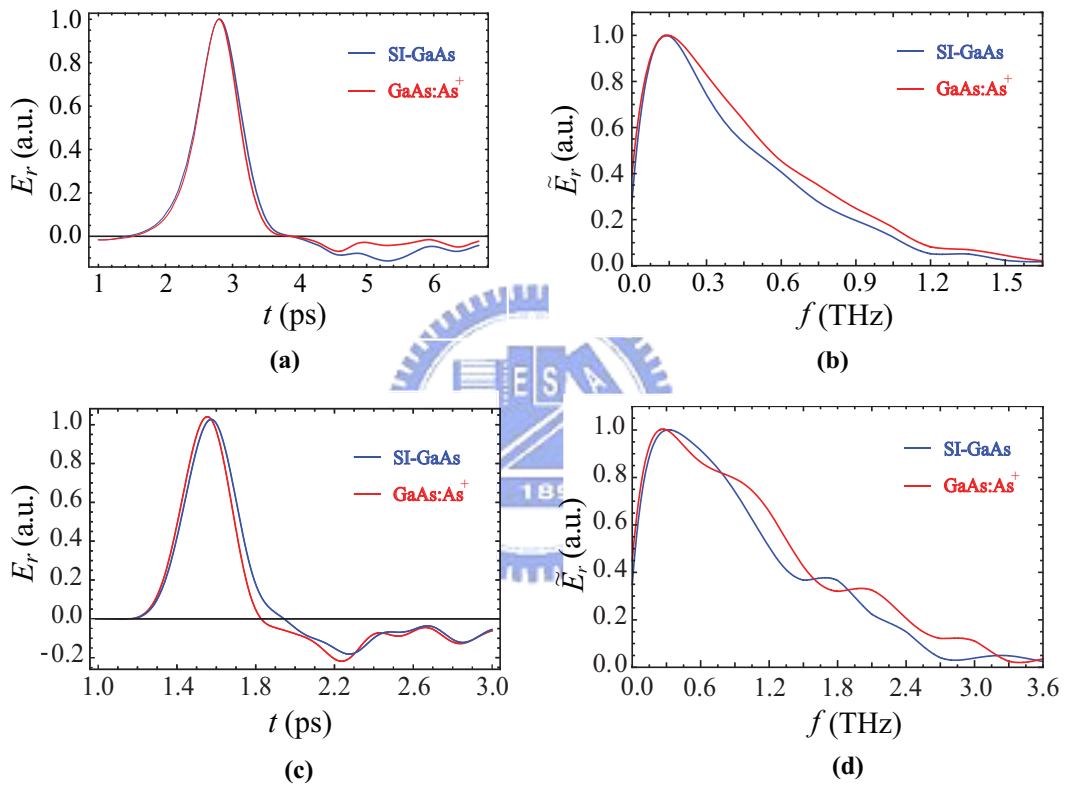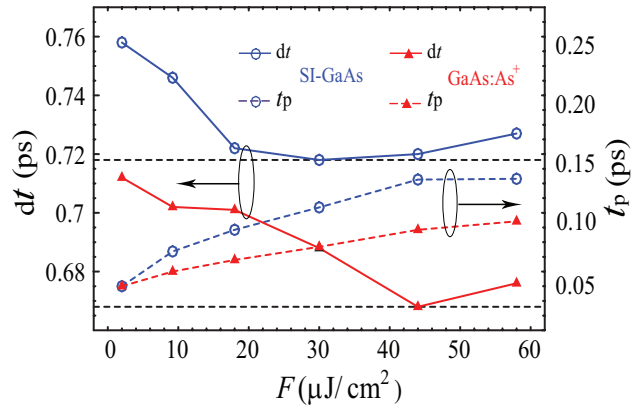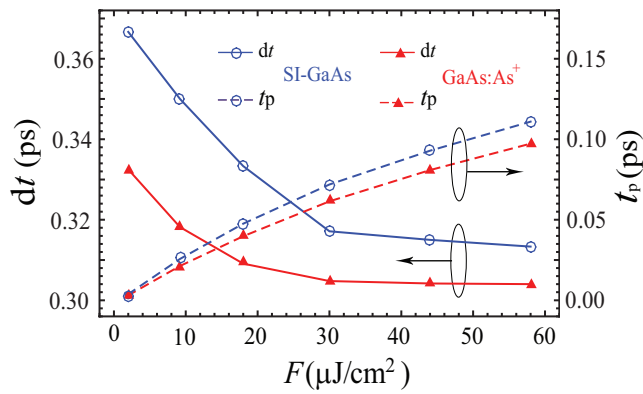
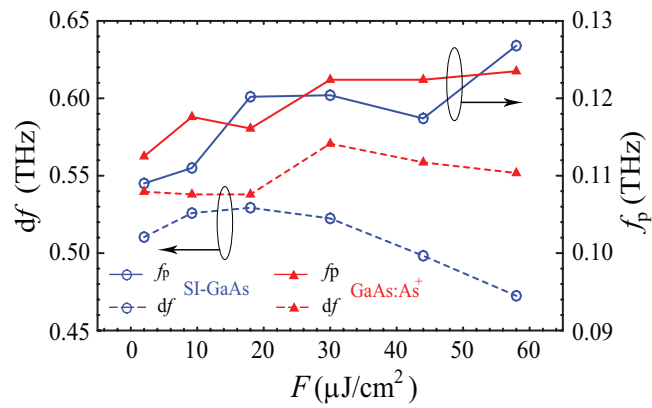**Fig. 4.5**: (a) Measured THz waveforms E_r, (b) corresponding Fourier-transformed amplitude spectrum $\widetilde{E}_r$, (c) simulated E_r and (d) $\widetilde{E}_r$ for SI-GaAs (blue full line) and GaAs:As$^+$ (red full line) antennas at pump fluence $F = 58\,\mu\text{J}/\text{cm}^2$. Both E_r and $\widetilde{E}_r$ are normalized to their peak amplitude.

(a)

(b)

(c)

85

Fig. 4.6: (a) Measured peak width d*t* (full line) and peak shift t_{p} (dashed line) obtained

from Fig. 2(a) and 2(b), (b) simulated d*t* (full line) and t_{p} (dashed line), and

(c) measured peak frequency f_{p} (full line) and bandwidth d*f* (dashed line)

obtained from Fig. 2 (c) and 2(d) as a function of pump fluence F for both

SI-GaAs (blue) and GaAs:As$^+$ (red) antennas.
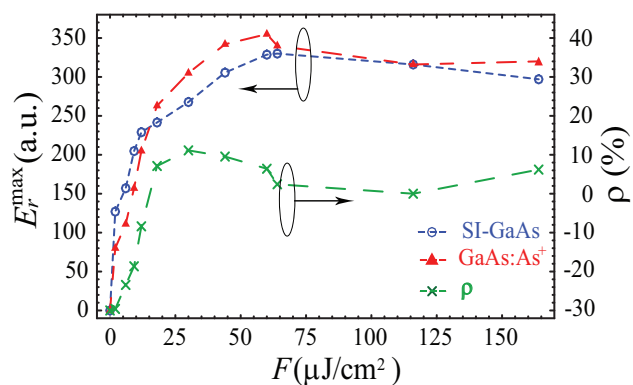
(a)
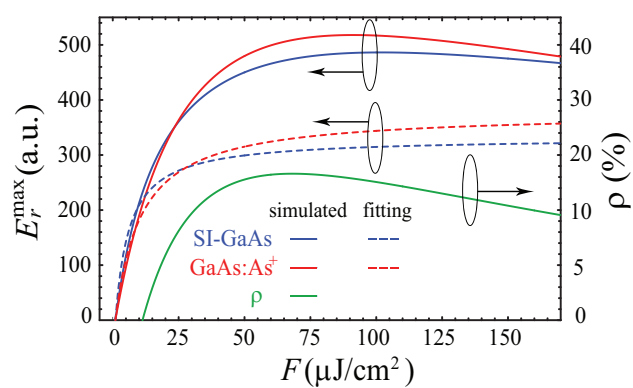
(b)

Fig. 4.7: (a) Measured (dashed-marks), (b) fitting (dashed line), and simulated (full

line) THz peak amplitude E_r^{max} versus pump fluence F for both SI-GaAs

(blue) and GaAs:As$^+$ (red) antennas. The green dash-cross and full lines are

the ratio ρ ($\equiv (E_r^{max}(\text{GaAs:As}^+) - E_r^{max}(\text{SI-GaAs}))/E_r^{max}(\text{SI-GaAs}))$ for

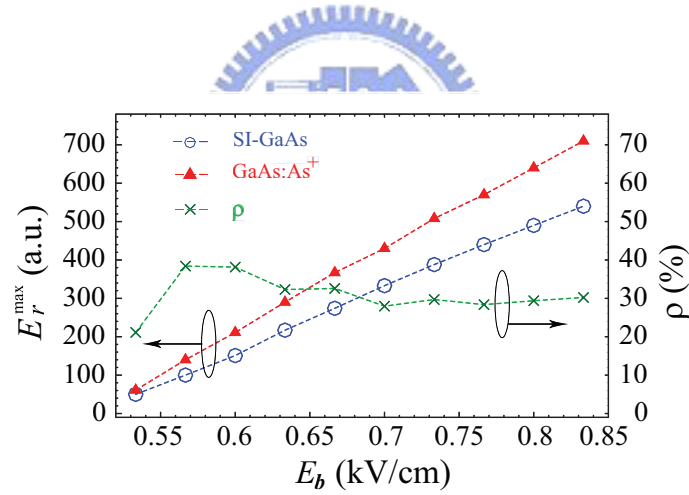measured and simulated case. The bias field E_b was kept at 0.6 kV/cm.

Fig. 4.8: Measured peak THz amplitude E_r^{max} from SI-GaAs (blue dashed-circle) and

GaAs:As$^+$ (red dashed-triangle) antennas, and the relative emission

efficiency ρ (green dashed-cross) as a function of bias field E_b at pump

fluence $F = 58\,\mu\text{J}/\text{cm}^2$.

Chapter 5

Mid-size-gap antennas

For the sake of generating giant THz radiation fields of up to a hundred kilovolts per centimeter, the gap size (G) of a biased PC antenna ought to be larger than 1 cm at least [1]. In a practical experimental configuration for such a large-aperture antenna, one requires a high bias voltage supply and femtosecond optical regenerative amplifier in order to obtain high THz power, while also employing a parametric generator and cooling system to tune excitation wavelength and remove excessive heat from antennas, respectively. Contrarily, the experimental setup for a small-gap antenna ($G < 0.05$ mm) is compact, but the THz radiation power from small-gap biased PC antennas are considerably lower than that from large-aperture ones [2-4]. Therefore, a compromise between large-aperture and small-gap biased PC antennas is to choose mid-size-gap PC antennas (0.05 mm $< G <$ 2 mm) as THz emission sources inasmuch as one can avoid employing a bulky system for a large-aperture antenna, while benefiting from its higher THz radiation compared to a small-gap antenna. Besides, a mid-size-gap PC antenna offers the significant advantages of being easily fabricated, optically aligned, as well as easily tunable for

THz radiation power in contrast to nonlinear crystal based THz emitters, and thus it

has sparked considerable interest.

5.1 Space-charge bias field screening effect

When a laser light with photon energy larger than the material bandgap is

incident upon a biased PC antenna, electrons are excited into the conduction band and

become electron-hole pairs. Then electrons and holes move toward the metallic

electrodes due to electric attraction force. electrons move to the anode due to its

negative charge, and holes move to the cathode due to its positive charge. The

separation of electrons and holes results in an electric field that is opposite to the bias

field. This space-charge field cancels the bias field partially or completely depending

on the photoexcited carrier concentrations. We call this phenomenon as space-charge

bias field screening effect, or space-charge screening effect for brevity.

The space-charge bias field screening effect is often demonstrated in electrical

device simulation. In 1996, G. Rodriguez and A. J. Taylor [5] use it to interpret the

bipolar THz radiation waveform from bias PC antennas. In their analysis, they

consider the space-charge bias field screening effect by calculating the continuity

equation for electrons and holes together with Poisson equation. On the other hand,

they include the near-THz field screening effect by incorporating a saturation term ,

$q\mu_n n\left(x, t\right) \eta_0 \;/\; \left(1 + n_{dc}\right)$, into the following transport equation:

$$J_n \;=\; \frac{q\mu_n n\left(x, t\right) E\left(x, t\right)}{1 + q\mu_n n\left(x, t\right) \eta_0 \;/\; \left(1 + n_{dc}\right)} \quad . \qquad (5.1.1)$$

For different gap size of PC antenna, they found that the negative peak becomes more

obvious if the pump fluence increases.

5.2 Theoretical methodology

Figure 5.1 schematically draws our THz antennas with different bias voltage V_b

and G. We start from considering how the bias field E_b of multi-GaAs:As$^+$ antennas

changes along both the gap direction x and the depth direction z (or the propagation

direction of pump pulse) before laser pulse excitation. Provided that a bias voltage V_b

is applied to a multi-GaAs:As$^+$ based antenna in the absence of optical pump pulse,

the distribution of E_b along x will be nonuniform instead of being simply an average

value V_b/G. The formation of a nonuniform E_b is due to defects existing within the

antenna, thus altering its electrostatic properties including E_b and space-charge

concentration. The bias V and E_b have traditionally been determined by utilizing the

Poisson equation:

$$-\nabla^2 V = \nabla \cdot E_b = \frac{q}{\varepsilon}\left[p(x,z) - n(x,z) + N_t(x,z) - N_a^-(x,z) \right], \qquad (5.2.1)$$

in which q and ε stand for electron charge and electric permittivity, p and n are the

hole and electron concentrations, while the trap and acceptor concentrations are

denoted by N_t and N_a^-. All the concentrations on the right side of Eq. (5.2.1) obey

Fermi statistics as follows:

$$p(x,z) = N_v\{1 + \exp[(U_f - U_v + qV(x,z))/kT]\}^{-1} \qquad (5.2.2)$$

$$n(x,z) = N_c\{1 + \exp[(U_c - U_f + qV(x,z))/kT]\}^{-1} \qquad (5.2.3)$$

$$N_t(x,z) = N_{t0}\{1 + \exp[(U_f - U_t + qV(x,z))/kT]\}^{-1} \qquad (5.2.4)$$

$$N_a^-(x,z) = N_a\{1 + \exp[(U_a - U_f + qV(x,z))/kT]\}^{-1} \qquad (5.2.5)$$

where N_c and N_v are the conduction and valance-band effective densities of states, N_{t0}

and N_a are the trap and acceptor concentration, the level of the Fermi energy U_f is

determined by letting Eq. (5.2.1) = 0, U_c and U_v are the energy levels of conduction

and valence band, and U_d and U_a are the deep donor and shallow acceptor level. In the

literatures, depending on the doped concentration or ion-implantation conditions, the

U_d values are reported to be about U_c－0.670eV for SI-GaAs [6] and U_c－0.3eV for

multi-GaAs:As$^+$ [7], respectively. For our multi-GaAs:As$^+$ antenna, the PC material

consists of the multi-GaAs:As$^+$ and SI-GaAs parts. The latter has a thickness of

300 μm which value is very much larger than the former layer (~100 nm). To match

the experimental result, U_d and U_a are assumed to be located at U_c－0.690eV and U_v＋

0.0261eV. These two values are closed to that for SI-GaAs case since the SI-GaAs

part provides the major contribution for THz radiation. For a given bias V_b, the potential at the anode depends on the maximum field E_{max} at the metal-semiconductor junction due to image-force lowering, and is given as:

$$V(x=0) = V_b + \sqrt{qE_{max}/4\pi\varepsilon} \,. \tag{5.2.6}$$

The solutions of V_b and E_b are obtained by calculating Eq. (5.2.1) through Eq. (5.2.6) iteratively.

When laser pump pulses propagate through the antenna with time t, a certain amount of n and p are excited and subjected to electric fields. Both n and p obey the current-continuity equations:

$$\frac{\partial n}{\partial t} = \alpha \bar{I}_{opt}(x,z,t) - \frac{n(x,z,t)}{\tau_c} + \frac{1}{q}\nabla \cdot J_n \tag{5.2.7}$$

$$\frac{\partial p}{\partial t} = \alpha \bar{I}_{opt}(x,z,t) - \frac{p(x,z,t)}{\tau_c} - \frac{1}{q}\nabla \cdot J_p \tag{5.2.8}$$

where α and $\bar{I}_{opt}$ stand for the absorption coefficient and the averaged photogeneration rate, and J_n and J_p are the current densities for electron and hole. The averaged photogeneration rate $\bar{I}_{opt}$ is defined by:

$$\bar{I}_{opt}(x,z,t) \equiv \frac{\int I_{opt}(x,y,z,t)dy}{\sqrt{\pi}w_y}$$

$$= \frac{F(1-R)}{hv\sqrt{\pi}w_t}exp[-(\frac{x-x_m}{w_x})^2 - \alpha z - (\frac{t-z/v}{w_t})^2] \tag{5.2.9}$$

where I_{opt} is the pump Gaussian beam, and w_y is the beam width in the y-direction. The pump Gaussian beam I_{opt} can be expressed in terms of a w_t-wide pulse with a w_x-wide spatial profile:

$$I_{opt} = \frac{F(1 - R)}{h\nu\sqrt{\pi}w_t} \exp[-(\frac{x - x_m}{w_x})^2 - (\frac{y}{w_y})^2 - \alpha z - (\frac{t - z / \text{v}}{w_t})^2] \qquad (5.2.10)$$

Here F, $h\nu$, x_m, v, and R refer to pump fluence, photon energy, position of maximum photogeneration rate, phase velocity of pump pulse, and reflection coefficient, respectively.

In addition to J_n and J_p, the separation between n and p also causes a net-charge concentration $\Delta(\equiv p - n)$, which is the main factor that produces space-charge field E_s. The relationship between E_s and Δ is described using the Poisson equation:

$$\nabla \cdot E_s = \frac{q\Delta}{\varepsilon}. \qquad (5.2.11)$$

The summation of J_n and J_p in Eqs. (5.2.7) and (5.2.8) is composed of a total current density J which is related to electron and hole mobilities, μ_n and μ_p, space-charge field E_s, and THz field E by the form:

$$J = J_n + J_p = q\{\mu_n n + \mu_p p\} \{E_s(x, z, t) + E(x, z, t)\}. \qquad (5.2.12)$$

In the near-field regime, the creation of J induces a THz field E satisfying with the wave equation [8]:

$$\nabla^2 E - \mu\varepsilon\frac{\partial^2 E}{\partial t^2} = \mu\frac{\partial J}{\partial t}, \qquad (5.2.13)$$

where μ is the magnetic permittivity. In the far-field regime, the THz radiation field $E_r(t)$ can be obtained by evaluating the broadband Huygen-Fresnel diffraction integral [5.9] of near-field E as follows:

$$E_r(t) = \int \frac{\cos(\hat{z}, \vec{r}\,')}{2\pi r' c_0} \frac{d}{dt} \left\{ E(\vec{x}\,', t - \frac{r'}{c_0}) \right\} ds. \tag{5.2.14}$$

In Fig. 5.1 we schematically illustrate the quantities used to calculate $E_r(t)$. These quantities include the point $\vec{x}\,'$ on the antenna's surface, the observation point $\vec{x}$, the relative vector $\vec{r}\,'$ of x' with respect to x, the distance r' from x' to x, the normal $\hat{z}$ to the surface, the differential area ds on the surface, and the radiation propagation speed c_0 in vacuum. The $\cos(\hat{z}, \vec{r}\,')$ term in Eq. (5.2.14) is known as the obliquity factor. We assume that the observation point locates at the z axis ($\vec{x} = 0$), and the distance from the antenna's surface to the observation point is assumed to be 60 cm.
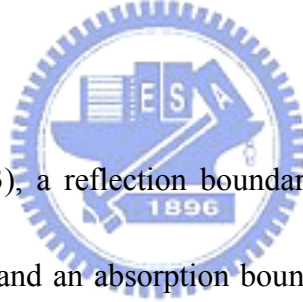
While solving Eq. (5.2.13), a reflection boundary condition was applied to the pump pulse incident surface, and an absorption boundary condition was assumed on the outer surface. In addition, experimental values including F, pulse duration w_t, carrier lifetime τ_c, and spot size w_x are substituted into Eqs. (5.2.1) - (5.2.14) for each G. According to our previous experimental result [10], the effective μ_n is estimated to be 1500 cm^{2}V^{-1}s^{-1}. To match experimental data, the values of μ_n and μ_p were taken to be 1000 cm^{2}V^{-1}s^{-1} and 30 cm^2 V^{-1}s^{-1}, the α, v, n_L, and R were 8×10^5 m^{-1}, 8.3×10^7 m/s, 3.6, and 0.3.

The positive peak E_r^{max} can be obtained by evaluating the maximum of Eq. (5.2.14). The relationship between E_r^{max} and F can be approximately described by the scaling rule [11]:

$$E_r^{max} \approx \frac{F / F_s}{1 + F / F_s},\qquad (5.2.15)$$

where the saturation fluence F_s represents as:

$$F_s = \frac{(1 + n_L)h\nu}{q(1 - R)\mu_n\eta_0}.\qquad (5.2.16)$$

Substituting the effective μ_n value and $n_L = 3.6$ into Eq. (5.2.16), we find that $F_s = 25\mu J/cm^2$.

In calculating Eq. (5.2.1)-(5.2.14), we consider two-dimensional (x and z) structure without the component in the y direction (the lateral gap direction). This omission is because of the lack of the component of bias field in the y direction. Thus, if the carrier concentration n (or p) and photogeneration rate I_{opt} both are the functions of y-variable in Eq. (5.2.7), the integration of $I_{opt}(x, y, z, t)$ with respect to y will be equal to an averaged rate $\bar{I}_{opt}(x, z, t)$. In the first term of the left-hand side and the second term of the right-hand side of Eq. (5.2.7), the integration of $n(x,y,z,t)$ with respect to y will obtain an average carrier concentration $n(x,z,t)$. In addition, the integration of the third term of the right-hand side of Eq. (5.2.7) with respect to y, that is, $\nabla \cdot \int n(x, y, z, t)E_b(x, z, t)dy$ will become $\nabla \cdot n(x, z, t)E_b(x, z, t)$ since E_b is dependent of y.

The appendix B demonstrates that how we solve Eqs. (5.2.7)-(5.2.13) using some

programming routines of Mathematica v 6.0. More complex routines will be

developed in the future works.

5.3   Experimental methods

We performed the experiments by employing THz time-domain spectroscopy as

shown in Fig. 5.2. Each THz radiation emitter consists of two coplanar strip lines with

Au metallic coating layers of 300 nm, and was fabricated on multi-energy

arsenic-ion-implanted GaAs (multi-GaAs:As$^+$) or semi-insulating GaAs (SI-GaAs)

antenna as illustrated in Fig. 5.3. When a pump pulse with 800-nm wavelength

propagates through the Au coating layer of 300 nm, it will attenuate completely due to

the very much small skin depth (~5 nm) of Au, and are not able to excite any carrier

beneath the metallic part. In other word, the PC material below the transmission lines

will have no contribution to the generation of THz radiation in our case. The

transmission line length L and width W are 10 mm and 0.1 mm. For each material, we

chose four samples with different G of 0.02, 0.1, 0.2, and 0.5 mm. Each sample is

implanted with energy of 50, 100 and 200 keV at dosage arsenic ions of 10^{16} ions/cm^2

and furnace annealed at 600°C with 60min processing. By a transient

photo-reflectance measurement the carrier lifetime τ_c of our multi-GaAs:As$^+$ and

SI-GaAs samples were estimated to be as short as 0.7 and 2.5 ps, respectively. The

ion implantation depth was estimated to be about 100 nm by SIMS (Secondary Ion

Mass Spectroscopy) measurement.

To control an average bias field strength E_b (~ 3.5 kV/cm) for preventing the risk

of antenna damage, the V_b (=$E_b \times G$) applied to the anode were: 7, 35, 70, and 175 V

for G = 0.02, 0.1, 0.2, and 0.5 mm, respectively. The experimental setup for the

generation and measurement of THz radiation was similar to the common free space

electro-optical (EO) detection [12] from the emitter of biased PC antennas [13]. In

detail, the pump or probe pulses with 800-nm wavelength and 130-fs pulse width was

also provided by the mode-locked Ti: sapphire laser operating at the repetition rate of

85 MHz and pump power of 500 mW. The pump pulse has spot size w_x of 0.1-mm

diameter, and was normally incident upon the antenna's surface. The laser excitation

positions are depicted in Fig. 5.2. In the case of G = 0.02 and 0.1 mm, x_m = G/2, that is,

the spot positions were central with respect to gap so that both illuminations were

nearly uniform. In the case of G = 0.2 and 0.5 mm, x_m = G/4, the spot positions were

off gap center and near the anode, so that both cases belong to edge-illuminations.

From the values of pump power, spot size, and repetition rate, the pump fluence F

was estimated to be $70 \mu J / cm^2$, corresponding to generated carrier concentration of

$2.0 \times 10^{18} cm^{-3}$. Thus the pump fluence ($F = 70 \mu J / cm^2$) used in the experiment is

considerably larger that the saturation fluence ($F_s = 25 \ \mu\text{J/cm}^2$) estimated from Eq.

(5.2.16). The generated THz radiation beam was thus collimated and focused onto the

EO sensor of ZnTe with thickness of 1.5 mm by a pair of off-axis paraboloidal

mirrors with 12-cm focal length. The distance between the emitter and EO sensor is

about 50 cm. Since the THz radiation was collected by parabolic mirrors in this

experiment, the temporal resolution would be limited by group velocity mismatch

between the optical probe beam and THz radiation. The other coherent polarized

probe beam was collimated onto the EO crystal and the polarization was modified

because of the modified refractive index from THz field. The probe beam was then

transmitted through the analyzer and sampled the THz field from the time delay

between the pump and probe beam.
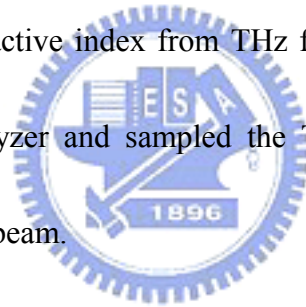
5.4.   Results and discussions

5.4.1 Trap-enhanced bias field

Before presenting the experimental data, we analyze our multi-GaAs:As$^+$ antennas

with numerical results which will be compared with the corresponding measured

results. The measured THz waveforms for SI-GaAs will also be shown without any

explanation of numerical simulation.

For multi-GaAs:As$^+$ antennas, Figure 5.4 shows on a logarithmic scale the simulated bias field $E_b(x)$ as a function of position x for four different G in the absence of pump pulses excitation. Each $E_b(x)$ in Fig. 5.4 is near the edge of the anode ($0 \leq x \leq 10\,\mu$m) and at depth $z = 0.1\,\mu$m. As seen in this figure, the $E_b(x)$ established near the anode are highly nonuniform. For different values of G, one can find much stronger $E_b(x)$ with the larger G. Besides, one common feature in all the cases is that the $E_b(x)$ will grow very rapidly if x approaches the anode ($x \sim 0$). For instance, $E_b(x)$ reaches field strength of as high as 10^3 kV/cm at $x < 0.5\,\mu$m in the case of $G = 0.5$ mm. This gap-dependent strong bias field is a consequence of the PC antennas with larger G being applied by larger bias voltage.
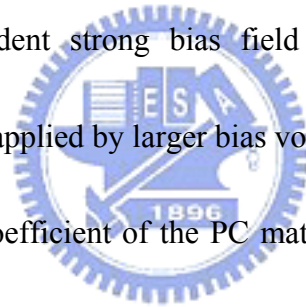
Because the absorption coefficient of the PC material is about 10^6 m^{-1}, the main absorption range of pump pulses is from $z = 0$ to $z = 2\,\mu$m, and is relatively much smaller than the antenna's gap size. Thus, for a given x, E_b is uniform along the z-direction within this absorption range. This is somewhat similar to the distribution of the magnetic field generated from a magnetic bar. Provided that the length of a magnetic bar is 20 cm, then the magnetic field will be uniform near the bar.

5.4.2 Evolutions of parameters in antennas

Next we study the variations of some physical parameters with time at specific

pump depth z and pump fluence F. As an example, Fig. 5.5 shows the calculated

$n(x,t)$, $\Delta(x,t)$, $E_s(x,t)$, and $E(x,t)$ for the case of $G = 0.5$ mm. As can be seen

from Fig. 5.5(a), at $x = 0.12$ mm the photo-excited electron concentration n exhibits a

maximum peak which is the signature of an edge illumination. After excitation, both

the photo-excited electron and hole are subjected to E_s and thus move in opposite

directions since both possess opposite charges. Of importance, the carrier separation

leads to two positive peaks in Δ as depicted in Fig. 5.5(b) where one peak locates at

around the gap center and the other peak is near the anode. Obviously, the magnitude

of the peak near the anode is much larger than that of the central peak. The large peak

has a magnitude of 10^2 of the small peak. This extremely large peak arises from the

combination of three mechanisms: the first is that electron mobility is much larger

than hole mobility, the second is that the enhanced bias field near the anode speeds up

the movement of electron near the anode, and the third is that large amounts of

electrons are absorbed by the anode.

The space-charge bias-field screening phenomenon associated with the two Δ

peaks is demonstrated in Fig. 5.5(c). We can see from this figure that the nonuniform

bias field E_s diminishes from its initial value E_b to a lower value with t. This behavior

originates from the mechanism that the small Δ peak at gap center produces an

opposite field canceling out the original field between the gap center and anode, while the large Δ peak near the anode creates a strong opposite field that screens the original enhanced bias field near the anode. The near-field THz radiation E was obtained from the solution of Eq. (5.2.12), with the result presented in Fig. 5.5(d). It is clear that inasmuch as the electron and bias field have extreme values near the anode, the maximum E also occurs in the vicinity of the anode.

Let us turn to what is the key to the understanding of gap-dependent THz waveform, the variations of Δ and E_s with t at specific z and x near the anode. Substituting four different values of G into the calculations, we obtain the t dependence of Δ and E_s at $x = 0.01$ mm and $z = 0.1\,\mu$m as shown in Fig. 5.6. For each G, one sees that the quantity Δ increases from 0 to $1.6 \times 10^{15}\,\mathrm{cm}^{-3}$ with t. For different G, the larger the G, the larger the Δ. The increase of Δ with t is related to the fast decrease in E_s, which is also plotted in Fig. 5.6. The result of Fig. 5.6 indicates that the decreasing amount of E_s is proportional to G within certain time duration. In other words, it implies that an antenna with larger G also has a larger space-charge screening effect that significantly influents THz radiation waveforms E_r, as we will show in the following.

5.4.3 THz radiation waveforms and spectra

According to Eq. (5.2.13), we calculated temporal THz fields E_r and corresponding Fourier-transformed amplitudes $\tilde{E}_r$ spectra using four different values of G, and the results of these calculations are given in Fig. 5.7(a) and 5.7(b), respectively. For comparison, we present the measured E_r from multi-GaAs:As$^+$ antennas and their corresponding $\tilde{E}_r$ in Fig. 5.7(c) and Fig. 5.7(d). The measured THz waveforms and spectra for SI-GaAs antennas are shown in Fig. 5.7(e) and Fig. 5.7(f). Here we first analyze the measured data for the multi-GaAs:As$^+$ case. In Fig. 5.7(c), each measured waveform contains a dominant positive peak and a negative peak followed by a slowly varying tail. The dimensionless parameter E_r was obtained by normalizing individual waveform to its maximum amplitude, so that the maximum amplitude of E_r is equal to one. In the time domain, the analysis for these waveforms can be characterized in terms of four quantities: the positive peak widths (full width of the positive peak at half maximum) δ_p, and the negative peak widths (full width of the negative peak at half minimum) δ_n, and the negative tail with duration of Γ, and the negative value $-E_r^{\min}$ of the negative peak. In the frequency domain, we concentrate on the frequency bandwidth Δf of the spectrum (full width of the spectrum at half maximum).

Examining the measured positive and negative peaks in Fig. 5.7(c), it is worth noting that the inequality $\delta_p > \delta_n$ is always satisfied at different values of G. In

detail, we observe that the measured δ_p values are fixed to about 0.33 ps which is less than that reported from Grischkowsky *et al*. ($\delta_p \sim 0.38$ ps) [14]. Furthermore, for different *G* the measured values of δ_n are also different, and range irregularly between 0.30 to 0.27 ps without any explicit dependence. For each *G*, one can see from Fig. 5.7(c) that a relatively long negative tail with duration $\Gamma \sim 3.7$ ps follows the negative peak, and is more obvious than those found in other similar experiments [15-16].

Let us now return to analyze the simulated data. In Fig. 5.7(a), we found that the measured feature that $\delta_p > \delta_n$ can also be fulfilled by the simulated data. Besides, the simulated data can reproduce the measured long negative tails. Quantitatively, the simulated δ_p, δ_n, and Γ are about 0.25, 0.18, and 0.8 ps, respectively. While further simulating the model by varying *F*, we found that the numerical solution gives the result of $\delta_p > \delta_n$ at large enough *F* (>10 μJ / cm^2), but a reverse result, $\delta_p < \delta_n$, will be obtained at small *F* (<10 μJ / cm^2). In addition, the simulated positive peak E_r^{max} will vary in a nonlinear way that obeys the scaling rule at various *F* as the case of small or large-gap antennas. On the other hand, as *F* increases, the negative value $-E_r^{min}$ of the simulated negative peak exhibits an increasing trend since a larger *F* will excite larger carrier concentration and thus acquire larger space-charge field screening effect.

5.4.4 Dependence of the negative peak on gap size

Also found in Fig. 5.7 is the phenomenon that the value of $-E_r^{\min}$ varies with G, as well as the bandwidth Δf. The dependences of both the simulated r and Δf on G can be obtained from Figs. 5.6(a) and 5.6(b). In Fig. 5.8 we compare these simulated dependences with the measured ones obtained from Figs. 5.7(c) and 5.7(d). As can be seen, as G increases from 0.02 to 0.5 mm the measured $-E_r^{\min}$ increases monotonically from 0.46 to 0.58, and depends in a strongly nonlinear way on G. The nonlinear dependence of the measured $-E_r^{\min}$ on G can be described by a saturation function with the form $-E_r^{\min} = (0.45G^{0.198} + 0.24)/(1 + 0.14G)$, which is also plotted in Fig. 5.8. The increasing trend in $-E_r^{\min}$ reflects the variation of Δf, and enables Δf to exhibit an increasing trend similar to r. In detail, the measured Δf increases nonlinearly from 1.2 to 1.6 THz with increasing G. These Δf values are close to those reported by Grischkowsky *et al.* [17] $(\Delta f \sim 1.32 \text{ THz})$ and M. Tani *et al.* [18] $(\Delta f \sim 1.63 \text{ THz})$. What is especially interesting is that such large Δf are much larger than those obtained from some large-aperture SI-GaAs antennas $(\Delta f \sim 0.27 \text{ THz})$ [19], as well as some small-aperture SI-GaAs or multi-GaAs:As$^+$ antennas $(\Delta f \sim 1 \text{ THz})$ [20]. This larger Δf is a reflection of a narrow negative peak in Fig. 5.5(c) and

5.5(d), and it is just favorable for applications such as THz medical or security imaging requiring broader spectra.

Compared to the measured data in Fig. 5.8, one can perceive that either the simulated $-E_r^{\min}$ or Δf vary with G in a manner similar to the measured ones. Fits to the simulated $-E_r^{\min}$ yield a saturation function by the form $-E_r^{\min} = (4.42G+0.43)/(1+6.66G)$ as plotted in Fig. 5.8. The values of the simulated $-E_r^{\min}$ agree well with the measured results, while the simulated Δf was found to be larger than the measured ones. This inconsistency is because our simulation neglect some pulse broadening factors such as the THz pulse dispersion in optical elements, and the strong diffraction property of the THz beam optics. In addition, we also ignore the antenna effect in the $100\text{-}\mu\text{m-wide}$ transmission lines where the field traveling in the x-direction is reflected and transmitted into free space (or into the substrate) at the edge of the line due to the large impedance mismatch between the metal and the semiconductor. This antenna effect might be one of the reasons why the experimental pulse width of THz radiation is broader than that of theoretical one. However, it is reasonable to guess the overall characteristics of the THz radiation is determined by the THz field generated in the photoconductive gap and the antenna effect only broadens the pulse shape without changing qualitative characteristics of the THz

radiation. We think that this antenna effect is worthy to be investigated further in future project.

According to the above numerical study, it implies that the underlying mechanism giving rise to the increasing trend in $-E_r^{\min}$ is that $-E_r^{\min} \propto -\partial E_s / \partial t$. In other words, $-E_r^{\min}$ is proportional to the space-charge screening effect. Therefore an antenna with larger G will create a stronger space-charge field screening effect leading to larger $-E_r^{\min}$ and Δf.

On the contrary, in the case of SI-GaAs antenna, $-E_r^{\min}$ decreases linearly from 0.64 to 0.47, and Δf also decreases monotonically from 1.77 to 1.41 THz. Obviously, the curves of Δf versus G vary in a manner similar to those of $-E_r^{\min}$ versus G for both kinds of PC materials.
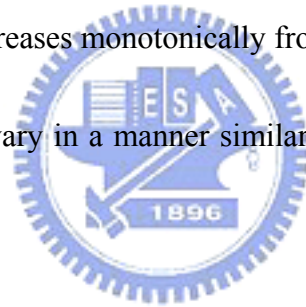
5.4.5 Bias field and pump fluence dependencies

Next we study how the peak THz amplitude $E_r^{\max}$ varies with the bias field E_b and pump fluence F using different PC materials and varying the G *factor*. Figure 5(a) plots the E_b dependencies of $E_r^{\max}$ from SI-GaAs and multi-GaAs:As$^+$ antennas with three different figures for G. As seen in this figure, the data reveals linear variations in the case of $G = 0.02$ mm. In the case of $G = 0.5$ and 1 mm, it is worth noting that nonlinear behaviors occur at both ends of the curve together with linear relationships

appearing in the middle parts of the curves. Such nonlinear behaviors become more

obvious in the case of multi-GaAs:As$^+$ antennas between 6 kV/cm and 9 kV/cm,

where the amplitude reduction is probably owing to the heating effect within the

antennas. This implies that an even higher THz radiation power may be acquired

under good cooling apparatus in the pumping area of the sample. Besides, the

multi-GaAs:As$^+$ antenna has the advantage of enduring a nominal bias field of as high

as 8 kV/cm without causing any electrical damage to itself under photoexcitation. By

contrast, the bias field applied to the SI-GaAs antenna has to be constrained below the

threshold of 4 kV/cm to prevent electrical damage to the devices.

The F dependencies of E_r^{max} are plotted in Fig. 5(b) where the E_r^{max} increases

monotonically with the increase of F for each material and G. We also found that the

antenna with a larger G possesses higher E_r^{max} for each material, and the E_r^{max} of a

multi-GaAs:As$^+$ antenna is lower than that of a SI-GaAs antenna in the measurable

range (i.e. $0 \sim 70 \ \mu J/cm^2$) with the same G. Nevertheless, we perceive that the E_r^{max}

from SI-GaAs antennas reveals slightly saturated trends at a high F, leading to a

reverse consequence that if F is over $70 \ \mu J/cm^2$ the E_r^{max} from multi-GaAs:As$^+$

antennas will be expected to be higher than the SI-GaAs cases, according to the

theoretical curves obtained from the fit to experimental data using the scaling rule

[15].

In the following, we employ the scaling rule to interpret the observations in Fig. 5. It is known that the scaling rule relates E_r^{max} to both E_b and F by the form

$$E_r^{max}(t) \approx D \frac{F}{F_s + F} \quad (5.2.17)$$

where

$$D = \frac{A\sqrt{n_L}E_b}{4\pi\varepsilon_0 c^2 \eta_0 \tau_d z} \quad (5.2.18)$$

$$F_s = \frac{(1 + n_L)h\nu}{q(1 - R)\mu_e \eta_0}. \quad (5.2.19)$$

In this notation, n_L is the refractive index, μ_e is the electron mobility, A refers to pump spot area, and $h\nu$ is the photon energy.

As described in the aforementioned experimental conditions, the diameter of our pump spot area stays at about 0.1 mm, corresponding to an area of $7.8\times10^{-3}\,mm^2$. For the cases of $G = 0.02$, 0.5, and 1 mm, the values of A are equal to the gap area $3.1\times10^{-4}\,mm^2$ in the former case, but equal to the pump spot size $7.8\times10^{-3}\,mm^2$ in the latter two cases as indicated in Fig. 1. According to Eq. (1) and (2), the E_r^{max} of a 0.02-mm-gap antenna is proportional to A, and thus has a lower value either in the bias or pump fluence dependence since its value of A is smaller than the other two cases. As a matter of fact, although the latter two cases have the same value of A, the value of E_r^{max} of a 1-mm-gap antenna is higher than that of a 0.5-mm-gap antenna rather than having the same value of E_r^{max}. The reason is because the strength of the trap-enhanced bias fields E_b near the anode depends on G. As we have mentioned

above, if one applies the same nominal bias field to each antenna, the larger the G, the

higher the E_b near the anode. Thus the E_r^{max} of a 1-mm-gap antenna with a higher E_b is

higher than that of a 0.5-mm-gap antenna with a lower E_b according to Eq. (2).

In Eq. (1) and (2), the n_L and μ_e show involvement with the optical and

electrical properties of PC materials. Due to ion implantation, the values of n_L for a

multi-GaAs:As$^+$ antenna are larger than that of a SI-GaAs antenna, and the effective

μ_e of a multi-GaAs:As$^+$ antenna is estimated to be about 1500 cm^2/Vs less than

that of a SI-GaAs antenna ($\mu_e \sim 3000$ cm^2/Vs). According to Eq. (3), a larger n_L and

smaller μ_e correspond to a larger D and F_s, leading to the E_r^{max} of a multi-GaAs:As$^+$

antenna being lower than a specific F but becoming higher than a specific F at the

same G. Here we take the 0.5-mm-gap antennas as an example to account for the F

dependencies. In Fig. 5(b) the fit to the experimental data yields that $D = 15.6$, $F_s =$

870.5 $\mu J/cm^2$ for a multi-GaAs:As$^+$ antenna, and $D = 10.2$, $F_s = 550.5$ $\mu J/cm^2$ for a

SI-GaAs antenna. We substitute these values into Eq. (1), and thus obtain the

corresponding theoretical curves as plotted by the dashed lines of Fig. 5(b). According

to these two fits for $G = 0.5$ mm, it can be seen that the E_r^{max} of a multi-GaAs:As$^+$

antenna is lower than that of a SI-GaAs antenna if $F < 70 \mu J/cm^2$, but becomes

higher if $F > 70 \mu J/cm^2$. Similar phenomenon has also been found in our

large-aperture GaAs:As$^+$ antennas [19], and hence we believe that the mid-size-gap

multi-GaAs:As$^+$ antennas will benefit from high pump fluence as well.

5.5   Conclusions

We have presented a combined experimental and theoretical study of gap-size

dependent effects on THz radiation.

Experimentally, we used four multi-GaAs:As$^+$ and four SI-GaAs mid-aperture

antennas with different bias voltages and gap sizes to observe their bipolar THz

waveforms in an optical pump-probe experiment. At fixed pump fluence and nominal

bias field, with the increase of gap size of antennas, we observe that both the

bandwidth of THz radiation and the absolute value of THz waveform minimum

decrease linearly for SI-GaAs antennas, whereas they increase monotonically for

multi-GaAs:As$^+$ antennas resulting in a consequence that the bandwidth from a

multi-GaAs:As$^+$ antenna is larger than that from a SI-GaAs antenna at a large gap size.

The bandwidths of the THz radiations from our antennas are considerably larger

compared to other small or large-aperture antennas. In the dependencies of bias field

and pump fluence on the peak THz amplitude, the measured data and associated

theoretical prediction curves indicate that the multi-GaAs:As$^+$ antenna benefits from

110

its higher reachable bias fields, and can generate even higher THz power, probably at high pump fluence, in comparison with SI-GaAs antennas.

Theoretically, we adopted a rigorous model incorporating trap-enhanced bias fields with a set of electromagnetic wave and drift-Poisson equations to interpret our experimental discovery. The numerical simulations demonstrate the carrier and field dynamics under pump pulses propagation within antennas, and also reproduce the THz waveforms which account for the experimental observations, including: increasing trends in both the negative value of the negative peak of terahertz waveform and the bandwidth, larger peak widths, as well as long waveform tails. Our numerical study indicates that an antenna with larger G has a higher trap-enhanced bias field near the edge of the anode, resulting in larger space-charge screening effect and bandwidth.

The results will help us understand the mechanisms responsible for gap-dependent THz radiations, and also enable the researchers to realize how to obtain what they need by controlling suitable experimental conditions.

References

[1] T. Hattori, K. Tukamoto, and H. Nakatsuka, J. Japan. App. Phys. 40, 4907 (2001).

[2] C. Fattinger and D. Grischkowsky, Appl. Phys. Lett. 53, 1480 (1988).

[3] P. U. Jepsen and S. R. Keiding, Opt. Lett. 20, 807 (1995).

[4] P. U. Jepsen, R. H. Jacobsen, and S. R. Keiding, J. Opt. Soc. Am. B 13, 2424(1996).

[5] G. Rodriguez and A. J. Taylor, Opt. Lett. 20, 807 (1996).

[6] C. M. Hurd and W. FL McKinnon, J. Appl. Phys. 75, 596 (1994).

[7] W.-C. Chen and C.-S. Chang, J. Appl. Phys. 81, 7295 (1997).

[8] E. J. Rothwell and M. J. Cloud, *Electromagnetics*, CRC Press New York, 100 (2001).

[9] J. W. Goodman, *Introduction to Fourier Optics*, McGraw-Hill, New York (1996).

[10] T. A. Liu, M. Tani, and C. L. Pan, J. Appl. Phys. 93, 2996 (2003).

[11] M. Tani, S. Matsuura, K. Sakai, and S. Nakashima, Appl. Opts. 36, 7853 (1997).

[12] M. B. Ketchen, D. Grischkowsky, T. C. Chen, C-C. Chi, I. hl. Duling, III, N. J. Hala, J-M. Halbout, J. A. Kash, and G. P. Li, Appl. Phys. Lett. 48, 751 (1986).

[13] Q. Wu and X.-C. Zhang, Appl. Phys. Lett. 67, 3523 (1995).

[14] N. Katzenellenbogen and D. Grischkowsky, Appl. Phys. Lett. 58, 222 (1991).

[15] C. Baker, C. E. Norman, IEEE J. Quantum Electron. 59, 121 (2002).

[16] T. A. Liu, M. Tani, and C. L. Pan, J. Appl. Phys. 93, 2996 (2003).

[17] J. Lloyd-Hughes, E. Castro-Camus, M. D. Fraser, C. Jagadish, and M. B. Johnston, Phys. Rev. B 70, 235330 (2004).

[18] M. Tani, S. Matsuura, K. Sakai, and S. Nakashima, Appl. Opts. 36, 7853 (1997).

[19] E. Sano and T Shibata, IEEE J. Quantum Electron. 26, 372 (1990).

[20] G. Rodriguez and A. J. Taylor, Opt. Lett. 21, 1046 (1996).
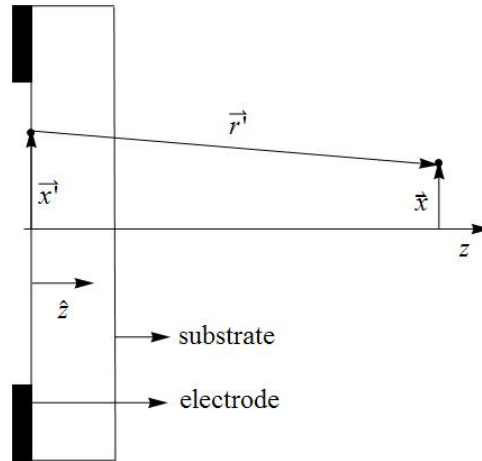
Fig. 5.1: Geometry for calculating the far-THz field $E_r(t)$. $\bar{x}'$ is the point on the

antenna's surface, $\bar{x}$ is the observation point, $\vec{r}'$ is the relative vector of

x' with respect to x, r' is the distance from x' to x, $\hat{z}$ is the

normal to the surface, and ds is the differential area on the surface.
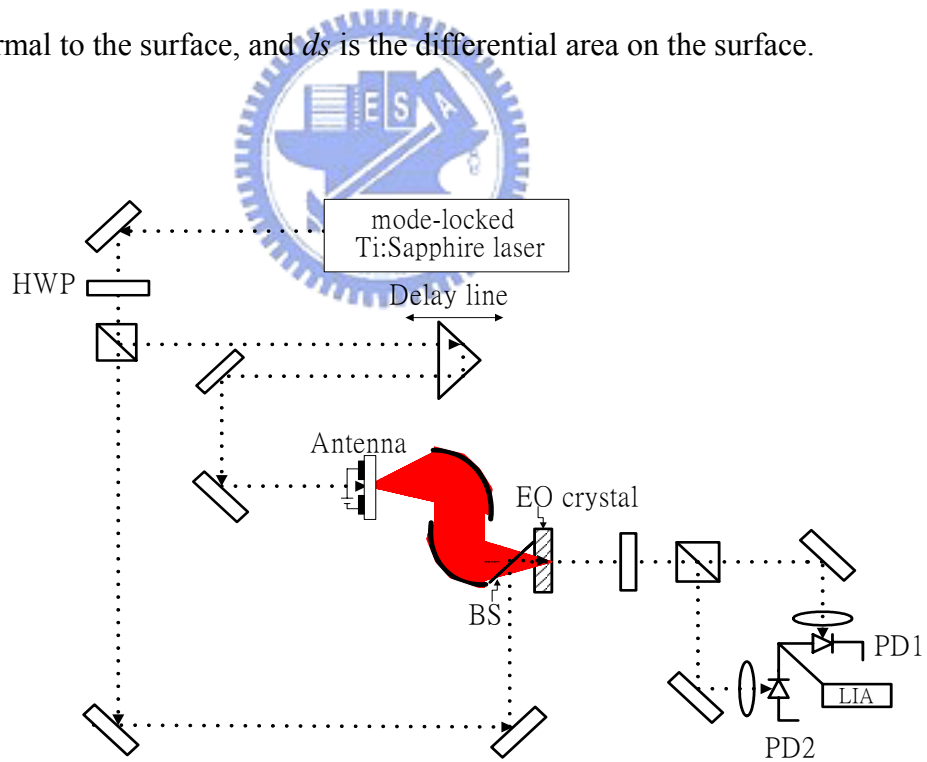
Fig. 5.2: The experimental setup for THz radiation from mid-size-gap

photoconductive antennas.
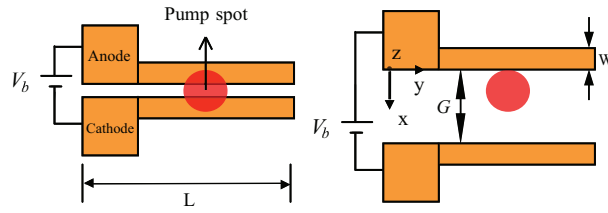
Fig. 5.3: Schematic representation of DC-biased PC antennas excited by femtosecond laser pulses. The transmission line length L and width W are equal to 10 mm and 0.1 mm, respectively. The illuminated regions are indicated by a red circular spot. The left and right diagrams illustrate a uniform illumination for gap size G = 0.02 or 0.1 mm, and an asymmetric illumination for G = 0.2 or 0.5 mm, respectively.
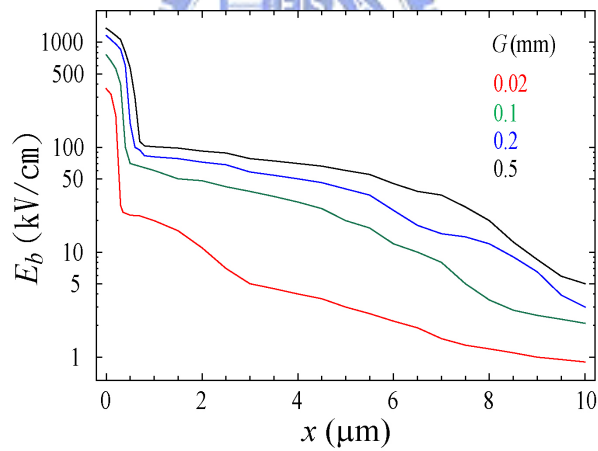
Fig. 5.4: Simulated bias field $E_b(x)$ as a function of position x at depth $z = 0.1$ μm for multi- GaAs:As[+] antennas with gap sizes G of 0.02 (blue), 0.1 (green), 0.2 (red), and 0.5 mm (black).

115
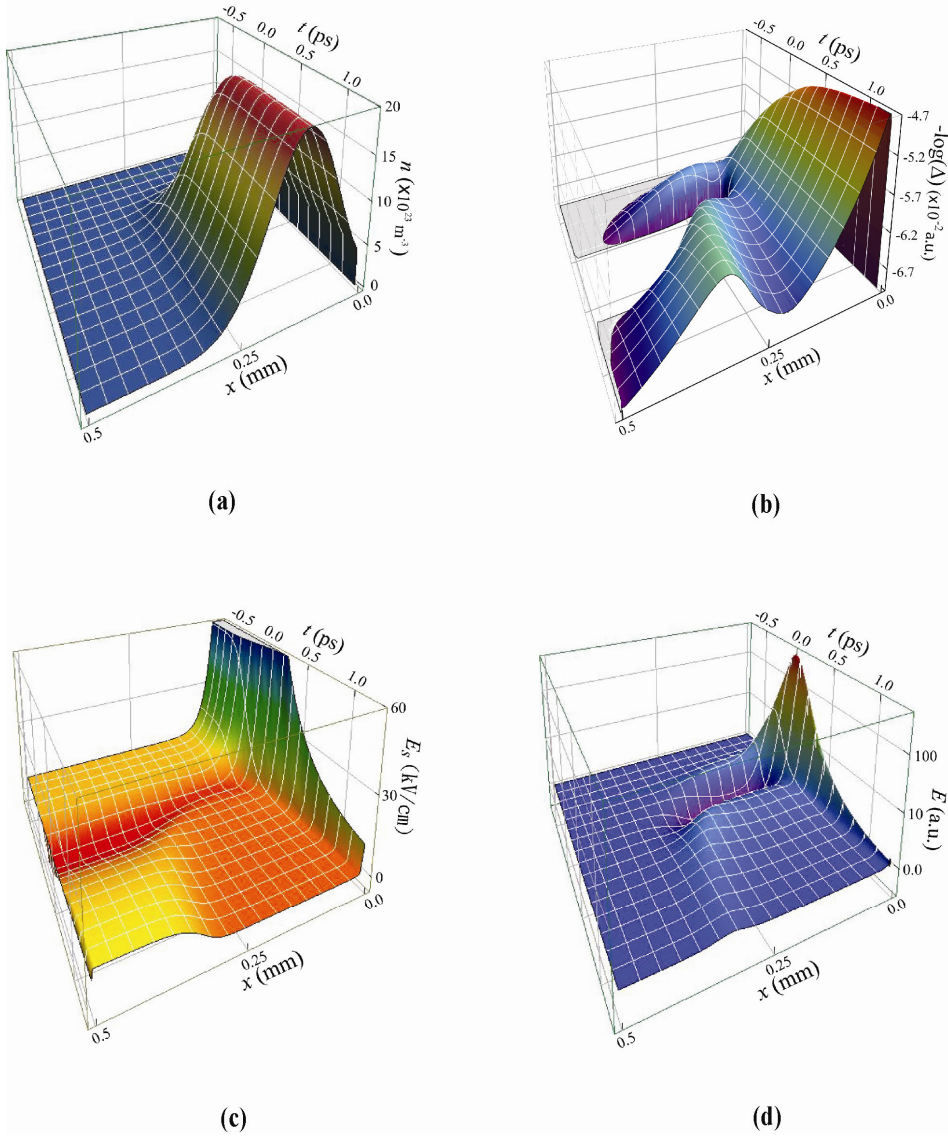
Fig. 5.5: Simulation results. (a) electron concentration $n(x,t)$, (b) negative logarithmic function of the net-charge concentration, $-\log[\Delta(x,t)]$, (c) space-charge field $E_s(x,t)$, and (d) near-field THz radiation $E(x,t)$ as a function of the time delays t and gap position x at pump depth $z = 0.1\ \mu$m for multi-GaAs:As$^+$ antenna with gap size of 0.5 mm. The values of the large and small peaks in (b) correspond to net-charge concentrations of 1.5×10^{15} and $4.0 \times 10^{13}\ (\#/\text{cm}^{-3})$, respectively.
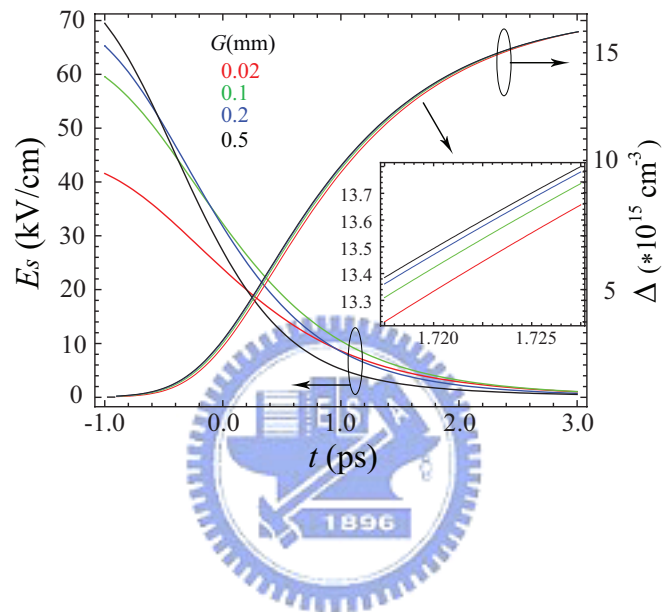
Fig. 5.6: Simulated temporal evolutions of (a) $\Delta(t)$ and (b) $E_b(t)$ at $x = 0.01$ mm and

$z = 0.1\ \mu$m for gap sizes G of 0.02 (blue), 0.1 (green), 0.2 (red), and 0.5 mm

(black). Inset shows a magnified view at $t \sim 1.72$ ps.
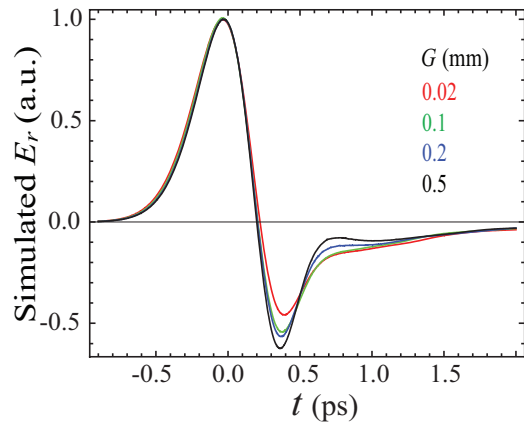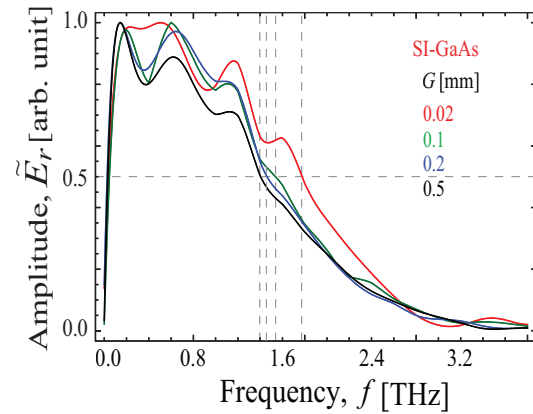
(a)
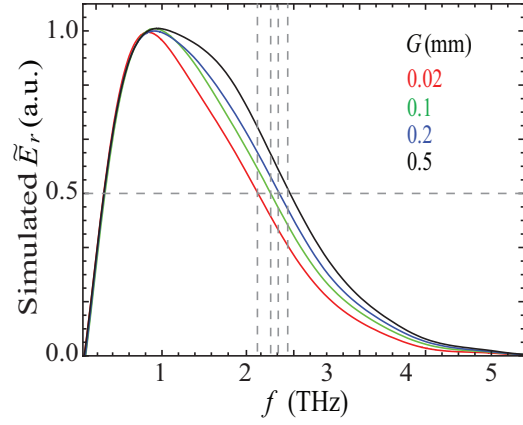
(b)
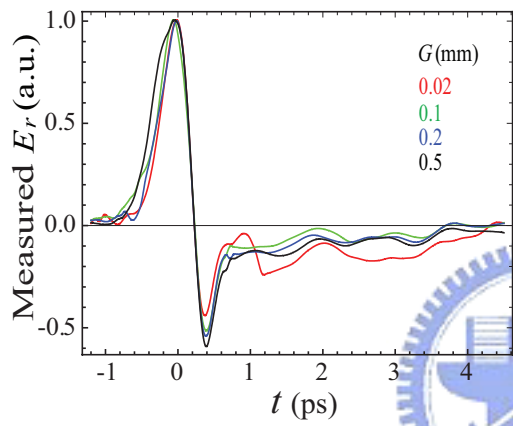
(c)
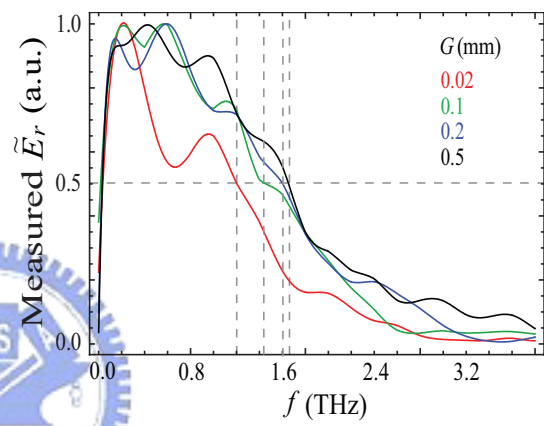
(d)
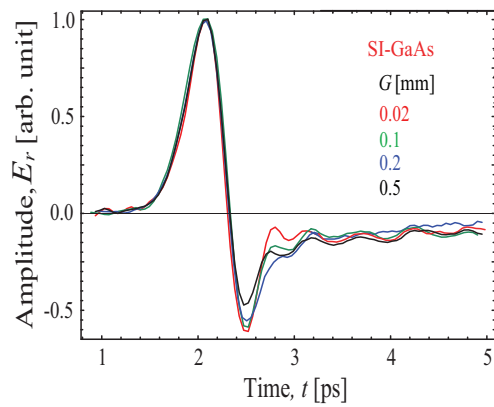
(e)

(f)

Fig. 5.7: Multi-GaAs:As$^+$ results: (a) Simulated and (c) measured THz radiation

waveforms E_r as a function of time delays t for gap sizes G of 0.02 (blue),

0.1 (green), 0.2 (red), and 0.5 mm (black). (b) and (d): The corresponding

Fourier-transformed amplitudes $\tilde{E}_r$ spectra. The pump fluence is

70 $\mu J/\text{cm}^2$. SI-GaAs results: (e) measured THz radiation waveforms E_r

and (f) corresponding Fourier-transformed amplitudes $\tilde{E}_r$ spectra.

(a)   **(b)**
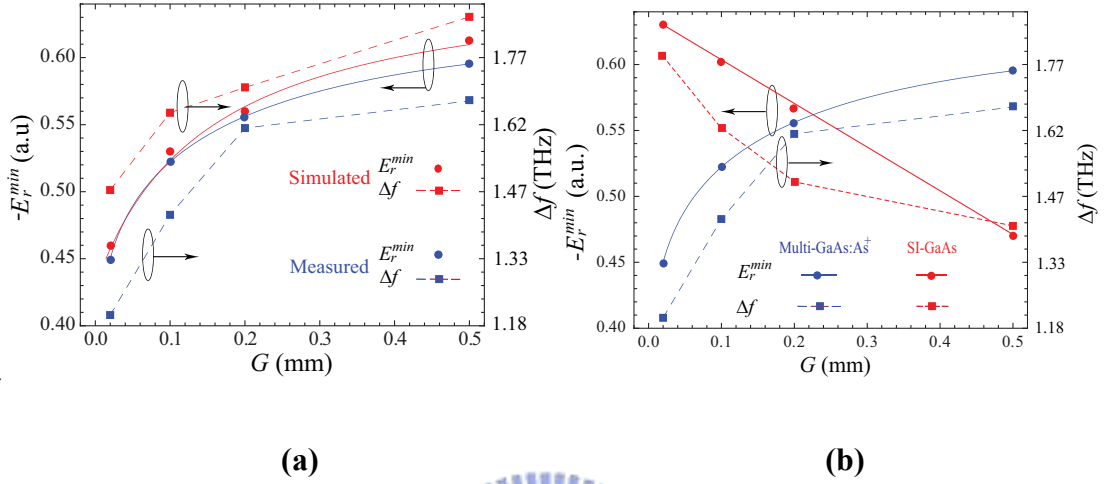
Fig. 5.8: (a) The negative values $-E_r^{\min}$ (circle marks) of the negative peak of THz

waveform, and frequency bandwidth Δf (squares and dashed curves)

versus gap size G for simulation (blue) and measurement (red). The blue and

red solid curves are the fits to the simulated and measured $-E_r^{\min}$. To

compare with the measured Δf, the values of the simulated Δf have been

shifted downward by 0.5 THz. Measured results: (b) Bandwidth Δf (square

marks) and negative values $-E_r^{\min}$ (point marks) of the negative peak of THz

waveform as a function of gap size G for multi-GaAs:As$^+$ (blue) and
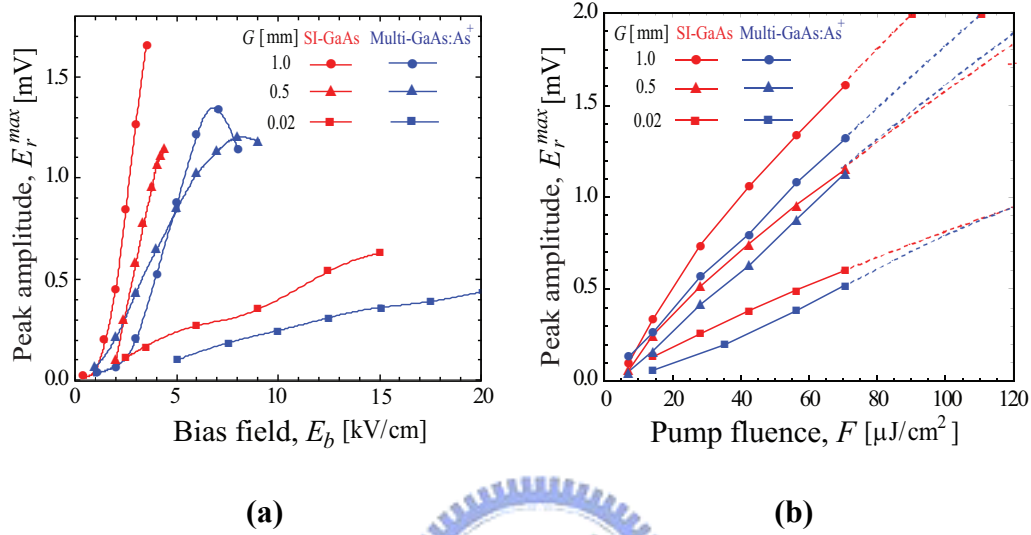
SI-GaAs (red) antennas.

Fig. 5.9: (a) Bias field E_b and (b) pump fluence F dependencies of peak THz amplitude E_r^{max} for multi-GaAs:As$^+$ (blue) and SI-GaAs (red) antennas with gap size G of 0.02 (square marks), 0.5 (triangle marks), and 1 mm (point marks). The pump fluence F is fixed at 70 μJ/cm^2 in (a), and the nominal bias field E_b is kept at 3.5 kV/cm in (b). The dashed lines are the theoretical curves corresponding to different G and material.

Chapter 6

Summary and future works

In this chapter, we summarize the achievements of this work. The following

six original results were achieved:

1. We construct two rigorous theoretical models to simulate the carrier and

   field dynamics in large-aperture and mid-size-gap photoconductive

   antennas. According to these dynamics, we can obtain the corresponding

   characteristics of THz radiation.

2. By calculating the wave and rate equations of the model for

   large-aperture photoconductive antennas, we successfully explain the

   characteristics of THz radiations for the SI-GaAs and GaAs:As$^+$ cases,

   and thus comprehend some important physical mechanisms responsible

   for the observed results.

3. By considering both the trap-enhanced bias field and space-charge field

   screening effect, we give a possible explanation of the gap-dependent

   THz radiation pulses.

4. We verify that the emission efficiency of a large-aperture GaAs:As$^+$

   based antenna is able to be higher than that of large-aperture SI-GaAs

based antenna.

5. Our studies reveal that the frequency bandwidth of THz radiation from GaAs:As$^+$ antenna is larger than that of THz radiation from SI-GaAs antenna.

6. The GaAs:As$^+$ antenna has several advantages that make it replace the SI-GaAs antenna and become a new candidate of THz emission source.

In this numerical study, we regard the whole depth as an effective layer with ion-implanted properties. However, in fact, the GaAs:As$^+$ antenna consists of a GaAs:As$^+$ layer with about hundreds of nanometer, and a SI-GaAs layer with about 300 μm depending on ion-implantation conditions. In the future work, we plan to consider these two layers in practical numerical simulation, and take the advantage of the fullwave approach to study the influence of the ion-implanted layer on the characteristics of THz radiation under various conditions.

In practical situation, the optical and electrical properties such as absorption coefficient and carrier mobility are supposed to vary with different implantation profile. Hence we plan to calculate the dependence of these properties on implantation condition by considering rigorous theory, and then substitute the calculation results into the wave and rate equations in order to see their influence on THz radiation. By doing these plans, we hope to realize how to design a THz emitter with high emission

efficiency and large bandwidth.

Curriculum vitae

出生地: 中華民國臺灣省桃園縣龜山鄉。

生日: 民國 59 年 4 月 8 日。

性別: 男。

住址: 南投縣南投市平和街 8 巷 21 號。

婚姻: 已婚，育有兩子。

電話: 049-2207811; 0918732783。

電子信箱: ronehwa@hotmail.com

民國年 97 月 8 日 國立交通大學光電工程研究所博士班畢業。

民國年 85 月 6 日 國立清華大學物理研究所碩士班畢業。

民國年 78 月 6 日 國立中央大學大氣科學系畢業。

民國年 74 月 6 日 省立板橋高中畢業。

民國年 70 月 6 日 台北市立萬華國中畢業。

民國年 67 月 6 日 台北市立新和國小畢業。

Appendix A

Mathematica codes for the simulation of large-aperture antennas:

Before proceeding to see our simulation code, it is necessary for one to learn some basic operation of Mathematica software. The basic usage of Mathematica can be found in Ref. [1]. Here we only demonstrate how we write the Mathematica programming codes to calculate our wave equation coupled with drift equation.

First we specify the numerical value for every parameter:

```
I0 = 15×10^-2; q = 16×10^-20; h = 662×10^-36; ν = 375×10^12; μ_n = 10×10^-2; μ_p = 1×10^-2; η_0 = 377;
ε_s = 13×8.854×10^-12; ε_p = 1.2×13×8.854×10^-12; ε_r = 1.3×13×8.854×10^-12; n_dc = 37×10^-1;
R = 3×10^-1; τ_n = 10^-10; τ_p = 10^-10; n_s = 10^18; α = 1×10^6; E0 = 60×10^3; tb = -6/2; te = 30/4;
wt = 5×10^-14; zb = 0; ze = 1×10^-5; μ_m = 400 π×10^-9;
F = I0 (1 - R) / (h ν √π);
```

Next we construct the wave and drift equations:

$$
\text{Maxwell} = \Big\{ \partial_{z,z}\, \mathbb{E}x[z,\,t] - \frac{\mu_m\, \epsilon_r}{wt^2}\, \partial_{t,t}\, \mathbb{E}x[z,\,t] - \mathbb{i}\, \frac{\mu_m\, \epsilon_r}{10\, wt^2}\, \partial_{t,t}\, \mathbb{E}x[z,\,t] ==
$$

$$
\frac{\mu_m\, \alpha\, q}{wt}\, \partial_t \left(\big(\mu_n\, n[z,\,t] + \mu_p\, p[z,\,t] \big)\, (E0 + \mathbb{E}x[z,\,t]) \right),
$$

$$
\partial_t\, n[z,\,t] == F \times \text{Exp}\!\left[-\left(t - \sqrt{\mu_m\, \epsilon_p}\, \frac{z}{wt} \right)^2 \right] \text{Exp}[-\alpha\, z] - \frac{wt}{\tau_n}\, n[z,\,t],
$$

$$
\partial_t\, p[z,\,t] == F \times \text{Exp}\!\left[-\left(t - \sqrt{\mu_m\, \epsilon_p}\, \frac{z}{wt} \right)^2 \right] \text{Exp}[-\alpha\, z] - \frac{wt}{\tau_n}\, p[z,\,t]
$$

$$
\Big\};
$$

In the above equations, the time is normalized to the pump pulse width, and thus dimensionless.

These nonlinear partial differential equations have to be solved by specified proper initial and boundary conditions as follows:

```
initial = { Derivative[0, 1][Ex][z, tb] == 0, Ex[z, tb] == 0,

        Derivative[1, 0][Ex][zb, t] - Cos[π/2.5] (√(μm εr))/wt Derivative[0, 1][Ex][zb, t] == 0,

        Derivative[1, 0][Ex][ze, t] + (√(μm εr))/wt Derivative[0, 1][Ex][ze, t] == 0,

    n[z, tb] == 0, p[z, tb] == 0 };
```

Here the factor $\cos[\pi/2.5]$ corresponds to the reflection coefficient of 0.3, and 1 refers to the absorption boundary condition.
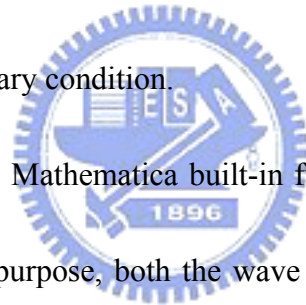
Now we can make use of the Mathematica built-in function "NDSolve" to calculate our equations. To reach this purpose, both the wave and initial-boundary conditions have to be put into the Mathematica built-in function "Join":

```
sol = NDSolve[Join[Maxwell, initial],
    {Ex, n, p}, {z, zb, ze}, {t, tb, te}, MaxStepSize → {1×10⁻⁷, ∞}];
```

After NDSolve has done the calculation, the numerical solutions of carrier concentration n, p, and field E_x will be returned and storaged in the name "sol". If we want to plot n, p, or E_x, we can specify a name for each variable. For example, the electron concentration can be written as

```
n[z_, t_] = n[z, t] /. sol[[1]];
```

Then we can use the function "plot" or "plot3D" to see the simulation results as follows:

```
Plot3D[n[z, t], {z, zb, ze}, {t, tb, te}, PlotRange→All,
  ViewPoint→{1.2`, 1.5`, 1.2`}, Mesh→False, PlotPoints→80]
```

```
Plot3D[Abs[dtEx[z, t]], {z, zb, ze}, {t, tb, te}, ViewPoint→{1.2`, 1.5`, 1.2`},
 Mesh→False, PlotPoints→60, BaseStyle→{FontFamily→"Times", FontSize→12},
 Boxed→True, BoxStyle→RGBColor[0.1`, 0.5`, 0.2`],
 ViewPoint→{1.57`, -0.75`, 0.91`}, AspectRatio→1.05`, FaceGrids→All]
```

If one want to see the THz data in the frequency domain, one can use the Mathematica built-in function "FFT" to transform the time-domain waveforms to frequency spectra. We demonstrate a convenient package to do this transformation. The package listed below is to use the Mathematica built-in function "Module" to integrate all the function required for evaluating Fourier-transform of temporal waveforms:

```
fftSpectrum[f_, t_, tMin_, tMax_] := Module[{dt, fData, ffData, plot},
   dt = N[(tMax - tMin) / (2^8 - 1)];
   fData = N[Table[f, {t, tMin, tMax, dt}]];
   ffData = Abs[Chop[Fourier[fData, FourierParameters→{-1, 1}]]];
   plot = ListPlot[ffData, Frame→True, Joined→True, PlotRange→{{0, 16}, All}];
   rawData = ffData
  ];
```

Appendix B

Mathematica codes for the simulation of mid-size-gap antennas:

The Mathematica codes for the simulation of mid-size-gap antennas is somewhat similar to that for large-aperture ones. The difference is that we should consider the drift of electron and hole and the space-charge electric field in the program code. The most difficult to do with is to solve the Poisson equation along with the carrier rate equations because the Poisson equation is a first-order spatial derivative whereas the rate equation is both first-order spatial and temporal derivative. The traditional method to solving Poisson and rate equations simultaneously is to make use of iterative approach. Here we introduce a method that makes the equations easy to be implemented in Mathematica software. The method is to differential the two sides of Poisson equation with respect to time, simultaneously.

The step is similar to the appendix A. We may give the numerical value for every parameter:

$\text{I0} = 70 \times 10^{-2};\ \text{q} = 16 \times 10^{-20};\ \text{h} = 662 \times 10^{-36};\ \nu = 375 \times 10^{12};\ \mu_n = 10 \times 10^{-2};\ \mu_p = 1 \times 10^{-2};\ \eta_0 = 377;$

$\epsilon_s = 13 \times 8.854 \times 10^{-12};\ \epsilon_p = 2.5 \times 13 \times 8.854 \times 10^{-12};\ \epsilon_r = 1 \times 13 \times 8.854 \times 10^{-12};\ \text{n}_{dc} = 37 \times 10^{-1};$

$\text{R} = 3 \times 10^{-1};\ \text{τn} = 10^{-10};\ \text{τp} = 10^{-10};\ \tau_n = 10^{-10};\ \tau_p = 10^{-10};\ \text{D}_n = 0 \times 10^{-4};\ \text{D}_p = 0 \times 10^{-4};\ \text{n}_s = 10^{18};$

$\alpha = 0.8 \times 10^6;\ \text{E0} = 20 \times 10^4;\ \text{Ec} = 5 \times 30 \times 10^4;\ \text{tb} = -\dfrac{6}{2};\ \text{te} = \dfrac{30}{4};\ \text{wt} = 15 \times 10^{-14};\ \text{xb} = 0;$

$\text{xe} = 1 \times 10^{-4};\ \text{wx} = 1.3 \times 10^{-5};\ \text{zb} = 0;\ \text{ze} = 1 \times 10^{-5};\ \mu_m = 400\,\pi \times 10^{-9};$

$$\text{F} = \frac{\text{I0}\,(1 - \text{R})}{\text{h}\,\nu\,\sqrt{\pi}};$$

Then we specify the wave and rate equations below:

$$\text{Maxwell} = \Big\{ \partial_{z,z}\mathbb{E}x[x, z, t] - \frac{\mu_m\,\epsilon_r}{wt^2}\,\partial_{t,t}\mathbb{E}x[x, z, t] ==$$

$$\frac{\mu_m\,\alpha\,F\,q}{wt}\,\partial_t\Big(\big(\mu_n\,n[x, z, t] + \mu_p\,p[x, z, t]\big)\,(E0 + \mathbb{E}xsc[x, z, t] + \mathbb{E}x[x, z, t])\Big),$$

$$\partial_t\,\mathbb{E}xsc[x, z, t] ==$$

$$-\frac{\alpha\,F\,q}{\epsilon_s}\,\big(wt\,\mu_p\,p[x, z, t] + wt\,\mu_n\,n[x, z, t]\big)\,(E0 + \mathbb{E}xsc[x, z, t] + \mathbb{E}x[x, z, t]),$$

$$\partial_t\,n[x, z, t] == \text{Exp}\Big[-\Big(\frac{x - xe/2}{wx}\Big)^2\Big]\,\text{Exp}\Big[-\Big(t - \sqrt{\mu_m\,\epsilon_p}\,\frac{z}{wt}\Big)^2\Big]\,\text{Exp}[-\alpha\,z] - \frac{wt}{\tau_n}\,n[x, z, t] +$$

$$wt\,\mu_n\,\partial_x\,(n[x, z, t]\,(E0 + \mathbb{E}xsc[x, z, t] + \mathbb{E}x[x, z, t])) + wt \times D_n\,\partial_{x,x}n[x, z, t],$$

$$\partial_t\,p[x, z, t] == \text{Exp}\Big[-\Big(\frac{x - xe/2}{wx}\Big)^2\Big]\,\text{Exp}\Big[-\Big(t - \sqrt{\mu_m\,\epsilon_p}\,\frac{z}{wt}\Big)^2\Big]\,\text{Exp}[-\alpha\,z] - \frac{wt}{\tau_n}\,p[x, z, t] -$$

$$wt\,\mu_p\,\partial_x\,(p[x, z, t]\,(E0 + \mathbb{E}xsc[x, z, t] + \mathbb{E}x[x, z, t])) + wt \times D_p\,\partial_{x,x}p[x, z, t]$$

$$\Big\};$$

The above equation has to be solved along with the following initial-boundary condition:

$$\text{initial\,–\,boundary} = \Big\{ \text{Derivative}[0, 0, 1][\mathbb{E}x][x, z, tb] == 0,\ \mathbb{E}x[x, z, tb] == 0,$$

$$\text{Derivative}[0, 1, 0][\mathbb{E}x][x, zb, t] - \frac{\sqrt{\mu_m\,\epsilon_r}}{wt}\,\text{Derivative}[0, 0, 1][\mathbb{E}x][x, zb, t] == 0,$$

$$\text{Derivative}[0, 1, 0][\mathbb{E}x][x, ze, t] + \frac{\sqrt{\mu_m\,\epsilon_r}}{wt}\,\text{Derivative}[0, 0, 1][\mathbb{E}x][x, ze, t] == 0,$$

$$\mathbb{E}x[xb, z, t] == 0,\ \mathbb{E}xsc[x, z, tb] == 0,\ \mathbb{E}xsc[xb, z, t] == 0,\ n[x, z, tb] == 0,$$

$$n[xb, z, t] == 0,\ n[xe, z, t] == 0,\ p[x, z, tb] == 0,\ p[xb, z, t] == 0,\ p[xe, z, t] == 0\Big\};$$

These equations are joined by the built-in function "Join", and solved by the built-in

function "NDSolve" with proper stepsize control in each dimension.

```
sol = NDSolve[Join[Maxwell, initial], {Ex, Exsc, n, p},
          {x, xb, xe}, {z, zb, ze}, {t, tb, te}, MaxStepSize → {1×10⁻⁶, 5×10⁻⁷, ∞}];
```

Finally, the solution can be extracted from the name "sol", and also plotted by the

built-in function "plot3D:

```
n[x_, z_, t_] = n[x, z, t] /. sol[[1]];
```

$$Plot3D\left[n\left[x, \frac{ze}{2}, t\right], \{x, xb, xe\}, \{t, tb, te\},\right.$$
$$\left.PlotRange → All, ViewPoint → \{1.2`, 1.5`, 1.2`\}, Mesh → False, PlotPoints → 80\right]$$